Doctoral Thesis

Thesis Title

Effects of Butanol Addition on Sooting Limits and

Soot Precursor Formation Behaviors of *n*-Heptane

Flames using a Micro Flow Reactor with a Controlled

Temperature Profile

Department of Mechanical Systems and Design,

Graduate School of Engineering,

TOHOKU UNIVERSITY

MOHD HAFIDZAL BIN MOHD HANAFI

Advising Professor at Tohoku Univ.	Professor Maruta, Kaoru
Research Advisor at Tohoku Univ.	
Dissertation Committee Members Name marked with "○" is the Chair of the Committee	○ Prof. Maruta, Kaoru 1 Prof. Kobayashi, Hideaki 2 Associate Prof. Nakamura, Hisashi

TOHOKU UNIVERSITY
Graduate School of Engineering

Effects of Butanol Addition on Sooting Limits and Soot Precursor Formation Behavior of
n-Heptane Flames using a Micro Flow Reactor with a Controlled Temperature Profile

（温度分布制御型マイクロフローリアクタによる正ヘプタン火炎のすす生成限界とすす前駆体生成挙動

に及ぼすブタノール添加の影響）

`

A dissertation submitted for the degree of Doctor of Philosophy (Engineering)

Department of Mechanical Systems and Design

by

Mohd Hafidzal Bin MOHD HANAFI

July 5, 2019

Effects of Butanol Addition on Sooting Limits and Soot Precursor Formation Behavior of n-Heptane Flames using a Micro Flow Reactor with a Controlled Temperature Profile

Mohd Hafidzal Bin Mohd Hanafi

Abstract

Research on Polycyclic Aromatic Hydrocarbons (PAHs) and soot reduction is important in combustion studies. The former is known as soot precursor, which is harmful to people, the environment, and engines. Soot emission can be minimized by mixing primary fuel with oxygenated fuel. Butanol, which is known as an oxygenated fuel, was used in this study due to it being a second-generation biofuel capable of reducing soot emission. Other reported advantages of n-butanol relative to methanol and ethanol are its higher cetane number, lower volatility, and higher energy density.

Previous studies elucidated soot behavior(s) at higher temperatures (>1,500 K), however, studies on soot behavior at temperatures under 1,400 K is rare. Elucidating the effect of the addition of butanol on sooting tendency and the formation of PAHs would help explain sooting behavior(s), while identifying the major reactions of the effect of mixing butanol with small and large hydrocarbons, as well as PAHs would help detail the soot formation process. Both would lead to the development of an accurate model for predicting PAHs and soot, especially at lower temperatures.

This work intends to elucidate the effect of the addition of butanol on sooting tendencies and PAHs formation of n-heptane using a micro flow reactor with a controlled temperature profile (MFR). The MFR, relative to other conventional methods, is capable of providing gentle temperature profiles in the reactor, while also distinguishing the reaction zone of flame, PAHs growth, and soot formation. This would be tremendously helpful when validating the gas phase chemical kinetic mechanism in fuel-rich conditions prior to soot formation.

The study of the effects of the addition of n-butanol on sooting tendency and formations of C_1 and C_2 primary intermediates of n-heptane/air mixtures were performed using MFR at a maximum wall temperature of 1,300 K. Three types of fuel at different mole percentage ratios were used in this study, consisting of pure n-heptane (hp100), n-butanol (bt100), as well as their mixture of n-heptane 50% and n-butanol 50%, that termed as hp50bt50. The sooting tendency was investigated over equivalence ratios of 1.5 - 4.0, an inlet mean velocity of 10 cm/s, and a pressure of 1 atm. Experimental observations indicated two types of flames: with and without soot formation. The critical sooting equivalence ratio was identified, which in the case hp100 was 2.0, in the case of hp50bt50 was 2.2, and for bt100 was 2.6. These values confirmed that the critical equivalence ratio is directly proportional to the n-butanol mole percentage, implying that mixing it with butanol lowered sooting tendencies. The effect of the addition of butanol is also evident due to the length of the sooting region in the MFR, and increased addition of butanol results in shorter region lengths.

The capability of current chemical mechanisms, such as CRECK, Veloo, Sarathy and Wang were also examined by comparing the maximum heat release rate (HRR) with the flames position of the experimental results.

The CRECK mechanism reported a fair agreement with the measurement results relative to that of other mechanisms.

The effect of the addition of butanol to the sooting tendency of n-heptane was further evaluated by measuring small hydrocarbon species (C_1 and C_2). The measurements were conducted at equivalence ratios of 1.5 - 4.0, and a maximum wall temperature of 1,100 K using MFR equipped with Gas Chromatography-Thermal Conductivity Detector (GC-TCD). Six species were measured, which were C_2H_4, C_2H_2, C_2H_6, CH_4, CO, and CO_2. The computations used five chemical mechanisms; CRECK, Wang, reduced and detailed Livermore, and KUCRS. The CRECK mechanism accurately predicted the trend of C_1 and C_2 species at multiple equivalence ratios. It was also used to analyze the relation between soot precursor (C_2H_4 and C_2H_2) and the final formation species (CO and CO_2). The CRECK mechanism showed the C_2H_4 and C_2H_2 mole fraction decreasing, while CO and CO_2 mole fraction increasing with increasing the mole percentage of butanol, especially at higher equivalence ratios. This trend was also observed from the measurement of the species.

Large hydrocarbons and PAHs (C_6H_6, C_6H_5OH, C_7H_6O, C_8H_{10}, C_8H_8, and $C_{10}H_8$) were measured using MFR equipped with Gas Chromatography/Mass Spectrometry (GC/MS). The computation uses the CRECK mechanism at equivalence ratios of 1.5 - 2.5 and a maximum wall temperature of 1,100 K. It can be seen that the CRECK mechanism is in agreement with the experimental results (similar trends). Large hydrocarbons and PAHs mole fractions are inversely related to the mole percentages of butanol.

The overall reaction path analysis and major reactions in the rate of production/consumption involving small and large hydrocarbons and PAHs were determined for CRECK mechanism. R1617: $CH_3CH_2CH_2CHOH<=>CH_3CHO+C_2H_5$ was identified as the key reaction controlling the concentrations of C_2H_2, C_2H_4, CO, and CO_2, while the reactions identified as major reactions controlling the concentrations of large hydrocarbons and PAHs were R1612: $CH_3CHCH_2CH2OH<=>C_3H_6+CH_2OH$, R1615: $CH_3CH_2CHCH_2OH<=>NC_4H_8+OH$, and R1617: $CH_3CH_2CH_2CHOH<=>CH_3CHO+C_2H_5$.

The results from this work provide new insights into sooting tendency and PAHs formation behavior at lower temperatures, which is expected to benefit mankind, the environment, and engines in the near future.

Table of Contents

List of Figures

Chapter 3

List of Tables

Nomenclature

Symbol	Description
A	Cross sectional area
C_P	Specific heat at constant pressure
D	Molecular diffusivity of the fuel to the mixture
I_e	Ionizing electron energy
I_t	Total ion current
$\dot{M}$	Mass flow rate
N	Molecules' concentration
Nu	Nusselet number
P	Pressure
Q	Total ionization cross section
T	Gas-phase temperature
T_w	Wall temperature
U_0	Inlet Mean velocity
V_k	Diffusion velocity
Y_k	Mass fraction
W_k	Molecular weight
a_O	Coefficient for oxygen molecules for ionization cross section
a_C	Coefficients of carbon molecules for ionization cross section
a_H	Coefficient for hydrogen molecules for ionization cross section
d	Inner diameter of reactor
h_k	Specific enthalpy
n_C	Number of carbon atom in molecules
n_H	Number of hydrogen atom in molecules
$\dot{\omega}_k$	Rate of production

x	spatial coordinate
λ	Thermal conductivity of the mixture
ρ	Density of the mixture
ϕ	Equivalence ratio

Chapter 1

Introduction

1-1 Background of this study

Combustion is defined as an exothermic reaction, due to its energy release upon completion, and Warnatz et al. [1] reported that ~90 % of energy production can be attributed to. Energy is crucial to the survivability of mankind, due to its role in heating and preparing food, and the study of combustion, in the context of energy, is regarded as a meaningful endeavor.

Combustion of gasoline and diesel in engines dictates almost the entirety of ground transportation. As per Figure 1.1.1(a), transportation(s) mainly utilizes gasoline as fuel, especially ground transportation. The demand for oil as fuel for ground transporation is significantly different relative to the other components. Its low supply accompanying high demands prompted researchers to look elsewhere, and the promising characteristic of biofuels (renewable and environmentally friendly) render it an attractive subsitute. The use of renewable energy is becoming more widespread. It is expected that the use of electricity and gas for transporation will become common in the near future. Energy demand is projected to continue increasing from 1980 to 2035.

Figure 1.1.1(b) shows the transport activity based on countries from 2000 to 2050.

Most countries show an upward trajectory in its use of transportation up till 2050. This increase will also result in increased combustion emissions, such as soot, which is an incomplete combustion product that is harmful to people [5,6], the environment [7] as well as engines [8,9].
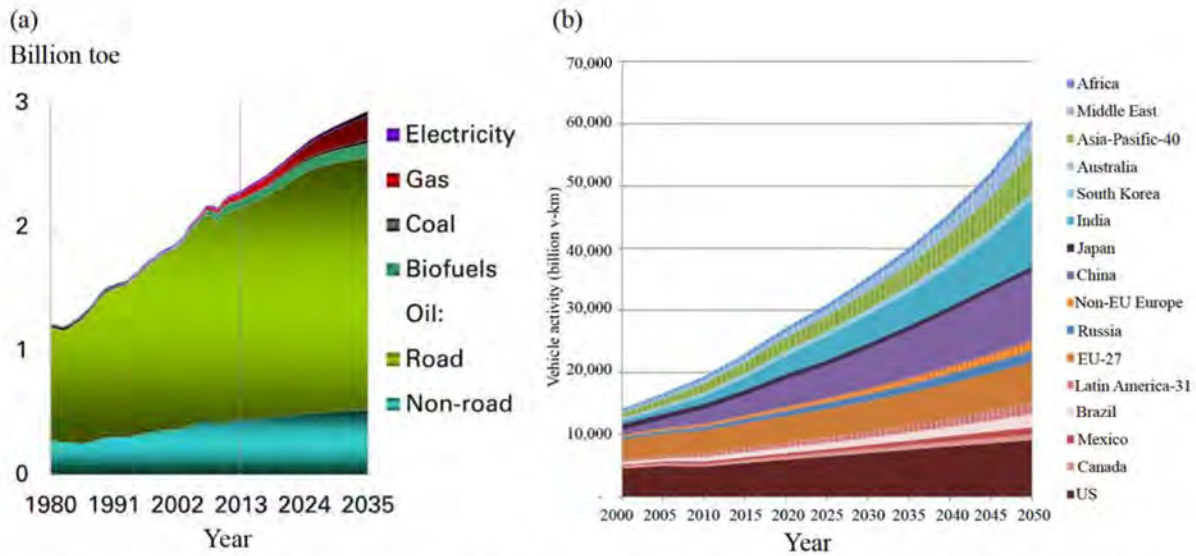
Fig. 1.1.1 (a) Transportation demand of fuel from year 1980 to 2035 [2], (b) Transport activity based on countries from year 2000 to 2050 [3,4].

Soot, or particulate matter, is a hazardous component. Figure 1.1.2 shows the types of particulate matter based on its size and its effects on our bodies. Particulate matter with diameters of 2.5 - 10 μm are known as PM_{10}, while particulate matter with diameter in the range of 1.5 to 2.5 μm are known as $PM_{2.5}$, and particulate matter smaller than 1.0 μm are known as $PM_{1.0}$. Barfknecht et al. [5] reported that small soot particles with diameters lower than 5 nm is transported directly to human lungs, since the respiratory tract is unable to filter it. This leads to diseases such as asthma, cancer, chronic bronchitis, and collapsed lungs [10].

Combustion also produces polycyclic aromatic hydrocarbons (PAHs), which is as harmful to our bodies as soot. PAHs are generally smaller than soot, with diameters of less than 3 nm. Soot emmision also results in environment pollution. Bond et al. [12] posited that soot is the secondmost severe contributor to global warming after carbon dioxide. Figure 1.1.3 illustrates how soot emmision affect the environment. For example, soot released from factories,

transports, and open burning causes direct absorption by solar radiation, which increases the earth's surface temperature. Moreover, in colder climates, soot particles prevents the reflection of sunlight, which melts snow and ice at a quicker rate. The fact that soot emission is detrimental to air quality and the environment is undeniable, which prompted many countries to implement and enforce regulations for limiting soot emissions.
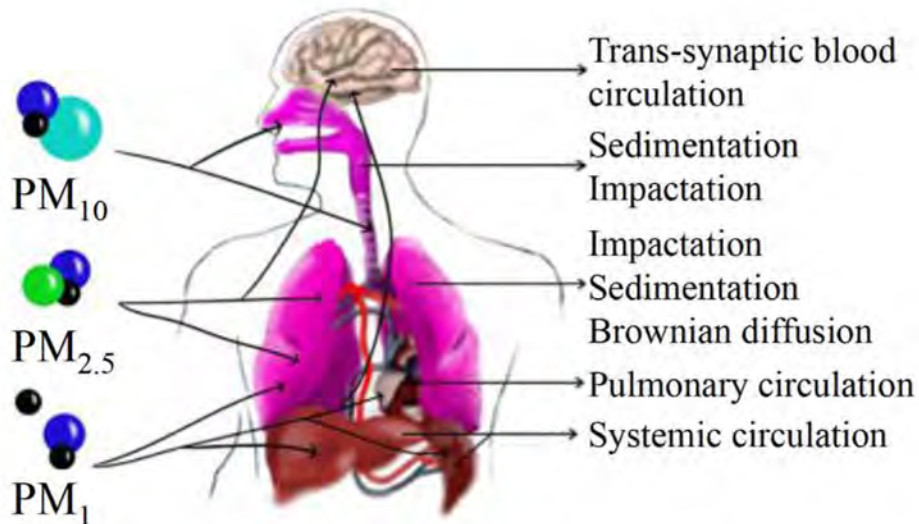
Fig. 1.1.2 Size of particles inside our body [11].
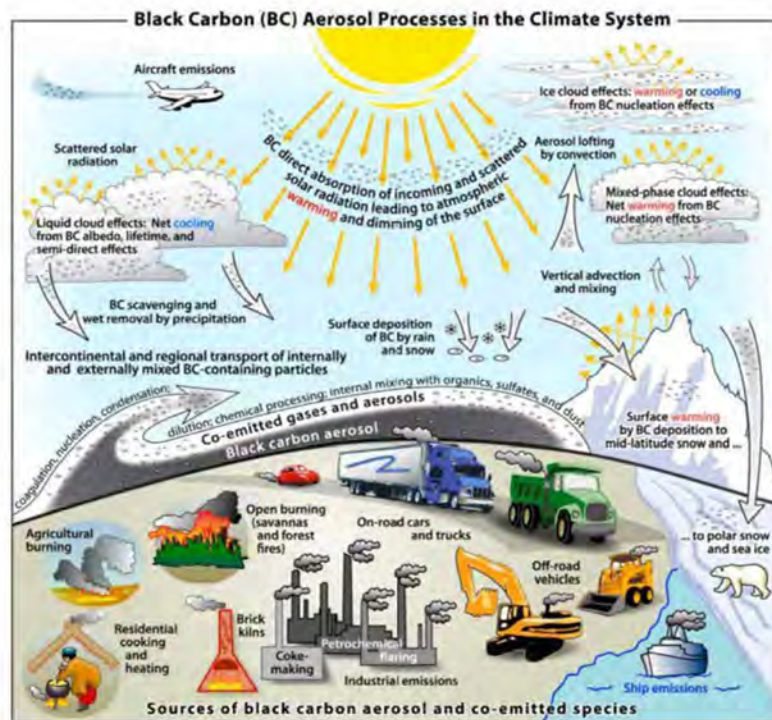
Fig. 1.1.3 Black carbon (soot) sources and its effects on the environment [12].

Soot is not only problematic to health and the environment, but it is it also negatively impact engines. High soot concentration in engines will contaminate the lubricant oil, which shortens its life and increase its service frequency. Continued usage of contaminated lubricant oil will severely wear the engine. Figure 1.1.4 shows the effect of soot on lubricant oil in diesel engine by using contamination index (IC), residual dispersancy (MD) and combined performance rating (DP) [13].

IC is applied to identify the concentration of insoluble matter in the lubricant oil which the scale is within 0.1 to 4 percent scale. High IC value means combustion is not efficient. Some of the reasons for high value of IC are problems in fuel injection, lugging and low compression.

MD represents the quality of lubricant oil. Lower value of MD signifies that the oil is not effctive and should be replaced earlier. Large number of soot causes lower value of MD since the soot lower down the oil's residual dispersion ability. This problem leads to change the colour of oil to become blacker and darker, thus it has high possibility to interfere with the oil flow toward engine's parts.

DP is a combination measurement of IC and MD methods. DP rating helps the user in monitoring degradation of oil condition. It is expressed by a rating from 0 to 200. High DP signifies poor oil condition which can be caused by high quantity of soot particles that related with too long between oil changes.

From Figure 1.1.4, starting from the left, clean silver represents the excellent condition of lubricant oil, which means near perfect combustion. The middle image represents the medium condition post usage. It coloration is slightly darker relative to the image on its left (prior to usage). The image on the right, however, is darker, signifying soot contamination. The presence and contamination of soot on lubricant oil in engines have been the subject of many studies [8,14–17]. Fundamental studies for soot reduction is regarded as essential. The results of this work is expected to be of use when intending to mitigate/eliminate the effect of soot on

people, the environment, and engines.

AD systems   **Examples -Diesel Engine**

IC: 0.8 MD: 95 DP: 4 | IC: 0.4 MD: 85 DP: 6 | IC: 3.5 MD: 75 DP: 87

o Good combustion and good dispersancy.

o Slight decrease of dispersancy.
o Probable engine temperature problem.

o Very high quantity of soot.
o Too long between oil change

www.adsystems-sa.com

Fig. 1.1.4 Effect of soot on lubricant oil [13].

1-2 Motivation

Jess et al. [18] pointed out that petroleum-based fuel meets ~80 % of energy demands, which is expected to increase in the near future. As such, this work is concerned with:

1) Petroleum-based fuel as an energy source decreases annually, which could affect future generations.

2) Combustion product from petroleum-based fuels such as NO_x, SO_x, and soot (particulate matter). This study focuses mainly on soot.

In order to deal with the first problem, many researchers search for renewable alternatives, such as biofuels. Renewable energy sources can be used indefinitely while also being environmentally friendly [18]. The International Energy Agency (IEA) [19] reported that by 2050, biofuels usage will increase from 2 % to 27 % in the context of global transportation. Furthermore, the European Union (EU) project that by 2020, 10 % of their energy source in the transportation sector will be made up of biofuel sources [20]. This projection implies the suitability of biofuels as an alternative to diesel, kerosene, and jet fuel. The applicability of biofuels not only solve the first problem, it also indirectly solves the second problem. Its environmental friendliness would reduce the formation and accumulation of soot, which forms the focus of this study.

Butanol, as a second-generation biofuel, is being explored by researchers as a potential alternative fuel source in the future. Furthermore, butanol, as an oxygenated fuel, is known for its ability to reduce soot emission [21,22]. Oxygenated fuels contains oxygen, which aids the oxidation process and lower soot emission, as per [23–26] (experimentally) and [27,28] (computationally). Miyamoto et al. [23] reported that reduction of soot is due to oxygen content in the molecular structure of oxygenated fuel. However, Frijters and Baert [24] explained that there is possibility to have different efficiencies in soot reduction eventhough the oxygen content is same. Song et al. [27] conducted modelling study by using a constant-pressure reactor

model (SENKIN) to investigate the effect of oxygenated additives on aromatic species in fuel rich, premixed ethane combustion. Computational results showed that soot precursors reduction by structure of the oxygenated fuels are related to the effects of enthalpy formation. Westbrook et al. [28] reported that difference in the molecular structure of the oxygenated fuels influenced the efficiencies of soot reduction. The effectiveness of butanol as oxygenated fuel in this context prompted its selection for use in this work.

1-3 Butanol as oxygenated fuel

Butanol, as an oxygenated fuel, is environmental friendly and could potentially replace fossil fuels in the future. Butanol can produce ~90 % of the energy that can be produced from petrol [29], which makes it suitable as a fuel on its own or as an additive. Butanol is produced by fermenting various organic materials, such as corn, wheat, and sugar canes [30,31]. It can also be procuced via non-fermentative synthesis [32]. Butanol has four types of isomers; *n*-butanol, 2-butanol, iso-butanol, and tert-butanol. The molecular structures of these isomers are shown in Fig. 1.3.1.
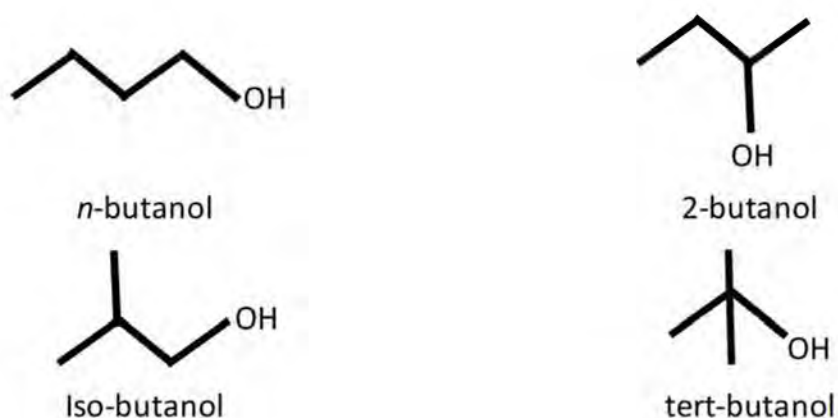
Fig. 1.3.1 Isomer structures of butanol.

The potential of butanol as an oxygenated fuel is currently being studied [33–37]. Some researchers studied combustion of butanol in jet stirred reactor [38], ignition delay in shock tube [39,40], and auto ignition of butanol isomers/*n*-heptane blend fuels in a rapid compression machine [41,42]. Chemical kinetic mechanisms were also developed to elucidate the reactions involved in the combustion of butanol [43,44]. Combustion of butanol as a fuel or a mixing agent with gasoline in engines were also experimented upon [45–51]. Due to promising results and the purported advantages of butanol, companies such as BP and Dupont are collaborating to produce bio butanol from British Sugar ethanol [52].

The properties of gasoline, diesel, methanol, ethanol, and butanol are compared and tabulated in Table 1.3.1, followed by details pertaining to the advantages of butanol relative to methanol and ethanol.

Table 1.3.1 Properties of gasoline, diesel, methanol, ethanol and butanol [30, 53].

Fuel	Research octane number, RON	Cetane number	Saturation pressure at 38 °C [kPa]	Volumetric energy density [MJ/L]	Lower heating value [MJ/Kg]
Gasoline	92-98	0-10	31.01	32	42.7
Diesel	20-30	40-55	1.86	32-40	42.5
Methanol	136	3	31.69	16	19.9
Ethanol	129	8	13.8	20	28.9
Butanol	96	25	2.27	29	33.1

The advantages of butanol include:

a. The cetane number of butanol exceeds both methanol and ethanol, while its RON number is almost similar to gasoline. Therefore, it can function as an additive to gasoline at lower or higher concentrations.

b. The saturation pressure of *n*-butanol is inversely proportional to carbon atoms, which menas that butanol has a lower volatility and lack vapor lock problems.

c. Its longer number of carbon atoms increases its (lower) heating value. Thus, the energy density of butanol exceeds that of methanol and ethanol, which results in better ignition performance during cold starts while also minimzing the usage of fuel.

d. Butanol is safe for consumption as it is less corrosive when transported in pipelines.

e. Butanol has higher oxygen content relative to biodiesel, which reduces the formation of soot.

1-4 Soot formation phenomenon

Prior to discussing the methods used in this study, it is crucial to understand how soot forms. Earlier studies reported soot formation as a complex process [34,54]. This chapter details the formation of soot and the associated processes. Soot is an incomplete combustion product formed from fuel-rich conditions. Soot formation, beginning from the decomposition of hydrocarbon fuel to carbonaceous agglomerate, reports millions of carbon atoms.

Rubino et al. [55] and Bockhorn [56] posited four main steps in soot formation. (1) Precursor formation, (2) particle inception, (3) particle growth, and (4) particle oxidation. Figure 1.4.1 depicts the soot formation process, starting from precursor formation by oxidation with hydrocarbon fuel, forming small hydrocarbon radicals, such as acetylene (C_2H_2), ethylene (C_2H_4), and C_3H_x.

Coagulation/
Agglomeration

Condensation

Surface growth

Particle inception

C_6H_6 $C_{10}H_8$

$C_{14}H_{10}$

Aromatics formation

Formation of linear hydrocarbons:
C_2H_2, C_2H_4, C_3H_x, C_4H_x, etc
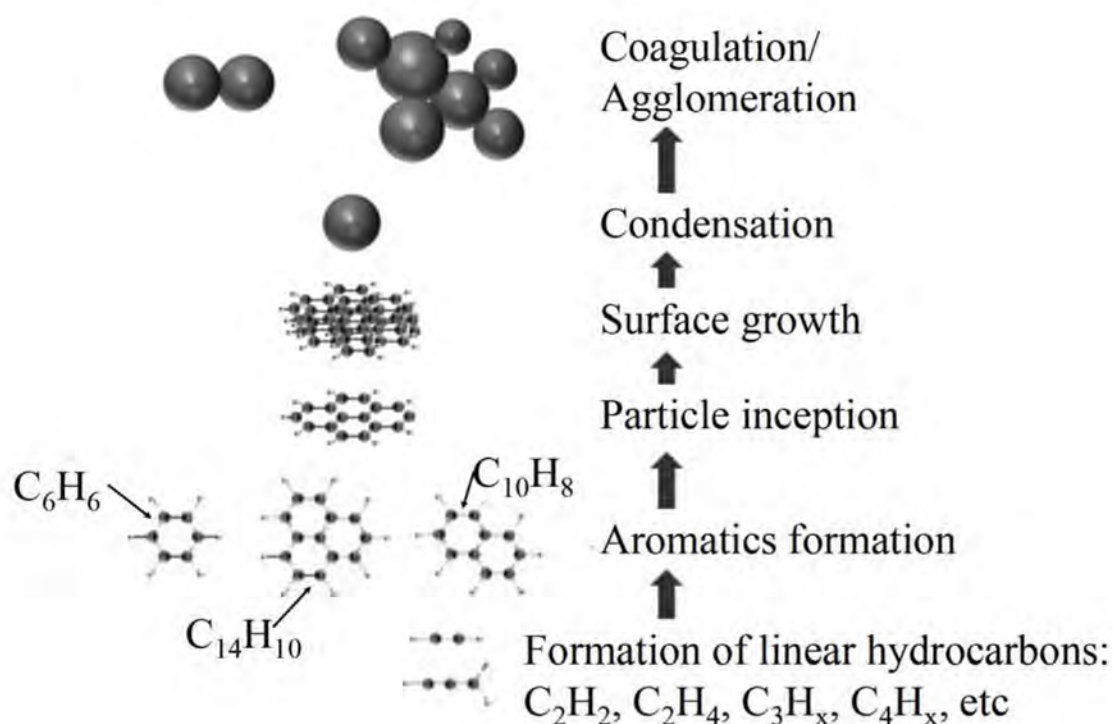
Fig. 1.4.1 Soot formation and reduction process [57].

These small hydrocarbons react with other hydrocarbons, producing larger PAHs such

as benzene (C_6H_6) and naphthalene ($C_{10}H_8$). This process, which involves two step reactions consisting of hydrogen abstraction and reaction with C_2H_2, is known as the "Hydrogen abstraction acetylene addition" (HACA) mechanism [58], illustrated in Fig. 1.4.2.

After the formation of aromatics, particle inception takes place. During this process, the condensation process of gas-phase to solid-phase condition with the particles' diameter measuring less than 1.5 nm takes place. Particle growth reaction involves surface growth and coagulation/agglomeration process, which further increases the diameter of the particles. Surface growth is a reaction between gas-phase species and the surface of the particles, while the coagulation process is a break up and combine process. The latter forms the final size of the soot particle, which could potentially reach ~50 nm.

It can be surmised that C_2H_2 and larger PAHs are important towards the formation of soot. This study measure these species, and their characteristics will be elucidated in the next chapter.
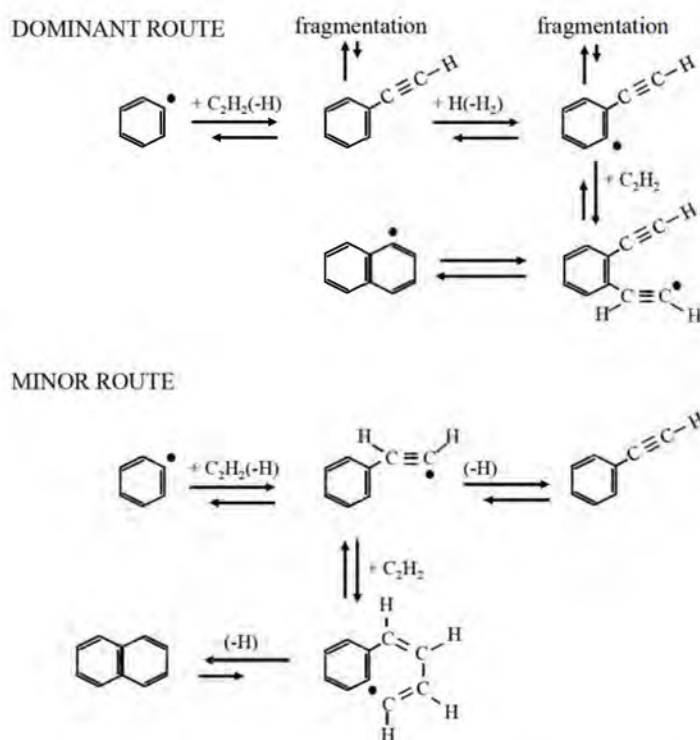
Fig. 1.4.2 Hydrogen abstraction acetylene addition (HACA) mechanism [58].

1-5 Sooting tendency

Sooting tendency is also a crucial component of soot reduction studies. Sooting tendency explains the sooting behavior of the tested fuels. The earliest study of sooting tendency was conducted by Kewley et al. [59] in 1927. They utilized a small lamp to measure the height of the flame to identify the sooting tendency from 10 mm to 32 mm. However, Minchin [60] disagrees with Kewley et al. [59] due to the fact that not all fuels are covered within the 10-32 mm length, with some fuels are beyond the scale used in that work. Due to the non-inclusivity of the scale, a new definition of sooting tendency, S_t, was proposed:

$$S_t = \frac{K}{SP}$$

Here, SP stands for the smoke point, which represents the highest flame without smoking when the tested fuel is combusted, while K is a constant set to 320. Mitchin et al. [60] pointed out that sooting tendency is proportional to the aromatic content of a fuel, which implies that an increase in the aromatic content leads to higher sooting tendency.

Clarke et al. [61] conducted sooting tendency experiments for 115 compounds, encompassing hydrocarbons, alcohol, ketones, and others using a new smoke point lamp setup by the Institute of Petroleum, encompassing a scale from 9 to 450 mm. The smoke point values were used to determine the sooting tendency, and their results show that the oxygenated fuel reduces sooting tendency. Olson et al. [62] concluded that the structure and composition of fuel plays an important role in sooting tendency. However, the unfixed smoke point value and behavior of molecular structure in many studies are inconsistent [63–65], and due to this, in 1983, Calcote et al. [66] introduced the threshold sooting index (TSI), as per the following equation:

$$TSI = a - b * \emptyset_c$$

Here, a and b are constant values, where according to [67], $a = 219$ and $b = 101$, while $\emptyset_c$ is the C/O ratio. TSI was determined to be within 0 - 100. For example, ethane was identified as the least sooting, with TSI = 0, while methylnaphthalene reported the highest sooting, with a TSI = 100. Higher values of TSI indicate that the fuel has higher sooting tendencies. However, the TSI method is not without flaws. First, the order of sooting tendency by TSI is strange, since it shows alkynes with lower sooting behavior than alkenes and alkanes, as per Fig. 1.5.1.
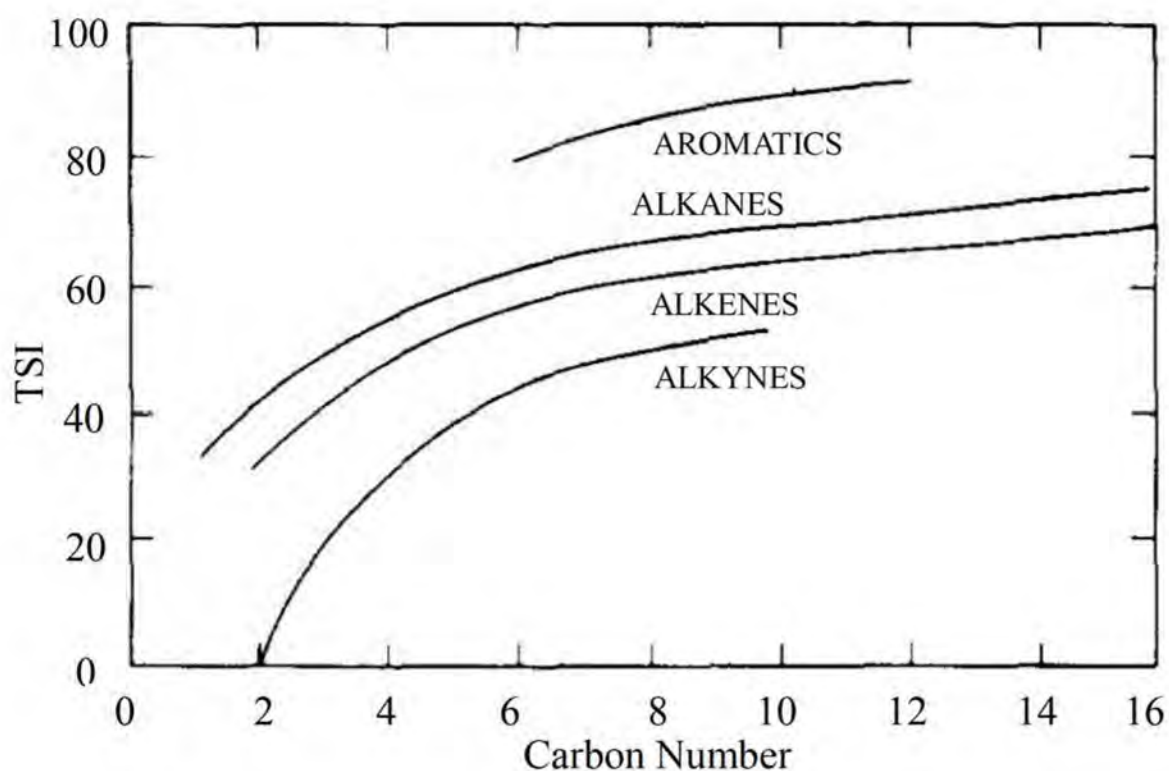
Fig. 1.5.1 TSI behavior for aromatics, alkanes, alkenes and alkynes [62].

For example, acetylene (C_2H_2), which is an alkynes, is expected to be more sooting relative to alkenes and alkanes. This is due to acetylene being widely accepted as a main soot precursor [68,69]. Hence, the correct order should be aromatics > alkynes > alkenes > alkanes, as per [70]. As shown in Fig. 1.5.1, TSI was developed only for pure hydrocarbons, and not for oxygenated fuels. Since our group focuses on the sooting tendency of butanol as oxygenated

fuel, therefore, the application of TSI in this study is irrelevant.

In 1993, Hamins [70] concluded the ranking of sooting tendencies for polyaromatics, aromatics, alkynes, alkenes, alkanes, and alcohol. He confirmed that alcohol has the lowest sooting tendency, while polyaromatics have the highest sooting tendency. Therefore, the ranking of sooting tendencies are as follows:

Polyaromatics > aromatics > alkynes > alkenes > alkanes > alcohols.

Based on this supposition, alcohol is identified as a potential fuel for the reduction of soot emmission. Butanol from the alcohol group is used in this study as a fuel by mixing it with *n*-heptane to determine its sooting tendency.

Several studies were performed to demonstrate the fact that the equivalence ratio can also be used to describe sooting tendency [71,72]. The smaller equivalence ratio at the sooting limit region implies that the fuel has higher tendency to soot. Most critical equivalence ratio experiments are conducted at high temperature. For example, Harris and Al [71] performed the critical equivalence ratio for five types of fuels (methane, ethane, propane, etylene, and acetylene) at 1,600 - 1,800 K. Ergut and Pickens [72] also carried out experiments to determine the effect of the equivalence ratio on soot formation behaviours at high temperatures (~1,900 K). The aforementioned studies confirmed that temperature is crucial towards sooting tendencies. However, most previous studies focused on higher temperatures, and only a few covered experiments at temperateures lower than 1,400 K.

In order to determine the sooting tendency of the tested fuels, the temperature of the flame needs to be fixed, as it is the only way to pinpoint the effect of temperature/structure for further analyses. This study focuses on investigating sooting tendencies at temperatures lower than 1,400 K, where the temperature will be kept constant using a hydrogen/air burner. Nakamura et al. [73][74] and Dubey et al. [75] pointed out that this method managed to maintain the temperature throughout the experiment in the micro flow reactor with a controlled

temperature profile (MFR).

To gain a more detailed insight into the parameters outlined in previous studies, a three-dimensional graph of fundamental studies including multiple equivalence ratios, temperatures, and pressures for heptane and butanol were plotted, and is shown in Fig. 1.5.2. Previous studies mostly investigated lower equivalence ratios which were under 2.0. This could be due to the difficulty associated with handling stable premixed flames at higher equivalence ratios. However, the current work explores the usage of higher equivalence ratios (2.0 - 5.0), which sets it apart from previous studies. This avenue was pursued in this work due to the capability and advantages of the MFR in carrying out experiments at wider equivalence ratios relative to other reported methods. Previous studies reported significant progress in covering an approximate range of temperatures (500 – 2,000 K) and pressures (1 - 10 atm).
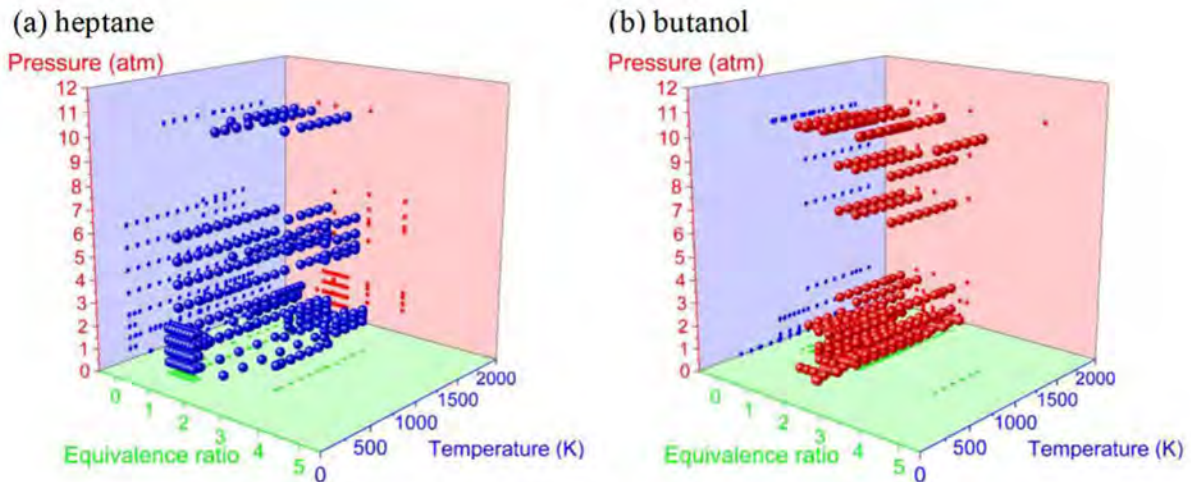
Fig. 1.5.2 Parameter ranges of pressure, equivalence ratio, and temperature studied for (a) heptane and (b) butanol. Data were from Ingemarsson et al. [76], Davidson et al. [77,78], Smallbone et al. [79], Yao et al. [80], Akih-kumgeh and Bergthorson [81], Yamamoto et al. [82], Herbinet et al. [83], Sileghem et al. [84], Hakka et al. [85], Seidel et al. [86], Tekawade et al. [87], Loparo et al. [88] and Savard et al. [89] studied for (a) heptane and Dagaut et al. [90], Sarathy et al, [37], Black et al. [44], Togbé et al. [91], Oßwald et al. [92], Cai et al. [93], Zhang et al. [94], Hansen et al. [95], Braun-unkhoff et al. [96] and Tran et al. [97] for (b) butanol.

This study also focuses on a maximum wall temperature of 1,100 K and atmospheric

pressure by using the MFR, where soot formation could be prevented even at higher

equivalence ratios, which would allow for the species measurement of the formation of PAHs

and soot precursors at atmospheric pressures and under 1,100 K for extremely fuel rich

conditions.

1-6 Micro flow reactor with a controlled temperature profile (MFR)

The MFR is a method derived from micro combustion research [98–103]. Numerous research in micro combustion has been performed, with many insightful contributions towards the development of higher energy density and improved efficiency of the energy conversion system. Attention on micro combustion study to produce small scale device with long-life time and good thermal efficiency is increased [104]. One of the pioneering approach to improve thermal efficiency management by decreasing heat loss was combination of swiss-roll burner and thermoelectric by Ronney [105].

In order to further investigate micro combustion, Tohoku University group designed and produced several scales of disk-shaped swiss-rolled micro combustors, shown in Fig. 1.6.1.
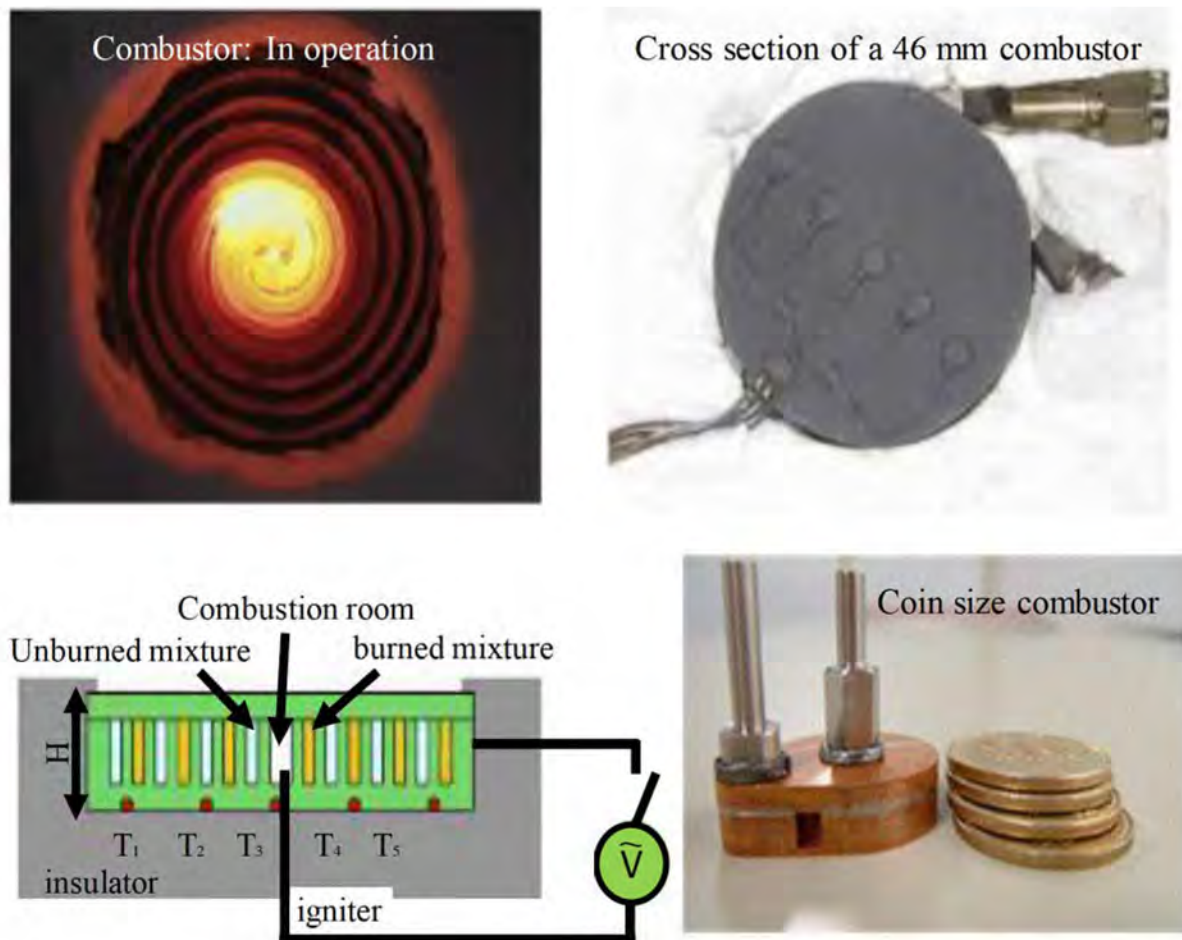
Fig. 1.6.1 Disk shaped swiss-roll combustor by Tohoku University group [102][106][107].

The swiss-rolled micro combustor applies recirculated heat from the burned gas to the unburned gas. Figure 1.6.1(a) demonstrates that a flame was stabilized in the swiss-rolled combustor. Positions of thermocouples in the swiss-rolled combustor are shown in Figure 1.6.1(b) Top view and (c) Cross section of a swiss-rolled combustor. Four sizes of prototype of swiss rolled combuster were fabricated. These four sizes of prototype have outer diameter of 64 mm, 45 mm, 26 mm and 20 mm. One of the combustor that has outer diameter of 20 mm is shown in Fig. 1.6.1(d). Besides development of disk shaped swiss–roll combustor, knowledge of stationary premixed flames in small tubes is also important. Therefore flame studies in MFR have been carried out. Explaination about MFR as follows.

The main part of the MFR is a quartz tube, which functions as a reactor, where the combustion and flame characteristic phenomena can be observed in the reactor. The diameter of this reactor is smaller relative to the normal quenching diameter. Stationary wall temperature can be observed along the axial direction when the reactor is heated. The reactor is heated by external heat source, which is either an electric heater [73,98] or a hydrogen air burner [74,103].

Figure 1.6.2 shows a schematic diagram of the MFR profile using an electric heater [73,98] and hydrogen/air burner [74,103] as heat sources. Both show that fuel and air are flown inside the reactor, which is controlled by a mass flow controller. The flow is laminar, since it has small Reynold number, while its pressure is constant. As outlined previously, the diameter of the reactor is small, which causes the wall temperature to strongly rely on the inner surface of the wall temperature.

Earlier studies of the MFR focused on identifying weak flames produced by fuels to elucidate fuel reactivity and ignition characteristics, such as dimethyl ether (DME) [108], *n*-heptane [82], gasoline primary reference fuel (RPF) [109], *n*-heptane/*n*-toluene [110], diesel surrogate (*n*-cetane, *n*-decane, *n*-heptane, iso-cetane, and α-methylnaphthalene) [111], natural gas components (methane, ethane, propane and *n*-butane) [112], as well as syngas [113]. Previous studies also showed that the radical quenching effects of the quartz tube are negligible

[114,115].

(a) Electric heater

52.5 mm

Burned gas — 2 mm — Flame — Unburned mixture

Heaters — Microchannel — X

(b) Hydrogen/air burner

Flow

CH₄/air → 2 mm — X — Flame

Cylindrical tube — Flat flame for heating — Sintered metal

Flow H₂/air
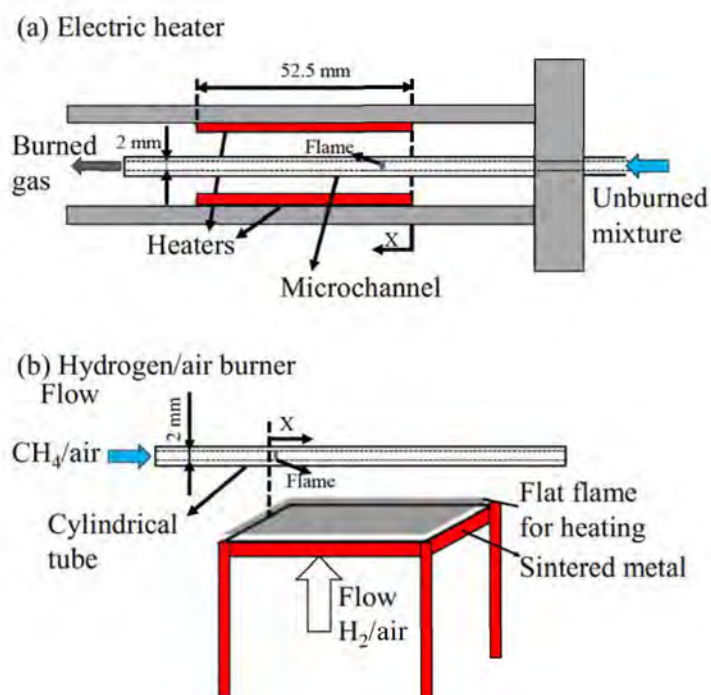
Fig. 1.6.2 (a) MFR with electric heater •• •••••••• •• •• •• •• ••• • • • • • • • •• ••••• •• • • • • • •

One of the interesting results obtained from the aforementioned studies by the MFR was the identification of three types of flame characteristic shown in Fig. 1.6.3 [108], which are (a) normal flame, (b) flame with repetitive extinction and ignition (FREI), and (c) weak flame. Stable flame of normal flame can be observed at high velocity (100 cm/s to 40 cm/s), while unstable flame of FREI (explained later) can be observed in the intermediate velocity (between normal and weak flames).

FREI is a continuous cycle phenomenon, where ignition occurs at high temperatures, then shift to lower temperatures, causing extinction. This flame was termed as the flame with repetitive extinction/ignition. In the case of low velocity (5 - 0.2 cm/s), weak flame was observed. This flame is termed weak flame due to its low luminosity. It is not visible to the naked eye and require a CH band pass filter to be seen. This filter was used to eliminate thermal radiation from the heated reactor. All of the three types of flames based on mean flow velocity and location are shown in Fig. 1.6.4.

19
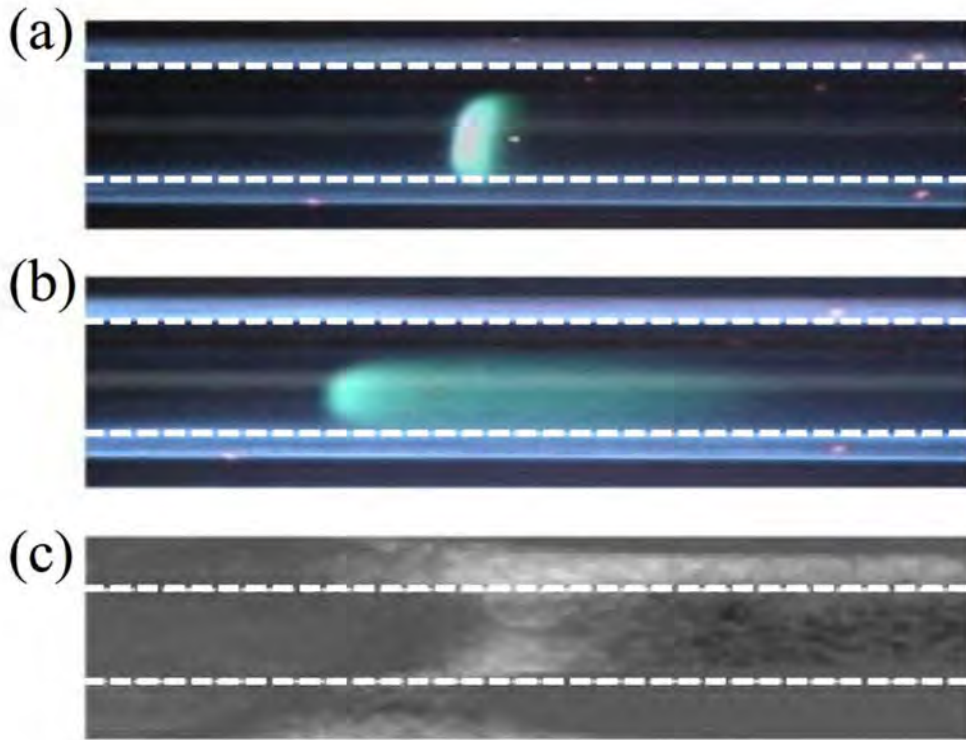
Fig. 1.6.3 (a) Normal flame (b) FREI (c) Weak flame ·· ·· .· · ·
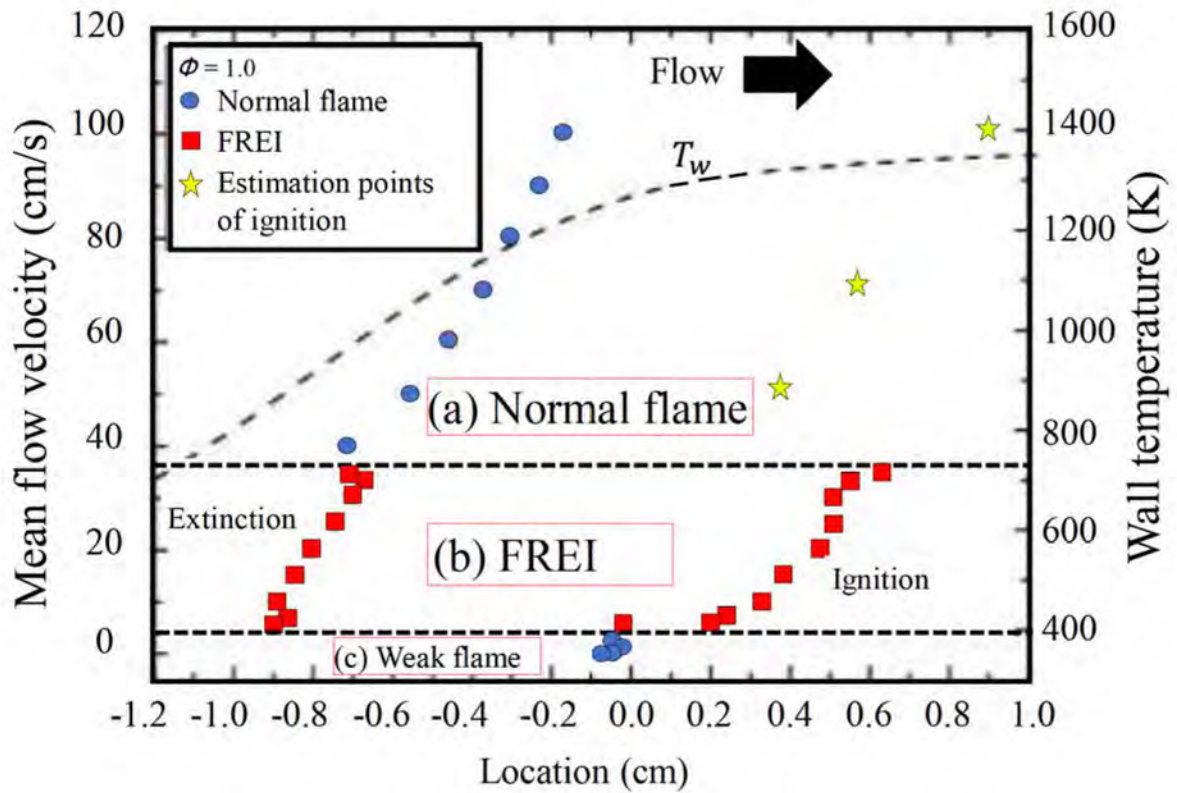
Fig. 1.6.4 Measured flame location based on type of flames ·· ··.··· · ·

Minaev et al. [116] reported that weak flame corresponds to ignition branch of the Fendell curve. This is also supported by Tsuboi et al. [100], who posited that the wall temperature at the lower limit of weak flame related to the ignition temperature of the fuel implies that the reactivity of the fuel can be determined. The weak flame is located upstream and at lower temperatures, which corresponds to a more reactive fuel.

Yamamoto et al. [82] reported that in the case of weak flame of *n*-heptane/air mixtures, transient ignition phenomena takes place, which helps in the identification of spatially separated flame consisting of cool, blue, and hot flames at different pressures, as shown in Fig. 1.6.5. The first flame was termed as the cool flame, the second was termed as the blue flame, while the third was termed as the hot flame. With increasing pressure, the cool and blue flames shift upstream, which is the low temperature region. It also shows that an increase in pressure causes the flames to become clearer.

(1) Cool flame (2) Blue flame (3) Hot flame
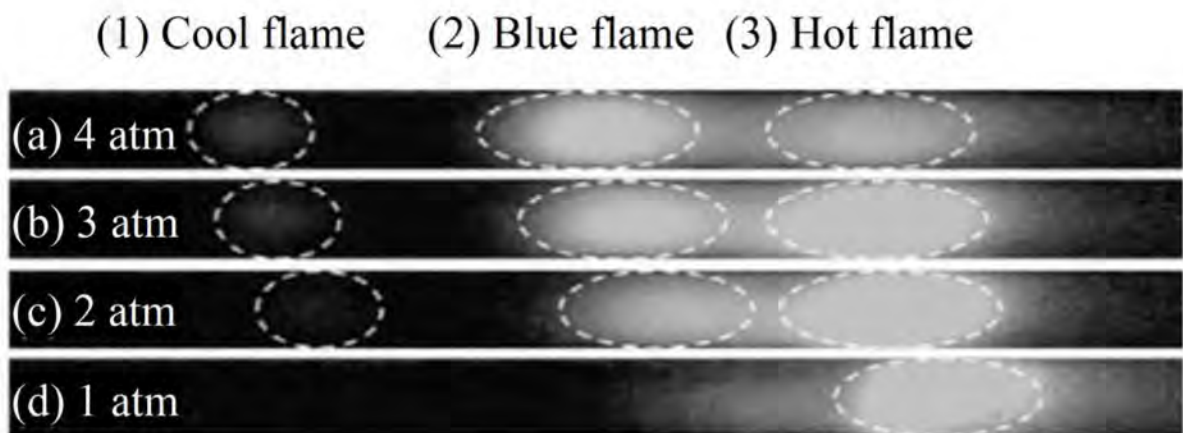
Fig. 1.6.5 Cool flame, blue flame and hot flame at different pressures • ••.••• •

MFR can also distinguish flame from soot within rich conditions [73–75,117]. Examples of flame and soot response with temperature profile is shown in Fig. 1.6.6, where (a) shows the luminosity of soot formation, (b) shows only the flame, while (c) shows none.

These types of flame and soot responses are plotted on the regime map of flame and

soot response, which relies on the inlet mean velocity and equivalence ratio shown in Fig. 1.6.7.

Based on this regime map, the critical sooting equivalence ratio can be identified.
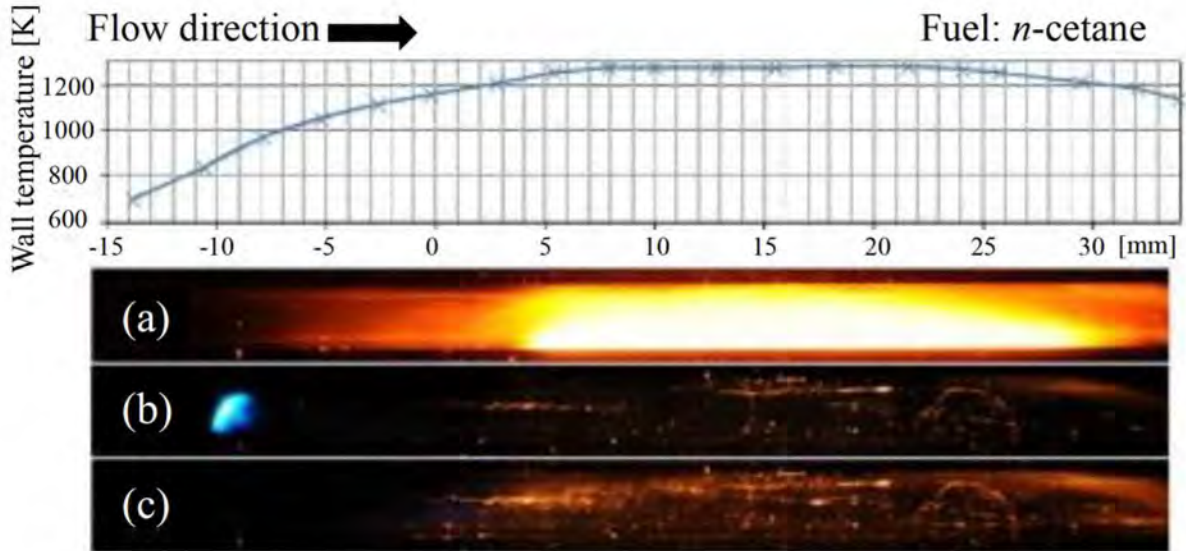
Fig. 1.6.6 Flame and soot response: (a) Soot, (b) Flame (c) None for *n*-cetane/air mixtures • • • • • • • • •
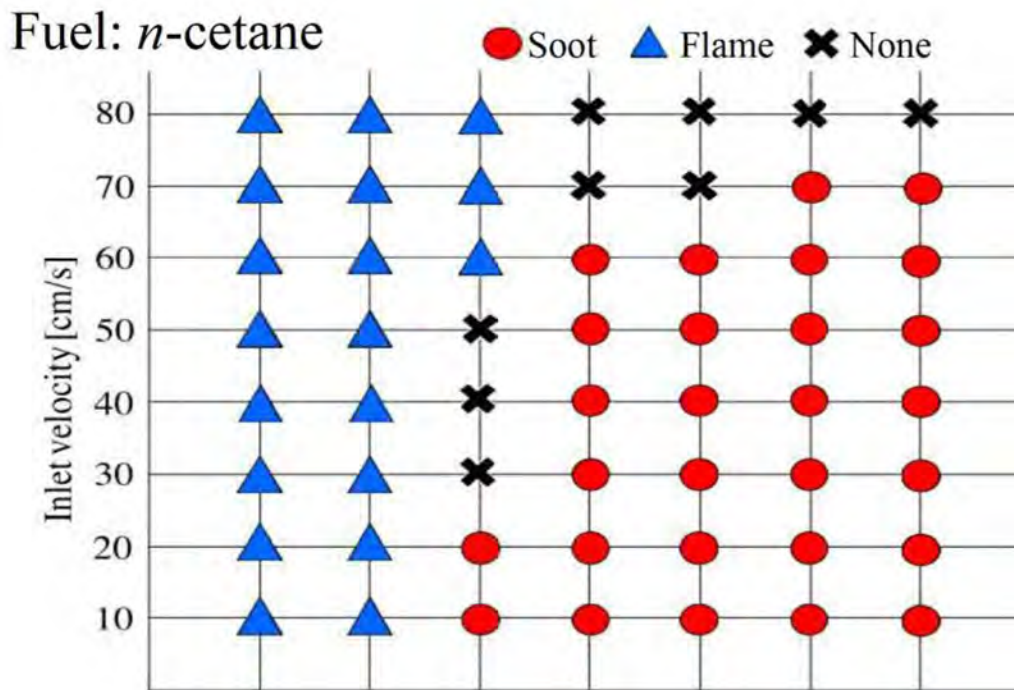
Fig. 1.6.7 Regime map of flame and soot responses • • • • • • • • •

The function of the MFR was extended to measure small hydrocarbons [117] and PAHs [73,74]. The MFR was connected to a Gas Chromatography/mass spectrometry GC/MS (Agilent 7890/5975). In Nakamura et al. [73], major species of PAHs formation from acetylene/air mixtures, such as benzene, styrene, naphthalene, phenanthrene, indene, acenaphthylene and biphenyl were measured at high equivalence ratios and different temperatures. This confirms that the MFR can be used to elucidate the temperature dependence of PAHs formation. Nakamura et al. [74] also reported results pertaining to species measurement of PAHs, such as benzene, toluene, styrene, indene, napthalene, biphenyl, acenaphthene, fluorene, and phenanthrene in the case of more complicated fuels (*n*-cetane and *iso*-cetane). These species measurements result is shown in Fig. 1.6.8, and determined the influence of fuel molecular structure on the formation of PAHs. The concentration of PAHs for *n*-cetane exceeds that of *iso*-cetane. This work utilized the MFR to measure small hydrocarbons and PAHs, even in the case of heavy and complicated fuels.
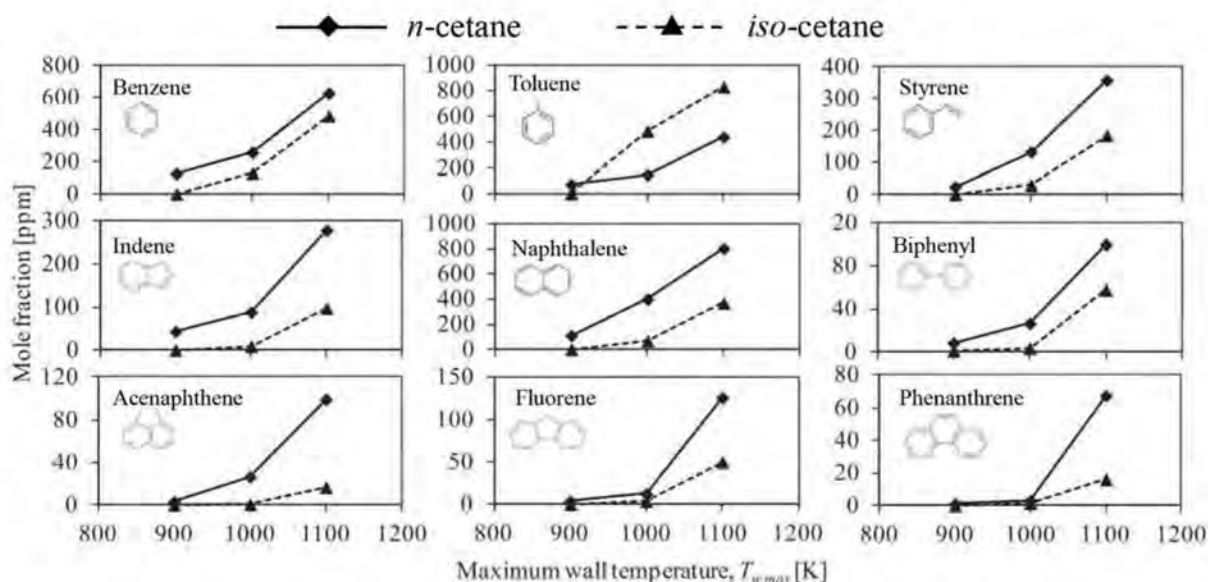
Fig. 1.6.8 Species measurement of mole fractions of PAHs • • • • • • • • •

According to Dubey et al. [75], the MFR can distinguish three phases of soot formation

behaviors, which are flame and aromatic precursor formation, small aromatics formation, and large PAHs and soot formation, as per Fig. 1.6.9. These features is important for species measurement analyses, which has been conducted in earlier studies. By controlling the temperature, the formation of soot can be prevented, and the experiment can then focus on measuring only the concentration of PAHs. The application of MFR is expected to be further developed to the point that it becomes the best method for investigating flame chemistry, PAHs, and soot formation behavior in the near future.
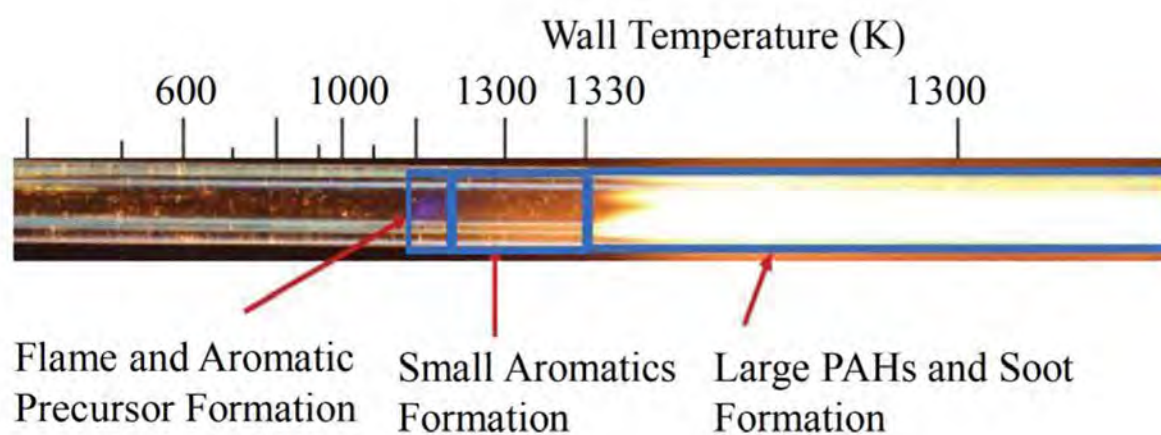
Fig. 1.6.9 Soot formation phases [75].

1-7 Research objectives

The objectives of this study are to gain a deeper understanding of the effect of the addition of butanol to sooting limit and PAHs formation of *n*-heptane. The specific objectives are:

a) To analyze sooting tendency of *n*-heptane with *n*-butanol addition at temperatures lower than 1,400 K. Comparison of pure *n*-heptane, pure *n*-butanol, and mix of both fuel will result in new insights into sooting tendencies.

b) To conduct species measurement of small hydrocarbons of C_1 and C_2, larger hydrocarbon, and PAHs formation species on the effect of the addition of *n*-butanol. The species are important due to their contributions to soot formation.

c) To understand the effect of the addition of *n*-butanol on *n*-heptane, the reaction path and rate of production analyses were conducted. Hence, major reactions contributing to the reduction of PAHs concentration can therefore be identified.

1-8 Structure of the thesis

Chapter 1: Introduction

This chapter details the background and motivation of this study, and literature pertaining to butanol as oxygenated fuels, phenomenon of soot formation, as well as sooting tendencies. Earlier studies on MFR were also detailed. This was then followed by outlining the objectives of this study.

Chapter 2: Sooting behaviour of *n*-heptane with butanol addition

This chapter details the experimental apparatus (MFR) and its associated procedures. This was followed by discussion pertaining to the computational method, encompassing energy equation, modifications, parameters, and other factors. Sooting limits and the influence of increasing equivalence ratio on soot formation behaviors were also elucidated. The chapter ends with the discussion of the validation of mechanisms for flame positioning.

Chapter 3: Validation capability of existing mechanism

This chapter details the validation of multiple mechanisms with the measured sample gases results of small hydrocarbons $C_1 - C_2$ formation, such as ethylene (C_2H_4), acetylene (C_2H_2), ethane (C_2H_6), methane (CH_4), carbon monoxide (CO), and carbon dioxide (CO_2). This was followed by the validation of, larger hydrocarbons and PAHs such as benzene (C_6H_6), phenol (C_6H_5OH), benzaldehyde (C_7H_6O), toluene (C_7H_8), ethylbenzene (C_8H_{10}), styrene (C_8H_8), and naphthalene ($C_{10}H_8$). This chapter ends with a discussion on the effect of the addition of butanol on the measured species.

Chapter 4: Reaction path and rate of production analyses

This chapter explains the experimental results of the reaction path from the computational results reported by the mechanisms. The explanation detail the differences between *n*-heptane and the addition of butanol to *n*-heptane via reaction path and the rate of

production analyses.

Chapter 5: Summary and Conclusions

This chapter concludes this study.

Chapter 2

Sooting behaviour of *n*-heptane with butanol addition

2-1 Introduction

This chapter discusses the effect of the addition of butanol on the flame and soot response of *n*-heptane using MFR. Nakamura et al. [73][74] and Dubey et al. [75] reported that MFR managed to elucidate flame and soot responses for multiple equivalence ratios. At the lowest equivalence ratio, only the flame can be observed, however, soot is evident when the equivalence ratio increases. The determination of the flame and soot response is important towards determining the critical equivalence ratio.

Here, the critical equivalence ratio means the beginning of soot formation at its lowest equivalence. Each fuel have different starting point of equivalence ratios for soot formation; if it is higher, it means that the fuel has a lower sooting tendency, and vice versa.

The maximum wall temperature for investigating the sooting tendency in this work was set to 1,300 K, which is lower relative to other studies. Moreover, Wang et al. [118] and Pickett et al. [119] reported that soot formation is difficult at temperatures lower than 1,400 K, except if the process takes place an MFR, setting it apart from the traditional methods involved in soot formation.

The length of the sooting region can also be used to quantitatively demonstrate the

28

formation of soot. The length of sooting region was used in this work to investigate the effect of increasing equivalence ratios and the mole percentages of butanol. A fuel with a shorter length of sooting region produces less soot, and vice versa.

This chapter also discusses the validation of the capability of the mechanisms by comparing the maximum heat release rate (HRR) of the computation with the flames position in the experiment. The flame position can be determined using the peak position from the luminosity profile of the captured image. In the case of computations, the flames positions in the MFR were modelled using a one-dimensional steady state condition. The detail of the experiment and computational methods are explained in the next section.

2-2 Experimental setup for flame and soot response observation

2-2-1 Micro flow reactor with a controlled temperature profile (MFR)

Figure 2.2.1 shows the schematic diagram of the micro flow reactor with a controlled temperature profile (MFR). The MFR consists of a quartz tube with an internal diameter of 2 mm, which is smaller than its quenching diameter. It is heated by an external heat source from a hydrogen/air burner (Fig. 2.2.2 (a)), and forms a stationary wall temperature profile along the inner surface of the quartz tube. The hydrogen/air burner was used as it provides a better visualization of chemiluminescene from the hydrocarbon flames in the MFR. The flow rate of hydrogen and air is controlled via two separated mass flow controllers (Fig 2.2.2 (b)) for setting the maximum wall temperature profile, $T_{w,max}$. When the desired temperature is achieved, the flow of both mass flow controllers are fixed.
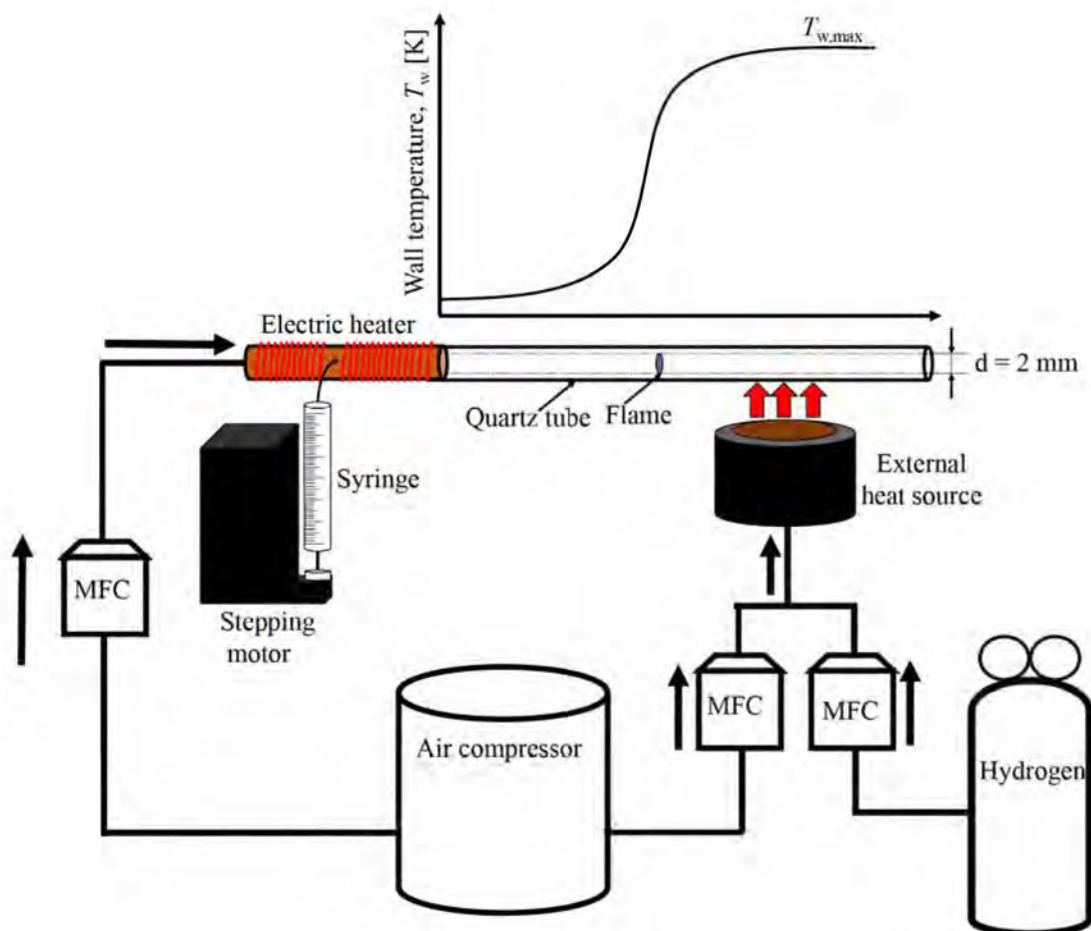
Fig. 2.2.1 Schematic diagram of the MFR.

In this work, high purity of *n*-butanol (99 % pure) and *n*-heptane (99 % pure) purchased from Wako Pure Chemical Industries, Ltd were used. *n*-heptane and *n*-butanol were mixed in liquid state at multiple mole percentages, where pure *n*-heptane is denoted by hp100, 50 % mole percentage of *n*-heptane + 50 % mole percentage of *n*-butanol is denoted by hp50bt50, and pure *n*-butanol is denoted by bt100. Mixtures of pre-mixed fuel and air was passed inside the MFR. A 500 μL micro syringe (Hamilton 1750RN) was used to inject fuel(s) into the upstream region of the MFR. The amount of fuel injected is controlled using a stepping motor (Fig. 2.2.2 (c)), while air is controlled by the mass flow controller (MFC) (KOFLOC 3200) (Fig. 2.2.2 (d)).
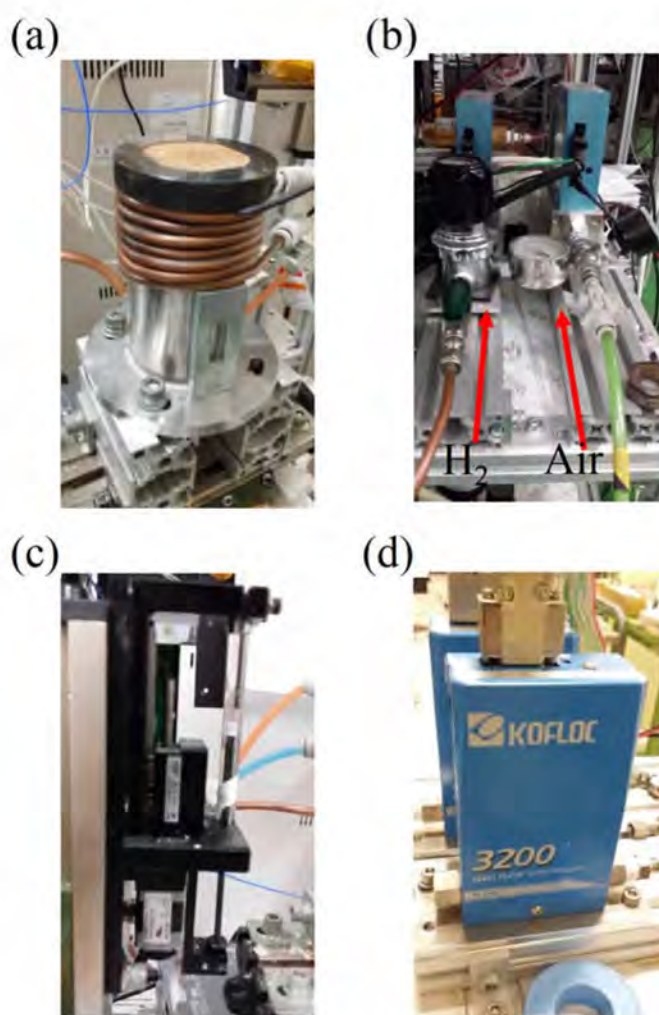
Fig. 2.2.2 (a) Hydrogen/air burner (b) Mass flow controller for hydrogen/air burner (c) Stepping motor and syringe (d) Mass flow controller to control flow of air.

The MFC is calibrated by the film flow meter (HORIBA) prior to using it with the MFR. An electric heater is used to control the temperature (313 K to 343 K) of air. It is covered at the upstream region of the MFR for heating the upstream mixing zone to completely vaporize the liquid fuels prior to it entering the MFR. An appropriate combination between the given heating temperature and fuel supply were tested in advance. Complete vaporization is confirmed by observing the stable flames in the MFR.

The wall temperature of the inner surface of the quartz was measured using a K-type thermocouple inserted from the outlet of the tube. The wall temperature profile is shown in Fig. 2.2.3. The maximum wall temperature, $T_{w,max}$, of 1300 K, was fixed. The same temperature profile was also used in the computation approach.
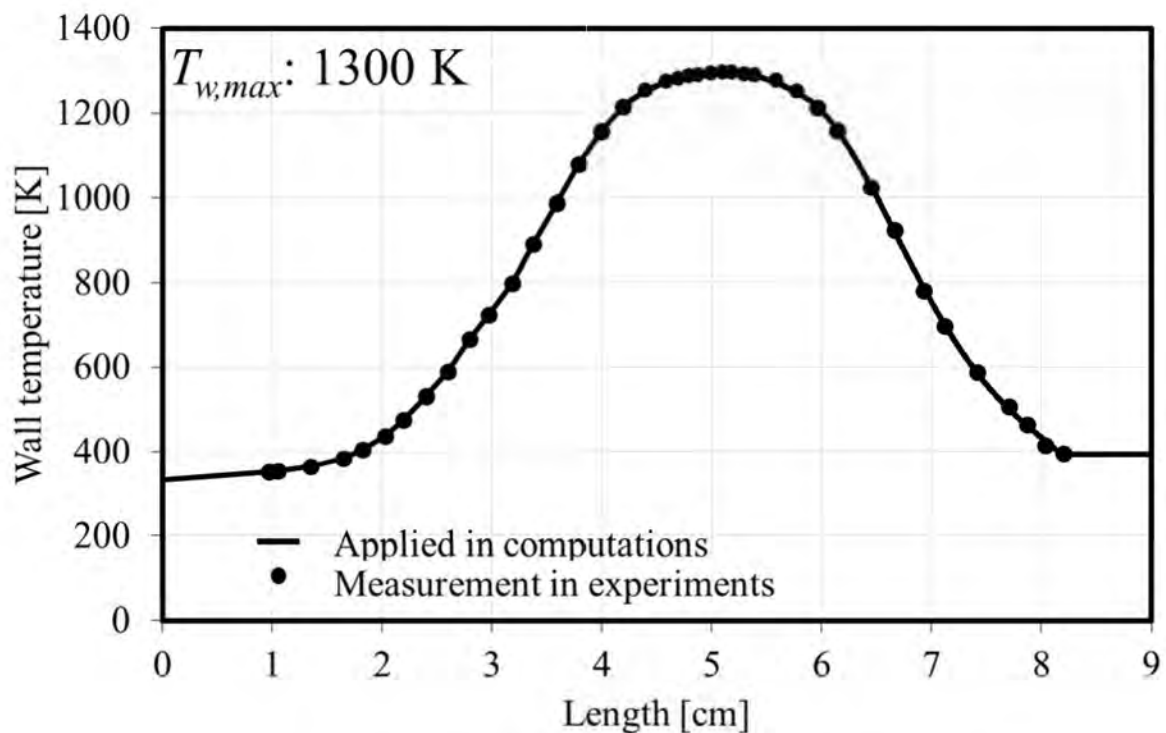
Fig. 2.2.3 Temperature profiles for sooting limit experiment.

The experiments were performed at different equivalence ratios, ϕ, at 1.5 - 4.5 and an inlet mean velocity, U_0, of 10 cm/s at atmospheric pressure. The images of the flame and soot

were obtained using a digital still camera (Nikon D300). To better visualize the flames position,

an optical band-pass filter (transparent wavelength: 431.4 nm, half bandwidth: 6.4 nm) was

used with the camera. The filter eliminates the thermal radiation from the heated quartz tube

along with the maximum luminosity from the flame, confirming that the flames position are

established. For better visualization of the flame images, the background image was subtracted

from the captured images.

2-3 Computational methods

The same computational method was used in this work, as per [75,112,120]. The flow inside the MFR was modeled using a one-dimensional reactive steady flow computation based on the PREMIX package and ANSYS Chemkin-Pro v17.2. A heat convection term between the gas and wall is added to the energy equation (red dash line at the left side) Maruta et al. [98] of PREMIX to model the flow field in the MFR as follows:

$$\dot{M}\frac{dT}{dx} - \frac{1}{c_p}\frac{d}{dx}\left(\lambda A \frac{dT}{dx}\right) + \frac{A}{c_p}\sum_{k=1}^{k}\rho Y_k V_k c_{pk}\frac{dT}{dx} + \frac{A}{c_p}\sum_{k=1}^{k}\dot{\omega}_k h_k W_k - \frac{A}{c_p}\frac{4\lambda Nu}{d^2}(T_w - T) = 0$$

Here, $\dot{M}$ denotes the mass flow rate, T denotes the gas-phase temperature, x is the spatial coordinate, c_p is the specific heat at constant pressure, A represents the cross sectional area, λ represents the thermal conductivity, ρ denotes the density, Y_k denotes the mass fraction, V_k is the diffusion velocity, $\dot{\omega}_k$ represents the rate of production, h_k represents the specific enthalpy, W_k denotes the molecular weight, d is the inner diameter, Nu is the Nusselt number, and T_w denotes the wall temperature. Note that, the flow in the quartz tube is laminar and in steady state. The pressure is always constant at atmospheric pressure. The radical quenching at the wall, heat recirculation, and the Soret and Dufour effect are negligible.

The target of this computation is the region at the upstream of the soot formation, where no soot was observed, therefore, the soot model was not used in this work. However, same parameters to those used in the experiments, such as temperature, pressure, and inlet mean flow velocity were used in the computation. The measured wall temperature profile is shown in Fig. 2.2.3 (see Section 2.2). The pressure is set to atmospheric, while the inlet mean velocity is set to 10 cm/s. The computation was also performed at multiple equivalence ratios.

The computation also require a chemical kinetic mechanism. To the best of the author's knowledge, there are only two reaction mechanisms involving the oxidation of *n*-heptane and *n*-butanol, and PAHs growth. The PAHs growth begins from C_1 and C_2 hydrocarbon species, as well as larger PAHs such as naphthalene ($C_{10}H_8$), phenanthrene ($C_{14}H_{10}$), and pyrene ($C_{16}H_{10}$).

The chemical kinetic mechanisms used in this study are the Wang and CRECK mechanisms. These chemical kinetic mechanism scripts are available at (http://www.erc.wisc.edu/) for the Wang mechanism, and (http://creckmodeling.chem.polimi.it/) for the CRECK mechanism.

The Wang mechanism is a reduced mechanism made up of 76 species and 349 reactions [118]. It was developed by the Engine research center in University of Wisconsin – Madison. It consists of a combination of three parts; a reduced mechanism of gasoline primary reference fuel (PRF) developed by [121], a detailed mechanism of PAHs growth up to pyrene (A4) developed by [122], and a reduced mechanism of *n*-butanol based on detailed mechanism developed by [123]. The Wang mechanism was validated in other studies in the context of ignition delay timings by shock tubes and soot emission by constant volume chambers, and it reported excellent agreement with its experimental counterpart [118].

The CRECK mechanism is a detailed mechanism Version 1412 of fuel, which consists of 225 species and 7645 reactions [103]. This mechanism was developed by the Chemical Reaction Engineering and Chemical Kinetics (CRECK) modeling group. They developed this mechanism by combining the oxidation mechanisms of PRF and PAHs [129], alcohol [125,126], as well as esters [127]. In previous studies, this mechanism was used to measure several oxidation species of ethanol in a jet stirred reactor, and the results are in excellent agreement with that of the ignition delay time of ethanol by the shock tube [129]. The Veloo mechanism [128] and Sarathy mechanism [123] were also used in this work, but only in the case of bt100, since the mechanisms were initially developed for butanol.

2-4 Critical equivalence ratio

The critical equivalence ratio was established to define the relative sooting tendency amongst fuels in premixed flames [73–75,117]. The fuel with a lower critical equivalence ratio has a high(er) sooting tendency.

The critical equivalence ratio can be determined using the flames and soot responses. In this study, the flames and soot responses experiment were performed at a maximum wall temperature, $T_{w,max}$ of 1,300 K, equivalence ratios, ϕ, of 1.5 - 4.5, inlet mean velocity, U_0, of 10 cm/s, and atmospheric pressure. Two types of flame and soot responses were confirmed in the present direct observation, which consists of only flame and flame with soot. Figure 2.4.1 shows the representative images of the captured flame and soot responses. In order to better distinguish the flames' image from its chemiluminescence, CH filtered images and their corresponding intensity profiles are shown together. The existence and position of the flames are framed by the white dotted circles.

In Figure 2.4.1(a), only weak chemiluminescence from the flame is apparent in the CH-filtered image, however, thermal radiation from soot is not visible in the direct and CH-filtered images. In Figure 2.4.1(b), both weak chemiluminescence from the flame and thermal radiation from soot are shown. Hereinafter, the flame and soot responses depicted in Figs. 2.4.1(a) and 2.4.1(b) are denoted as "Flame" and "Flame + Soot", respectively. Furthermore, Figure 2.4.1(b) shows that the flame position is far upstream of the onset of soot formation, which indicates that fuel pyrolysis and PAHs growth occurs in the region between the flame position and the onset of soot formation. This region is considered as the target of species measurement, which will be explained in the upcoming sections of this thesis.
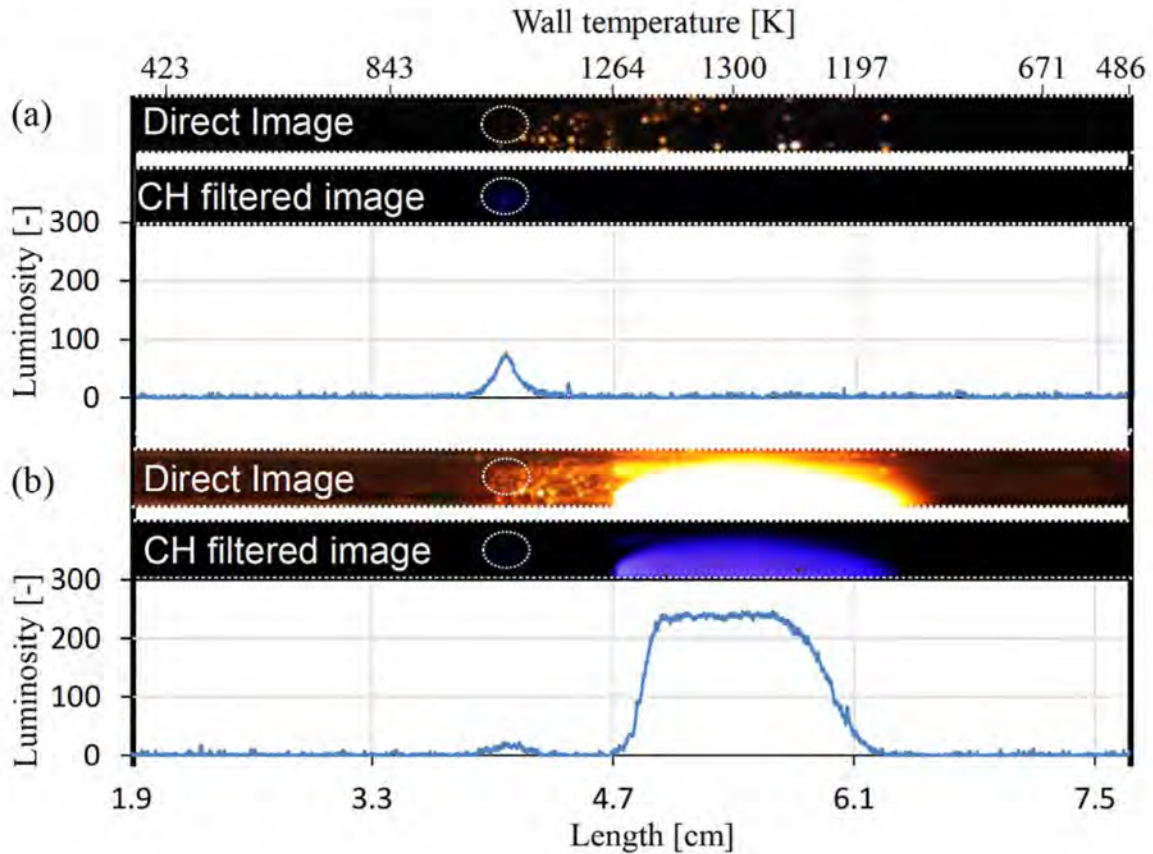
Fig. 2.4.1 Two types of flame and soot responses confirmed at $T_{w,max}$ = 1300 K and U_0 = 10 cm/s. (a) flame (hp50bt50 at ϕ = 2.1) and (b) flame + soot (hp100 at ϕ = 3.0).

Figure 2.4.2 shows a regime map of flame, as well as soot responses, with the *x*-axis representing the various equivalence ratios (1.5 - 4.0), while the *y*-axis represents the tested fuel. In the regime map, the blue triangles represent a condition where only chemiluminescence from a flame is observed, whereas a red circle represents a condition where both chemiluminescence from a flame and thermal radiation from soot are observed. Here, the border between "Flame" and "Flame + Soot" responses is evident, which is known as the critical equivalence ratio. As outlined in the previous chapter, the critical equivalence ratio plays an important role in sooting tendencies.

If the fuel has a higher critical equivalence ratio, it means that the fuel has lower sooting tendency, and vice versa. Figure 2.4.2 shows that hp100 begin producing soot at an

equivalence ratio of 2.0, while hp50bt50 does so at an equivalence ratio of 2.2, and bt100 at an equivalence ratio of 2.6. These trends show that the critical equivalence ratio increases significantly with increasing of *n*-butanol mole percentage. Therefore, the order of the sooting tendency ranking, which begins from a higher sooting tendency to the lowest sooting tendency is hp100 > hp50bt50 > bt100.
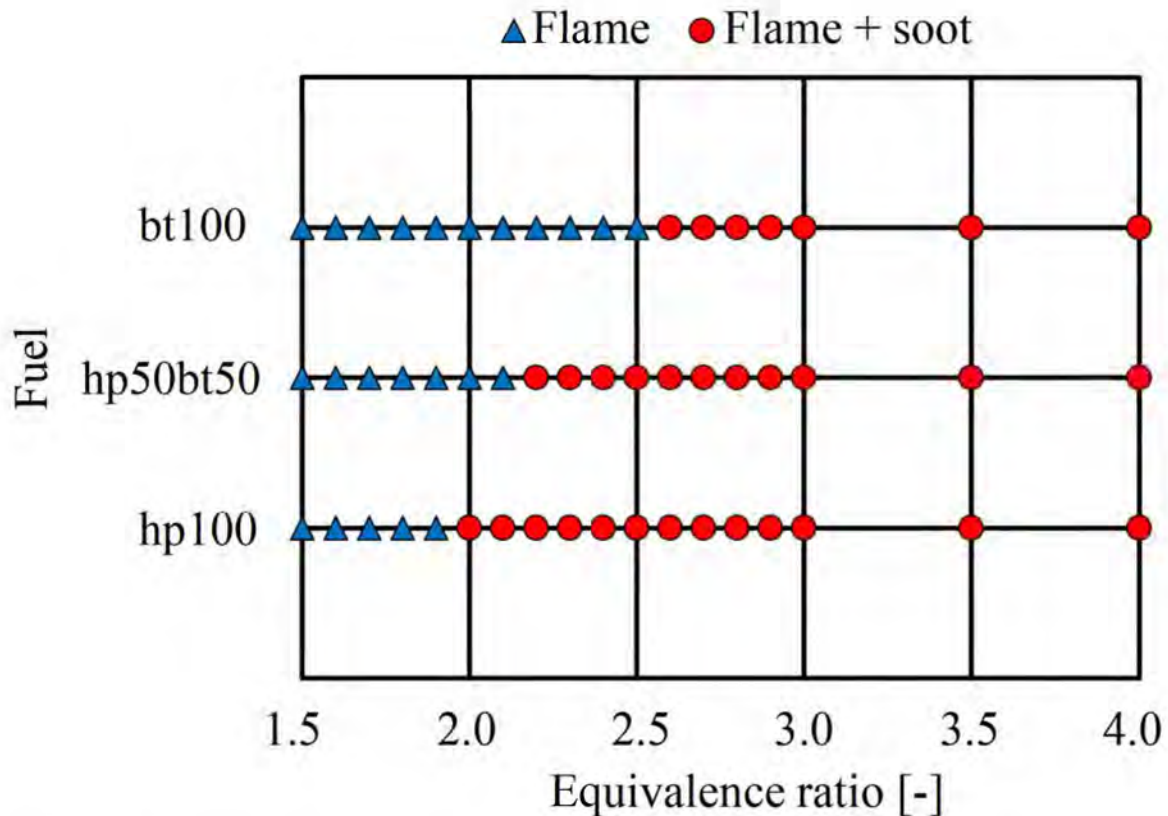
Fig. 2.4.2 Regime map of overall experimentally obtained results of flame and soot responses for hp100, hp50bt50, and bt100 with equivalence ratios in the range of 1.5 to 4.0, $T_{w,max}$ = 1,300 K and U_0 = 10 cm/s.

2-5 Sooting region length

2-5-1 Effect of an increase in equivalence ratio on the sooting region length

The length of the sooting region can be used to show the relative ease of soot formation. A longer sooting region length indicates that the fuel has higher sooting behavior. However, it should be noted that measurement of the soot formation is not done directly since it may be affected by the effect of surface reactions. It means comparison for sooting tendency may not be quantitatively showing soot formation. Figure 2.5.1 shows direct images of flames and soot responses for hp100, hp50bt50, and bt100 for equivalence ratios of 2.0, 3.0, and 4.0, respectively. As expected, the length of the sooting region in all of these cases extends with increasing equivalence ratios. For hp100, all of the values of equivalence ratios are present in the sooting region. However, at hp50bt50 and bt100, no sooting regions are evident, which confirms the potential of butanol as an oxygenated fuel for the reduction of soot formation.
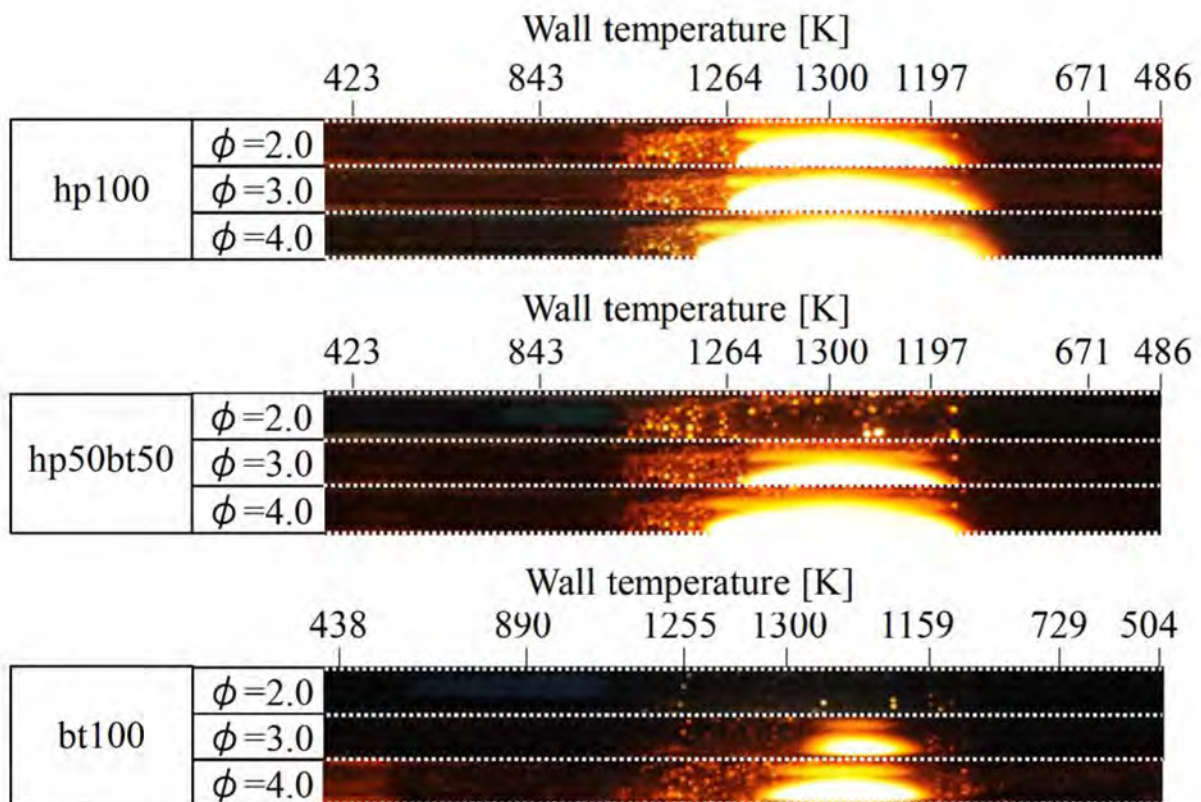
Fig. 2.5.1 Equivalence ratio dependence: Direct images of flames and soot responses for hp100, hp50bt50, and bt100 at $T_{w,max} = 1,300$ K and $U_0 = 10$ cm/s.

2-5-2 Effect of butanol addition on the sooting region length

If the same images are fixed at the same equivalence ratio, starting at hp100, hp50bt50, and bt100, the effect of the addition of butanol on sooting behavior will become evident. Figure 2.5.2 shows the effect of the addition of butanol on soot formation at an equivalence ratio of 2.0, 3.0, and 4.0. All of the equivalence ratios show the sooting region length being inversely proportional with butanol mole percentages. The decreasing sooting region length is also indicative of the decrease of the rate of aromatic formation. Hence, the sooting tendency of *n*-heptane is inverserly proportionaly to the, amount of butanol.
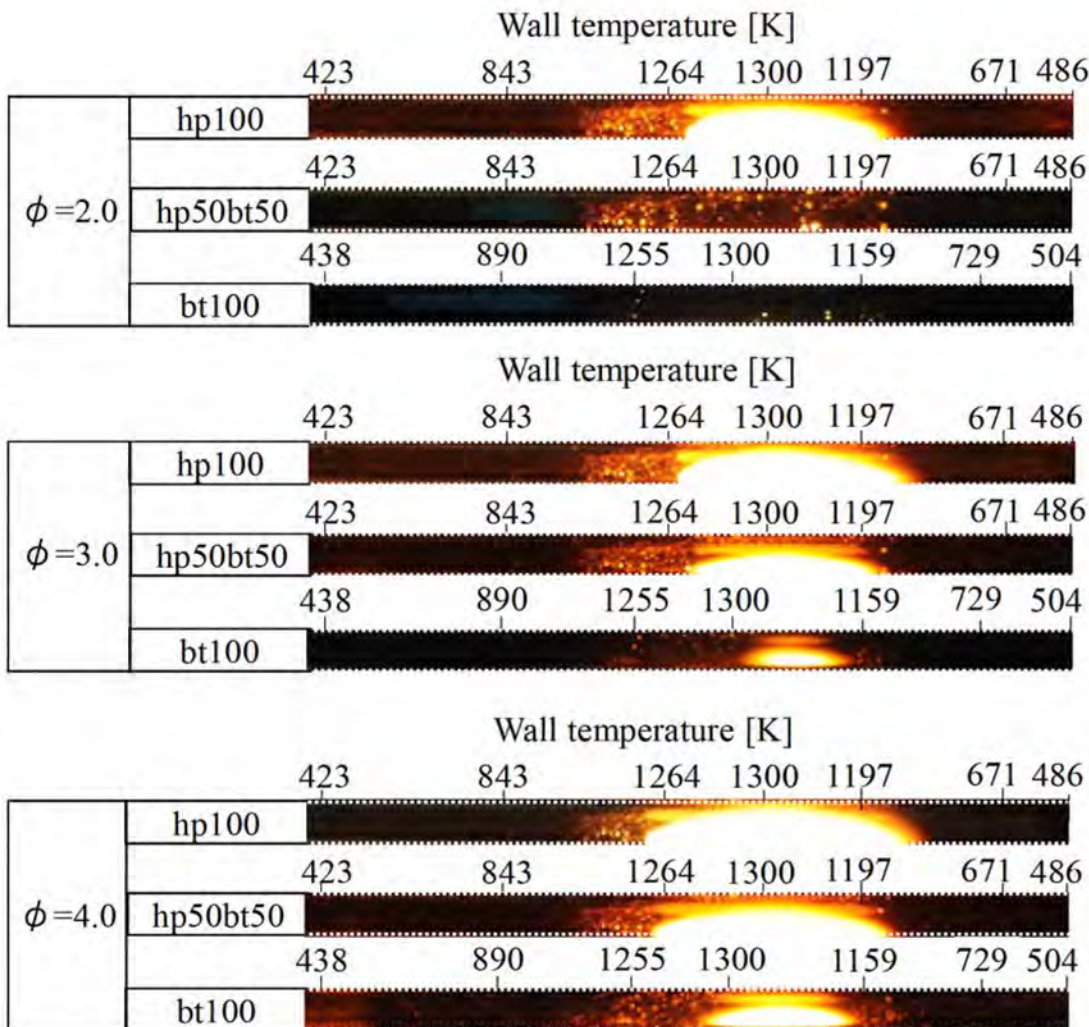
Fig. 2.5.2 Effect of butanol addition: Direct images of flames and soot responses for hp100, hp50bt50, and bt100 at $T_{w,max}$ = 1,300 K and U_0 = 10 cm/s.

2-6 Flame position

The mechanisms were validated by comparing the computed flame positions to its experimental counterparts. The experimental flame position is defined as the peak position in the luminosity profile, while the computational one is defined as the peak position in the heat release rate (HRR) profile. Figures 2.6.1, 2.6.2, and 2.6.3 show the representatives of hp100, hp50bt50, and bt100 of the luminosity profile of the CH filtered images and the HRR profiles computed with the Wang and CRECK mechanisms at the highest equivalence ratio of $\phi = 4.0$, $T_{w,max} = 1,300$ K, and $U_0 = 10$ cm/s. Since the flame has a weak luminosity, the location of the flame is shown using white circle lines. Furthermore, the fuels show a small single peak for flame position and large abroad peak for the luminosity of soot formation.

The value of axial flame positions (x) and wall temperature at flame positions ($T_{w,f}$) in the experiments and computations at similar conditions as the ones shown in Tables 2.6.1, 2.6.2, and 2.6.3.

2-6-1 hp100

As shown in Figure 2.6.1, a flame with very weak chemiluminescence is located at the far upstream side of the onset of soot formation. The flame position can be determined using the CRECK mechanism ($x = 4.07$ cm and $T_{w,f} = 1,151$ K), and it is in agreement with the experimental flame position ($x = 4.05$ cm and $T_{w,f} = 1,147$ K). There is a small discrepancy in its wall temperature, at ~0.3 %. The flame position computed with the Wang mechanism ($x = 3.76$ cm and $T_{w,f} = 1,017$ K) reported a much lower temperature region relative to the experimental flame position, and its wall temperature discrepancy is quite significant, at ~11 %.

Fig. 2.6.1 Comparison between experimental of peak luminosity profile with computational HRR profile (Wang and CRECK mechanisms) for hp100 at $\phi = 4.0$, $T_{w,max} = 1,300$ K, and $U_0 = 10$ cm/s.

Table 2.6.1 shows the comparison between the axial flame position and wall temperature at multiple flame positions via experiment and computational approaches at parameters of hp100 at $\phi = 4.0$, $T_{w,max} = 1,300$ K, and $U_0 = 10$ cm/s.

Fuel: hp100	Axial flame position, x, [cm]	Wall temperature, $T_{w,f}$ [K]	Percentage wall temperature different [%]
Experiment	4.05	1147	
Wang mechanism	3.76	1017	11
CRECK mechanism	4.07	1151	0.3

2-6-2 hp50bt50

Experimental CH filtered images and computed HRR for hp50bt50 at an equivalence

ratio of 4.0 and $U_0 = 10$ cm/s is shown in Fig. 2.6.2. Current mechanisms (Wang and CRECK mechanisms) predicted the flames position of hp50bt50 at similar conditions as those reported in Fig. 2.6.1. The computational values for the axial positions of the flame position and wall temperature at the flame position is tabulated in Table 2.6.2. There are variations among the mechanism in the case of flame position prediction. Wang mechanism report an axial flame position at 3.81 cm at wall temperature of 1,038 K, which is a 7 % difference with that of the experimental flame position. However, the CRECK mechanism shows a closer prediction to the experimental flame position, where it reports an axial flame position of 4.06 cm and a wall temperature of 1,149 K, which is only a 3 % difference with that of the experimental value of the flame position.
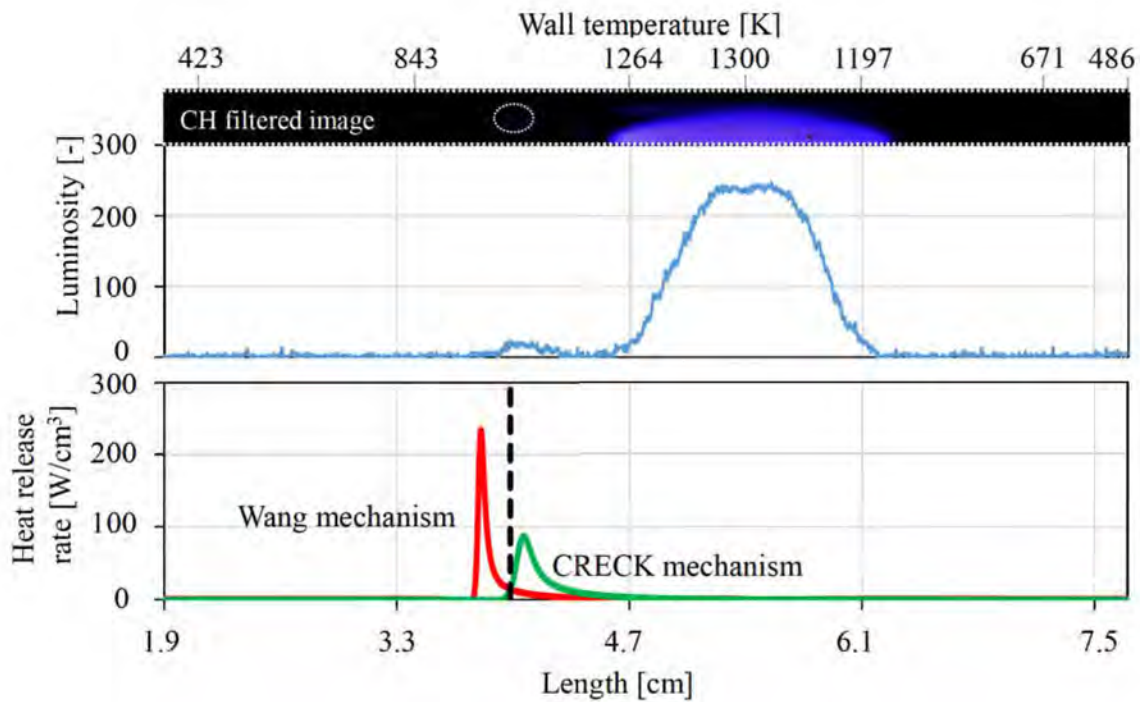
Fig. 2.6.2 Comparison between experimental of peak luminosity profile with computational HRR profile (Wang and CRECK mechanisms) for hp50bt50 at $\phi = 4.0$, $T_{w,max} = 1,300$ K, and $U_0 = 10$ cm/s.

Table 2.6.2 show the comparison between axial flame position and wall temperature at the flames position via experiment and computational approaches in the case of hp50bt50 at ϕ = 4.0, $T_{w,max}$ = 1,300 K, and U_0 = 10 cm/s.

Fuel: hp50bt50	Axial flame position, x, [cm]	Wall temperature, $T_{w,f}$ [K]	Percentage wall temperature different [%]
Experiment	3.98	1119	
Wang mechanism	3.81	1038	7
CRECK mechanism	4.06	1149	3

2-6-3 bt100

Same as hp100 and hp50bt50, flame position in the experiments for bt100 also was defined as maximum luminosity from the flame while in the computations was defined as peak position of net heat release rate. Experimental CH filtered image with temperature profile, luminosity profile and computational HRR profile (Wang and CRECK mechanisms) for bt100 at ϕ = 4.0, and U_0 = 10 cm/s are presented in Fig. 2.6.3. A small single luminous region represents flame position and large peak for the luminosity of soot formation are observed.

Axial flame position, wall temperature and percentage wall temperature difference for bt100 are presented in Table 2.6.3. Existing Wang and CRECK mechanisms predict the flame position of bt100 satisfactory. It can be seen in Table 2.6.3 that the Wang mechanism reported a small discrepancy, at 0.1 % (x = 3.87 cm, $T_{w,f}$ = 1,107 K). However, the CRECK mechanism still reports a reasonable percentage discrepancy, which is lower than 3 % relative to that of the experimental value(s).
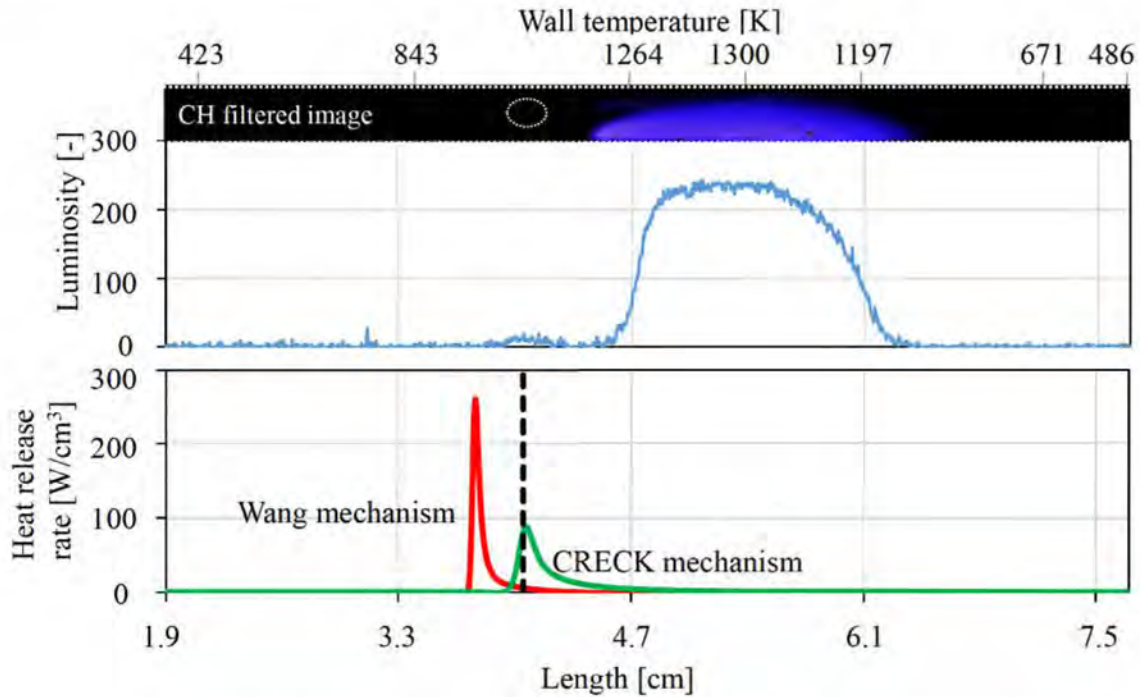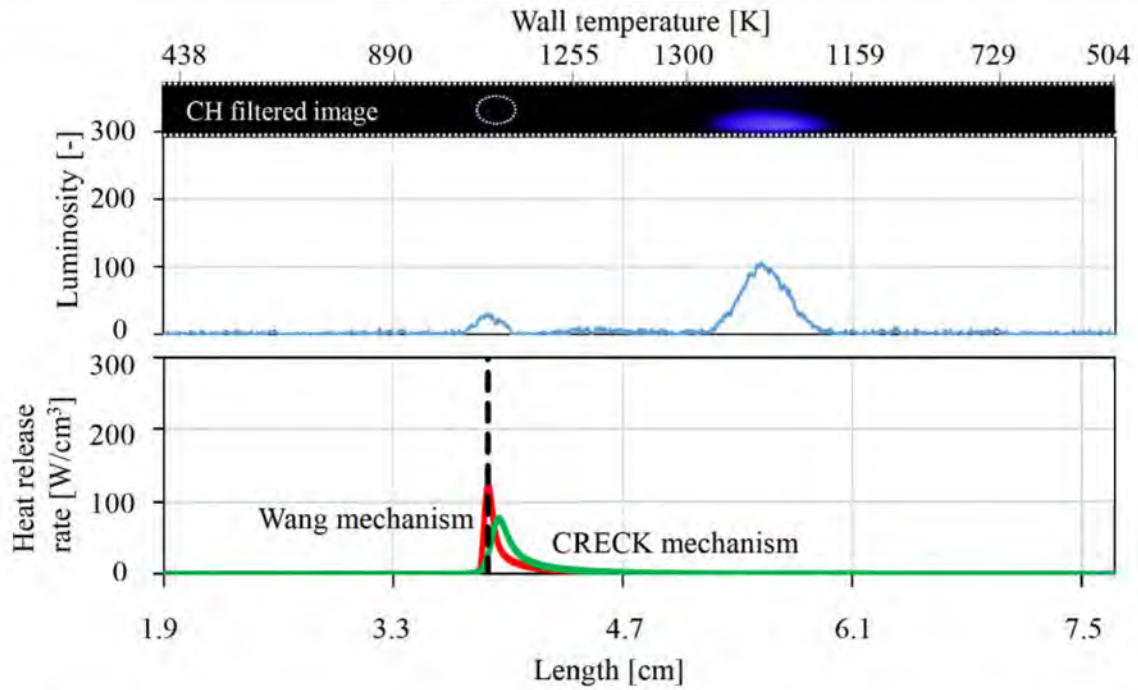
Fig. 2.6.3 Comparison between experimental of peak luminosity profile with computational HRR profile (Wang and CRECK mechanisms) for bt100 at ϕ = 4.0, $T_{w,max}$ = 1,300 K, and U_0 = 10 cm/s.

Table 2.6.3 shows the comparison between axial flame position and wall temperature at flame position via experiment and computational approaches for bt100 at ϕ = 4.0, $T_{w,max}$ = 1,300 K, and U_0 = 10 cm/s.

Fuel: bt100	Axial flame position, x, [cm]	Wall temperature, $T_{w,f}$ [K]	Percentage wall temperature different [%]
Experiment	3.88	1109	
Wang mechanism	3.87	1107	0.1
CRECK mechanism	3.94	1133	2.2

2-6-4 Overall flame position

Figure 2.6.4 presents the overall flame position between the experiments and

(a) ϕ = 2.0

(b) ϕ = 3.0

(c) ϕ = 4.0
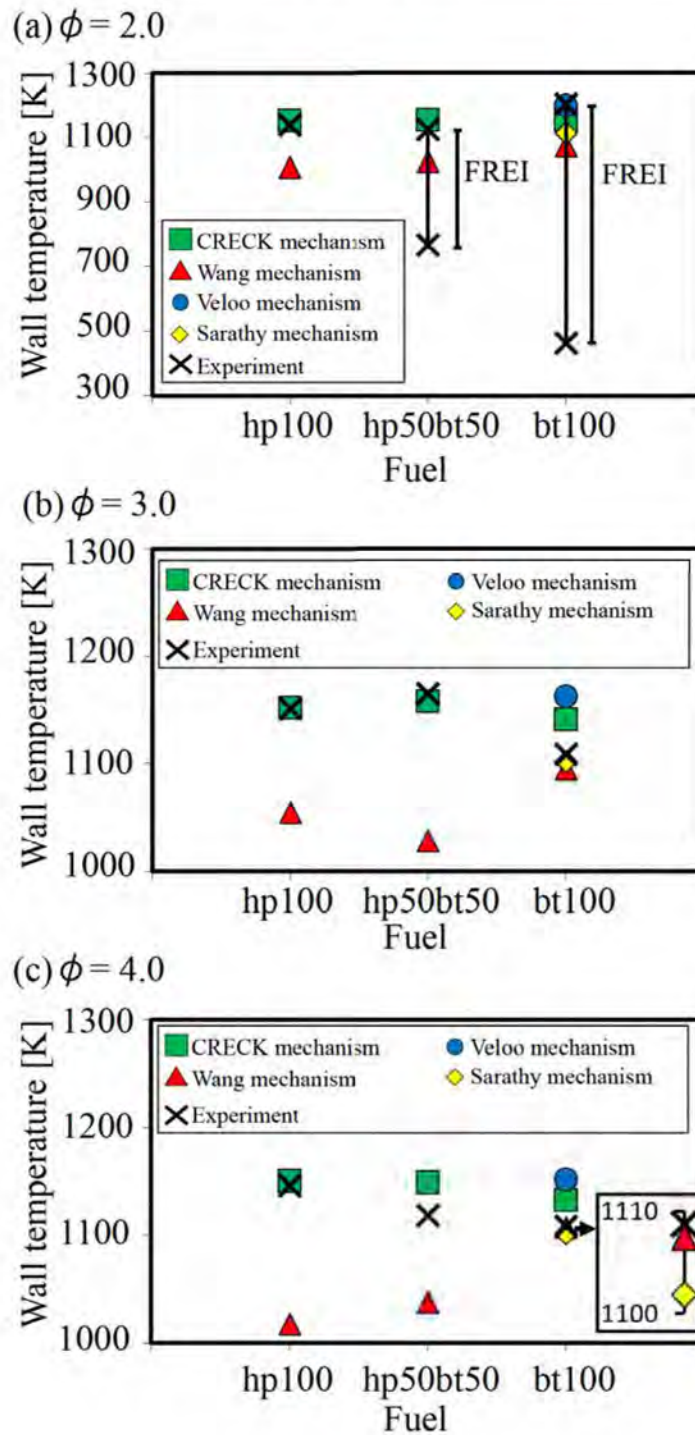
Fig. 2.6.4 Experimental and computational flame positions for hp100, hp50bt50 and bt100 at ϕ = 2.0, 3.0 and 4.0 at $T_{w,max}$ = 1,300 K and U_0 = 10 cm/s.

computations at equivalence ratios of 2.0, 3.0, and 4.0 in the case of all of the employed fuels. At ϕ = 2.0, Flames with Repetitive Extinction and Ignition (FREI) [76] was observed for

hp50bt50 and bt100, while stable flame was observed only in the case of hp100. Nonetheless, the CRECK mechanism are in excellent agreement with the flame position of hp100 relative to the ones reported by the Wang mechanism. At $\phi = 3.0$, the experimental flame position expressed by the wall temperature slightly increased, from hp100 to hp50bt50, then decreases from hp50bt50 to bt100. The CRECK mechanism predicts this trend well, although a small discrepancy is apparent in the case of bt100. The flame positions expressed by the wall temperature computed using the Wang mechanism are much lower than that of the experiments involving hp100 and hp50bt50, while the computed values obtained using the Wang mechanism reported excellent agreements with the experimental values in the case of bt100. The Veloo mechanism overestimates the experimental flame position in the case of bt100, however, computations using the Sarathy mechanism resulted in the best agreement with that of experimental values among the employed mechanisms. At $\phi = 4.0$, the experimental flame position expressed by the wall temperature is inversely proportional to the amounts of *n*-butanol in mixed fuels. The CRECK mechanism predicted this experimental trend well, while the Wang mechanism reported an inverse tendency relative to the experimental values. Although the Wang mechanism significantly underestimates the flame positions for hp100 and hp50bt50, it reported the best agreement with the experimentally obtained values in the case of bt100.

From the overall flame position results, it can be concluded that the CRECK mechanism reported values that are in better agreement with experimental values relative to that of the Wang mechanism.

2-7 Summary

The effects of the addition of *n*-butanol on sooting tendency and formation of initial stages of primary intermediates for rich *n*-heptane/air mixtures were studied using the MFR. The sooting tendency was experimentally investigated over equivalence ratios of 1.5 - 4.0 at a maximum wall temperature of 1,300 K.

In the critical equivalence ratio experiment, the results showed two types of flame and soot responses, consisting of "flame" and "flame + soot". The latter is directly proportional to the amount of butanol added to the fuel. Hp100 started showing a critical equivalence ratio at 2.0 and hp50bt50 at 2.2, while bt100 shows this at 2.6. This confirms the effect of butanol as an oxygenated fuel at higher critical equivalence ratios, which results in lower sooting tendency. The sooting tendency was also qualitatively investigated via the length of the sooting region. The extension of the sooting region is directly proportional with the equivalence ratio and inversely proportional with the amount of *n*-butanol in the fuel.

The validity of the present mechanisms were tested by comparing the maximum HRR in the computational results with that of the experimental peak position in the luminosity profile of the flames position. The CRECK mechanism are in excellent agreement with the experimental flames position.

Appendix 2-A Contribution of heat release rate for the CRECK and Wang mechanisms

Figures 2.A.1 and 2.A.2 show the contribution of the heat release rate to the peak value of the CRECK and Wang mechanisms at T_{max}=1,300 K. The reaction(s) significantly contributed to the CRECK and Wang mechanisms. However, the dependence of fuel(s) on the contributions differ between the CRECK and Wang mechanisms.
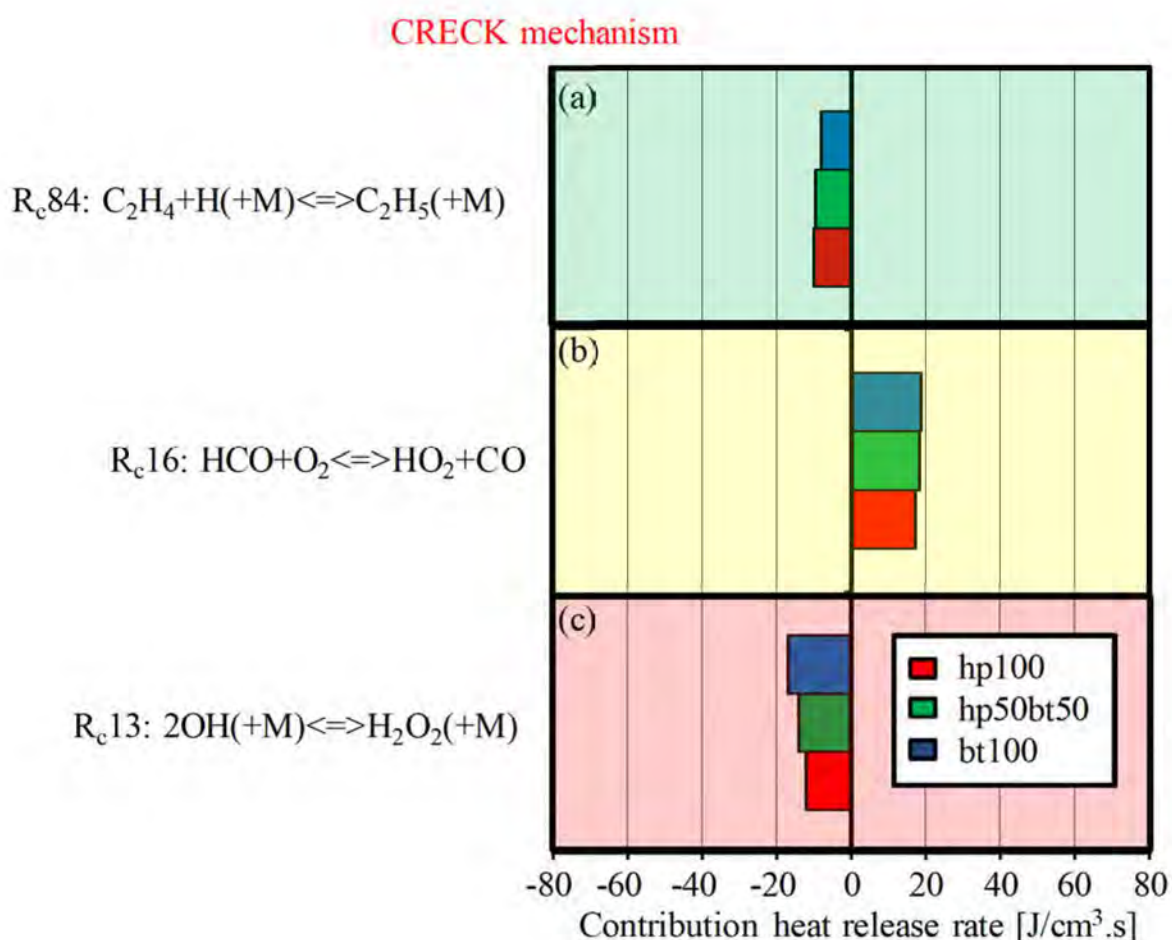
Figure 2.A.1 Contribution of heat release rate to its peak value for the CRECK mechanism at $T_{w,max}$=1,300 K. (R_C: CRECK reaction)

For example, the contribution from $C_2H_4+H(+M)<=>C_2H_5(+M)$ decreases with the addition of butanol in the CRECK mechanism, but it lacks a monotonic variation in the Wang

mechanism; the contributions from $HCO+O_2<=>HO_2+CO$ and $2OH(+M)<=>H_2O_2(+M)$ increased with the addition of butanol in the CRECK mechanism, but decreased in the Wang mechanism. Due to the large contribution from $HCO+O_2<=>HO_2+CO$ at bt50hp50 and hp100 in the Wang mechanism, it could predict the flame positions at much lower temperatures relative to the experiments in the aforementioned fuel conditions.
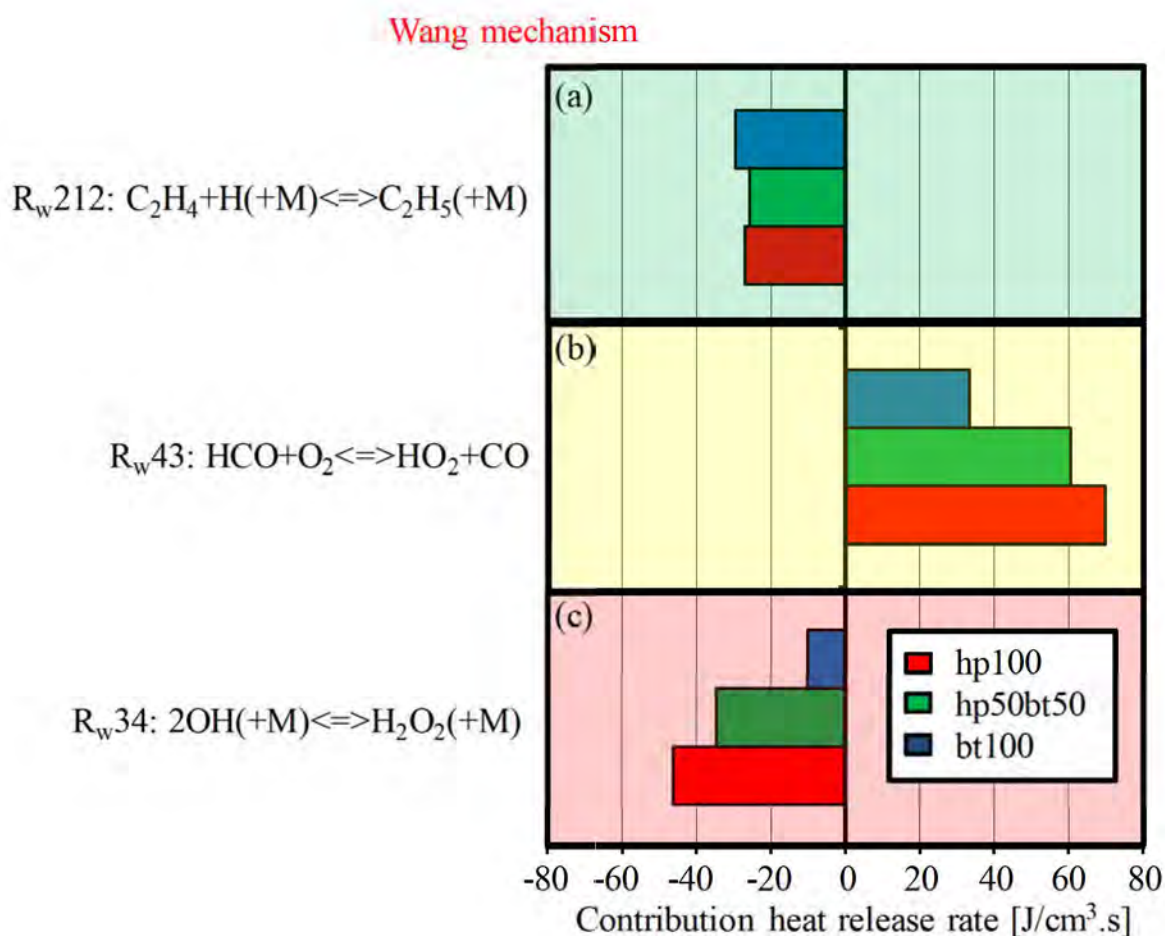
Figure 2.A.2 Contribution of heat release rate to its peak value for the Wang mechanism at $T_{w,max}=1,300$ K. (R_w: Wang reaction)

Chapter 3

Validation of existing mechanism using MFR

3-1 Introduction

The previous chapter discussed the effect of the addition of butanol on the sooting behavior(s) of n-heptane flames. It was concluded that butanol is capable of extending the critical equivalence ratio, which lower sooting tendencies. The discussion continues with the species measurement produced from the n-heptane/n-butanol mixture flames. The measurement species are divided into two parts: (1) Small hydrocarbons of C_1 and C_2 species, and (2) larger hydrocarbons and PAHs. Both were tested under similar parameters, such as an inlet mean velocity, $U_0 = 10$ cm/s, pressure, $P = 1$ atm, and a maximum wall temperature, $T_{w,max} = 1,100$ K.

The measurement of small hydrocarbons species C_1 and C_2 were done using a Gas Chromatography-Thermal Conductivity Detector (GC-TCD). Six species profiles were identified by GC-TCD, which were ethylene (C_2H_4), acetylene (C_2H_2), ethane (C_2H_6), methane (CH_4), carbon monoxide (CO), and carbon dioxide (CO_2).

The measurement of larger hydrocarbons and PAHs were done using a Gas Chromatography/mass spectrometry (GC/MS). Seven gases were measured; benzene (C_6H_6), phenol (C_6H_5OH), benzaldehyde (C_7H_6O), toluene (C_7H_8), ethylbenzene (C_8H_{10}), styrene (C_8H_8), and naphthalene ($C_{10}H_8$).

The concentration for the measured species in the case of each fuels were plotted against the equivalence ratios. The capability of several mechanisms were also compared with the measured species by plotting them on the same axis.

Species measurement results are essential towards understanding the effect of butanol as an oxygenated fuel on the products of small and larger hydrocarbons, as well as PAHs. These products are well known and widely accepted by researchers as key intermediate species or soot precursors that form larger soots [129–131]. Therefore, discussions regarding the effect of the addition of butanol to soot precursors (C_2H_2 and C_2H_4), PAHs (C_6H_6, C_8H_{10}, C_8H_8 and $C_{10}H_8$), as well as CO and CO_2 was conducted. This study intends to provide useful insights into the soot formation process.

3-2 Experimental method for species measurement

The experimental method for species measurement used in this work is similar to the ones outlined in the previous chapter (Section 2.2.1). The objective detailed in the previous chapter is to investigate flame and soot responses of *n*-heptane/*n*-butanol mixtures, while in this chapter, the objective is to measure the species of *n*-heptane/*n*-butanol mixture flames. Therefore, the MFR was used alongside with a gas sampler and GC-TCD or GC/MS. The schematic diagram of the MFR with a species measurement method and temperature profile are shown in Fig. 3.2.1.
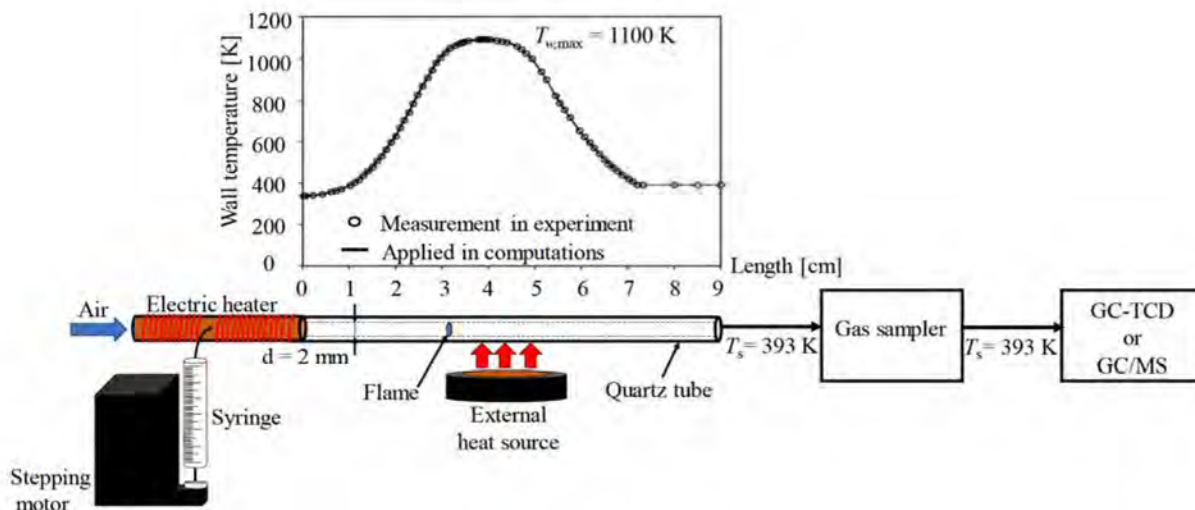
Fig. 3.2.1 Schematic diagram of the MFR connected to a gas sampler and GC-TCD or GC/MS.

The quartz tube was used as a reactor and the exit of the quartz tube is connected to the gas sampler (see Fig. 3.2.2(a)), which can be used to obtain the constant sampler loop volume. In this study, a sampler loop volume of 250 μL was set up. After the gas sampler, the GC-TCD or GC/MS method was used to identify and measure the obtained species. Two sampling lines were used to flow the gas from the MFR to GC-TCD or GC/MS. The first sampling line was connected between the MFR and gas sampler while the second sampling line was connected between the gas sampler and GC-TCD or GC/MS. The sampling line was stainless tube of 1 mm that attached with thermocouple and cord type resistance heaters. An insulation tape also

was used to cover whole parts of sampling line in order to maintain a fixed temperature. Both sampling line temperature were kept at 120 ˚C to prevent condensation from interrupting the measurements.
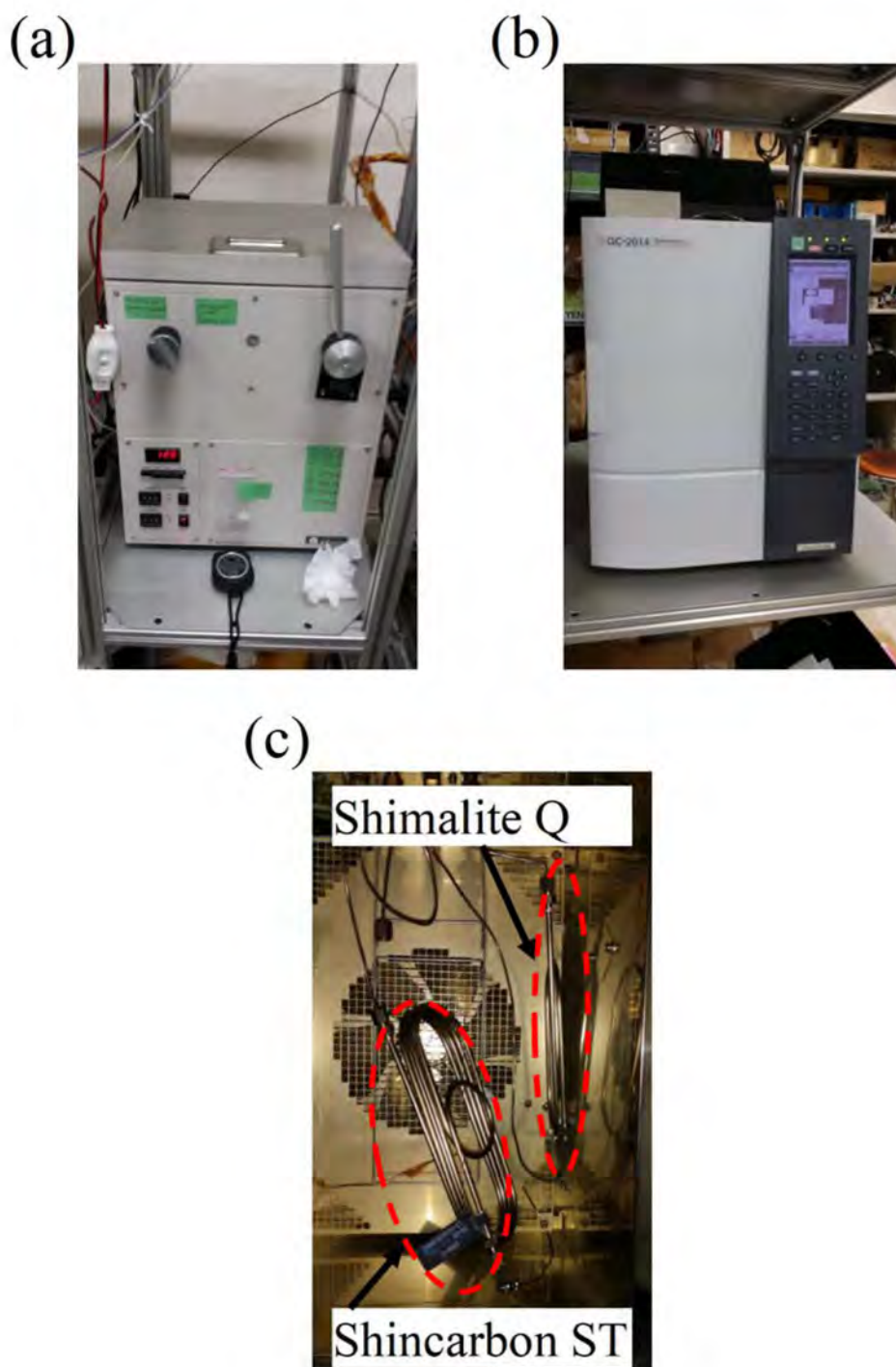
Fig. 3.2.2 (a) Gas sampler (b) GC-TCD (c) Column of Shimalite Q and Shincarbon ST.

As pointed out previously, the species measurement method is made up of two parts. The first part is to measure small hydrocarbons species C_1 and C_2, conducted using the GC-TCD (see Fig. 3.2.2(b)). GC TCD separates a different components gas mixture and identifies the components. The GC consists of a stationary phase (column), a flowing mobile phase (carrier gas) and detector. In these experiments, a 2.0 m long Shincarbon ST was used as a sampler column, while a 0.5 m long Shimalite Q was used as a reference column (see Fig. 3.2.2(c)). The column temperature for GC-TCD was set to 150 °C, while the TCD temperature was set to 210 °C . Helium (He) was used as the carrier gas, at a flow rate of 50 ml/min. Six initial-stage primary intermediates species (C_2H_4, C_2H_2, C_2H_6, CH_4, CO, and CO_2) were detected and quantified via calibration with standard gases.

The second part measures larger hydrocarbons and PAHs conducted using a GC/MS (see Fig. 3.2.3(a)). GC/MS was used instead of GC-TCD was due to the current GC-TCD column unable to measure higher carbon species than the C_2 species.
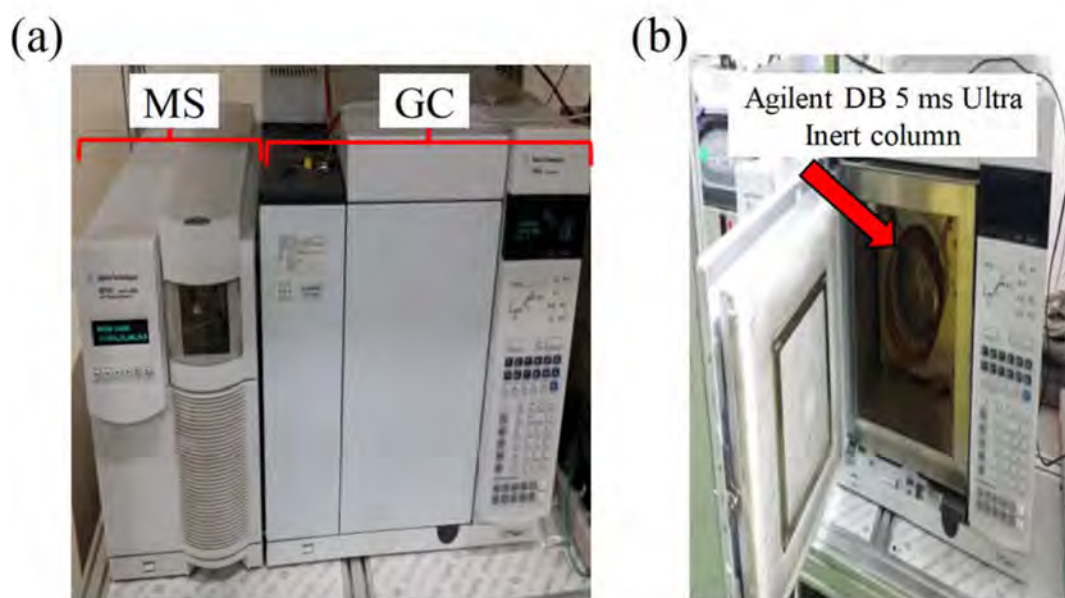
Fig. 3.2.3 (a) GC/MS (b) Agilent DB-5 ms Ultra Inert column.

GC/MS consists of two important parts which are GC and MS. The GC uses capillary

column which depend on the column's length, diameter and thickness. The column used for currect study was Agilent DB-5 ms Ultra Inert column that is 60 m long, has an inner diameter of 250 μm, and a film thickness of 0.25 μm (see Fig. 3.2.3(b)). The temperature of the column for GC/MS was set to 55 °C for 10 minutes, then increased to 200 °C at 20 °C /min for 2 minutes, as shown in Fig. 3.2.4. The column separated the sampled gas into several compounds before entering MS.

MS produces mass spectrum to identify and measure sampled gas. In the GC/MS experiment also, helium as carrier gas was used to move sampled gas from GC to MS through column. Seven sampled gases were measured in this study, which were C_6H_6, C_6H_5OH, C_7H_6O, C_7H_8, C_8H_{10}, C_8H_8, and $C_{10}H_8$.
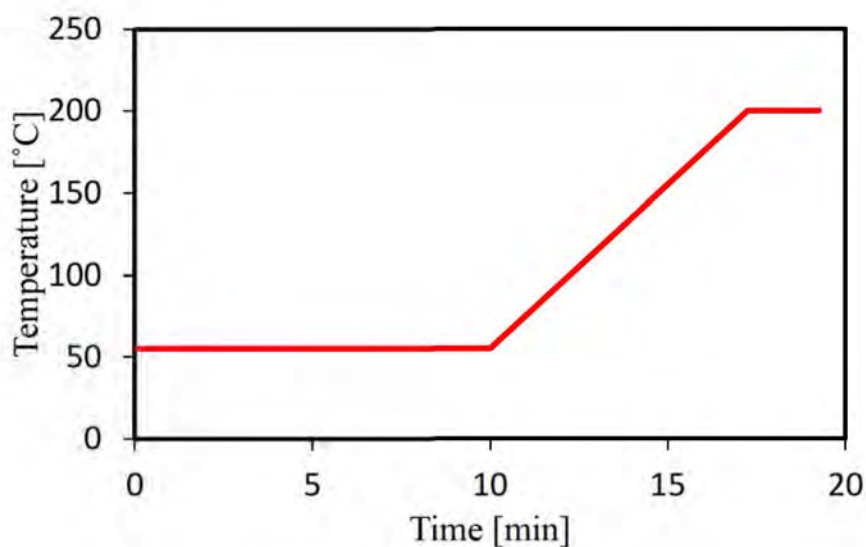
Fig. 3.2.4 Temperature profile for GC/MS.

The concentration of benzene was determined using a standard calibration gas of 965 ppm, 99.7 ppm, and 9.65 ppm, while the concentration of other species were calculated using a relative response factor. In this study, the relative response factor calculated in [129] was used. They proposed an equation that can be used to measure the total ionization cross section:

$$I_t = QI_e dN$$

56

where I_t represents the total ion current, Q represents the total ionization cross section, I_e denotes the ionizing electron current, d denotes the ionizing path length, and N denotes the molecules' concentration. It was reported in Fitch et al. [132] that the prediction of relative total ionization cross section method accuracy is within 4.69 %. In order to calculate Q, the number of carbons, hydrogens, and oxygens are essential. Thus, the following equation is used.

$$Q = 0.082 + a_C n_C + a_H n_H + a_O n_O$$

where a_C, a_H, and a_c are the coefficients of carbon, hydrogen, and oxygen, at 1.43, 0.73, and 1.10, respectively, while n_C, n_H, and n_O represents the atom numbers of carbon, hydrogen, and oxygen, respectively. The information of each measured species is tabulated in Table 3.2.1.

Table 3.2.1 ·

Name of species	Molecular structure	Number of carbon atoms	Number of hydrogen atoms	Number of oxygen atoms	Total ionization cross section [eV]	Relative response factor
Benzene	C_6H_6	6	6	-	13.042	1
Phenol	C_6H_5OH	6	6	1	14.142	1.084
Benzaldehyde	C_7H_6O	7	6	1	15.572	1.194
Toluene	C_7H_8	7	8	-	15.932	1.222
Ethylbenzene	C_8H_{10}	8	10	-	18.822	1.443
Styrene	C_8H_8	8	8	-	17.362	1.331
Naphthalene	$C_{10}H_8$	10	8	-	20.222	1.551

3-3 Computational methods

The computation of the flow in the MFR is the same to the one detailed in Section 2.3. Therefore, the computational method will only be briefly described here. The computations were performed using ANSYS chemkin 17.2 with a PREMIX based code. A heat convection between the wall and inner gas flow was included in the energy equation. The parameters from the experimental method, such as temperature, pressure, equivalence ratios, and inlet mean velocity were used in the computational method.

As outlined above, one of the parameter from the experiment used in the computation is the temperature, where its profile is shown in Fig. 3.2.1. Note that the maximum wall temperature for the experimental flame and soot response was 1,300 K, as per the previous chapter. However, in the measurement species experiment, the maximum wall temperature here is 1,100 K. The maximum wall temperature in the measurement species experiment is lower than the flame and soot response experiment, since the target is not soot formation, instead, it is the gas phase of small and large hydrocarbons, as well as PAHs. Therefore, this temperature condition was set up after conducting several trial experiments to ensure that no soot is formed/present during species measurement.

To understand the formation of small and large hydrocarbons, as well as PAHs, a suitable chemical kinetic mechanism is required. Therefore, several chemical kinetic mechanisms were compared with the experimentally obtained results, where each fuel has different tested by chemical kinetic mechanism.

In the case of hp100 fuel, five mechanisms were used. The first mechanism is the CRECK mechanism, which was developed by the Chemical Reaction Engineering and Chemical Kinetics (CRECK) modeling group [124–126]. The second mechanism is the Wang mechanism, developed by the Engine Research Center, University of Wisconsin, Madison [118]. The third and fourth mechanisms are the reduced Livermore [133] and detailed Livermore

mechanisms [134,135], where both were developed by Lawrence Livermore National Laboratory. The last mechanism is the KUCRS mechanism, which was created by Professor Miyoshi from Japan [136].

In the case of the bt100 fuel, four mechanisms were used in the computations, which were the CRECK [124], Wang [118], Sarathy [123], and Veloo [128] mechanisms, while in the case of hp50bt50 fuel, only two mechanisms were used, which were the CRECK and Wang mechanisms.

3-4 Measurement of small hydrocarbons

C_2H_2 and C_2H_4 led to the growth of the aromatic species to polycyclic aromatic hydrocarbons (PAHs), as well as larger aromatic rings. The coagulation of these larger aromatic ring compounds results in the production of soot. Previous studies reported that soot formation begins from hydrocarbons such as C_2H_2, C_2H_4, and others [68,139,140].

The suitability of the reaction mechanisms with the experimental results are shown in Section 3-4-1 in the case of small hydrocarbons (C_1 and C_2 species), as well as in Section 3-4-2 in the case of larger hydrocarbons and PAHs formations. The best mechanism obtained from Section 3-4-1 will be used in Section 3-4-2, which helps determine the effect of adding butanol to n-heptane on small and large hydrocarbons, as well as PAHs. Figure 3.4.1 shows the mole fraction profile of the computed species for small hydrocarbons (C_2H_4, C_2H_2, C_2H_6, CH_4, CO, and CO_2) using the CRECK mechanism along the axial length of the quartz tube, where the dashed line represents the maximum HRR.

Note that the profile of species mole fraction from computation were taken at the end of the domain of the MFR model. It can be seen in Fig. 3.4.1 that all of the species increase with respect to the maximum HRR point before they become constant until at the exit of the tube, implying that reactions are quenched at the sampling point. Thus, there are no reactions beyond the sampling point. This confirms that the trend of species from the CRECK mechanism demonstrate reasonable behavior and species measurements at the end of the quartz tube is indeed relevant.

A similar trend was also reported by large hydrocarbons and PAHs (C_6H_6, C_6H_5OH, C_7H_6O, C_8H_{10}, C_8H_8, and $C_{10}H_8$), as shown in Fig. 3.4.2. The trend of mole fraction profiles of large hydrocarbons, and PAHs reported similar trends for all fuels and equivalence ratios. A representative result of hp100 at $U_0 = 10$ cm/s, $\phi = 2.0$, and $T_{w,max} = 1,100$ K is shown here, while the other mechanisms' profiles will be discussed in the upcoming sections.
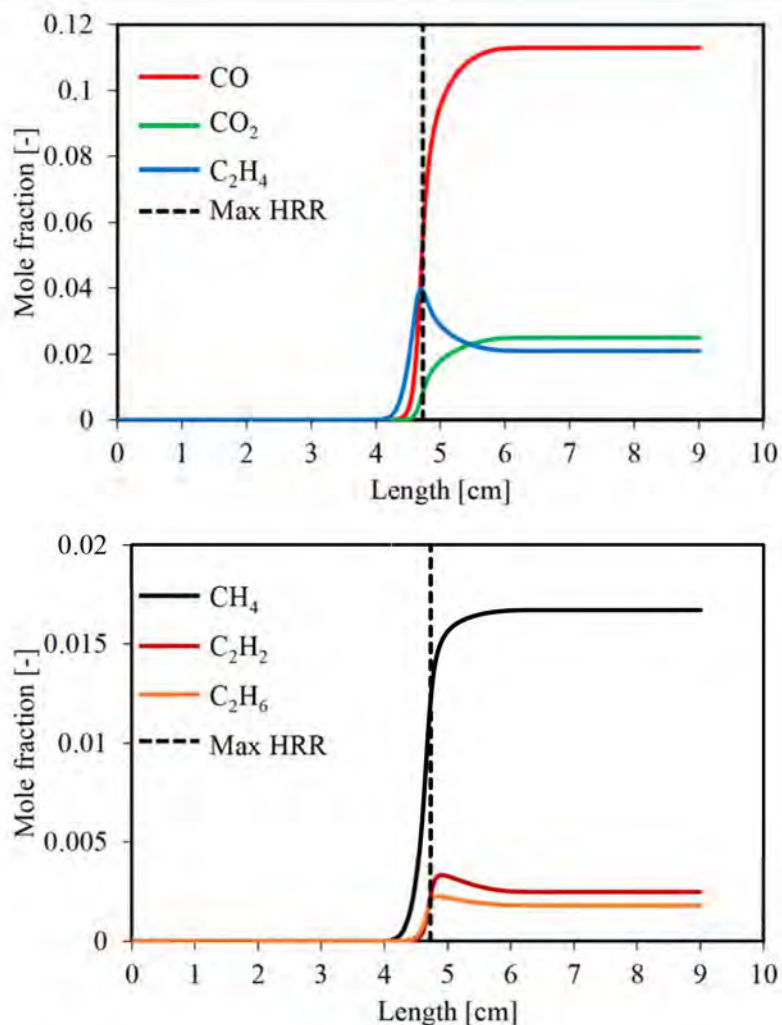
Fig. 3.4.1 Computed mole fraction profiles of small hydrocarbons species by the CRECK mechanism along the axial length of the quartz tube. (U_0 = 10 cm/s, ϕ = 2.0, and $T_{w,max}$ = 1100 K).

At this point, it is important to note that profile of species mole fraction (small and large hydrocarbons, as well as PAHs) along the axial length of the quartz tube was not measured. Measurement and comparison between experimental results (measurement species) and computational results were conducted at the sampling point which was at the exit of the quartz tube. This means, species measurement measures results of complete reactions of measured species that covers overall production and consumption in the micro flow reactor.
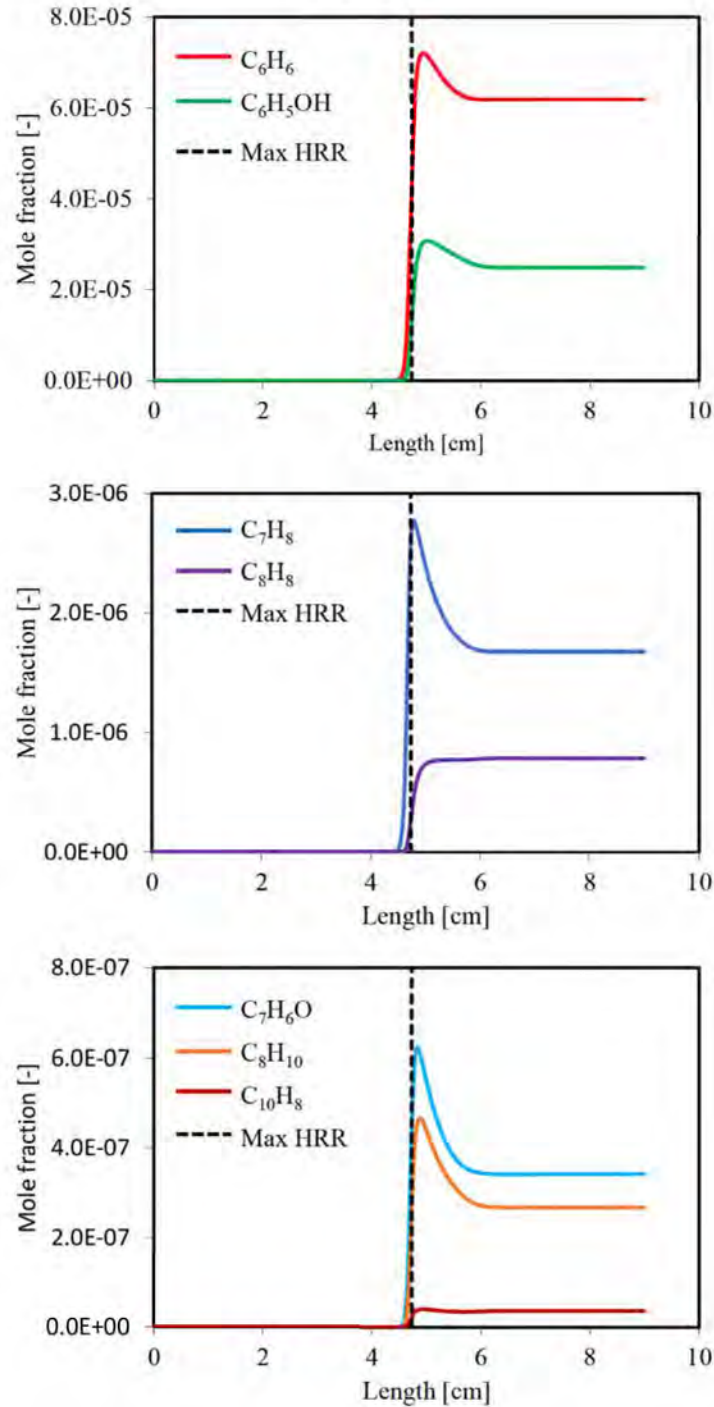
Fig. 3.4.2 Computed mole fraction profiles of large hydrocarbons and PAHs measurement species along the axial length of the quartz tube. (U_0 = 10 cm/s, ϕ = 2.0, and $T_{w,max}$ = 1100 K).

3-4-1 Formation of small hydrocarbons (C_1 and C_2 species)

This section details the measurement of species C_2H_4, C_2H_2, C_2H_6, CH_4, CO, and CO_2, representing the overall primary reactions from the pyrolysis of hp100, hp50bt50, and bt100.

The concentration of these species derived from the computation was plotted alongside the measurements at multiple equivalence ratios, as shown in Fig. 3.4.3.

In general, some of the species concentration are directly proportional to the equivalence ratios, which are demonstrated by C_2H_4, C_2H_2, C_2H_6, and CH_4. CO shows different trend in certain fuel. For hp100, CO concentration increases with respect to equivalence ratio and then shows slightly decrease. On the other hand, for hp50bt50 and bt100, the CO concentration increases with the increase of equivalence ratios and finally it shows constant concentration. Final product which is CO_2 concentration shows inversely proportional relation with respect to the equivalence ratios. Figure 3.4.3 shows the first group behavior of C_2H_4, C_2H_2, C_2H_6, CH_4, and CO. In the case of hp100, the KUCRS and reduced Livermore mechanism underpredicted the measurement of C_2H_4, especially at equivalence ratios of 3.0, 4.0, and 5.0. However, Wang, CRECK, and detailed Livermore mechanisms reported fair agreements with the measurement results. The capability of Wang and CRECK mechanisms for hp50bt50 were tested, and the results reported reasonably excellent predictions. In the case of bt100, the Sarathy, CRECK, and Veloo mechanisms reported similar trends to that of the measurement results, where it is directly proportional to the equivalence ratios.

In the case C_2H_2, most of the mechanisms under-predicted the experimental concentration values, but in the case of bt100, the Veloo mechanism reported an over-prediction of the measurement results relative to the computational results. All of the computations reported a similar trend with the measurement results of C_2H_6, but most over-predicted the measurement results, especially at higher equivalence ratios for the reduced Livermore as well as Wang mechanisms in the case of hp100. It is also evident that at the equivalence ratio of 2.0 in the case of bt100, C_2H_6 cannot be detected due to the C_2H_6 signal being too weak. In the case of the CH_4 mole fraction, the measurement results confirmed that it is directly proportional to the equivalence ratios. This trend is similar in all of the mechanisms used in this work.
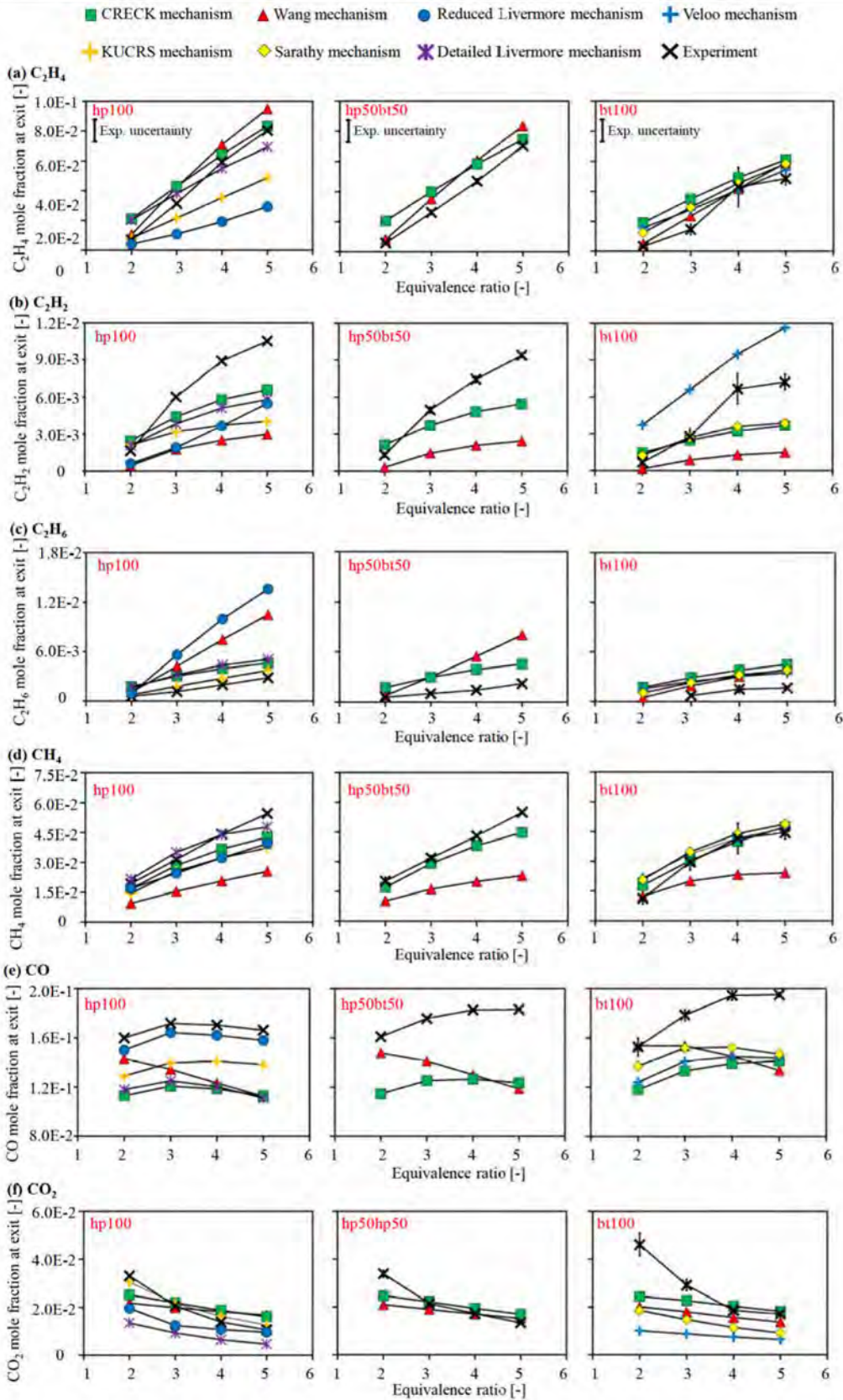
Fig. 3.4.3 Computational and experimental results of C_1 and C_2 species mole fractions at $U_0 =$ 10 cm/s, $\phi = 2.0$ to 5.0, and $T_{w,max} = 1100$ K.

The computation of the CH_4 mole fraction with the detailed Livermore mechanism reported better agreement in the case of hp100, while the CRECK mechanism reported better agreement in the case of hp50bt50 and bt100 relative to other mechanisms.

The highest measurements among the species are shown in the CO mole fraction for bt100 at ϕ = 5.0, which is ~20%. However, the computations were unable to yield excellent predictions vis-a-vis the measurements, where all of the mechanisms under-predicted the experimental results. The closest mechanism with CO measurement results was reported by the Reduced Livermore mechanism in the case of hp100. Unfortunately, this mechanism is inapplicable for hp50bt50 and bt100. Also, the CO mole fraction computed by the Wang mechanism shows a completely opposite trend with the experimental results, which is directly proportional to the equivalence ratio. Generally, the computation results by the CRECK mechanism reported a similar trend to that of the measurement results in the case of all of the fuels.

As seen in Fig. 3.4.3, the second behavior shown by CO_2 is its inverse relationship with the equivalence ratios. All of the mechanisms predicted a similar trend with the measurement results in the case of all of the fuels. In the case of hp100, the KUCRS mechanism reported the best agreement with that of the experimentally obtained results. The Detailed Livermore and Reduced Livermore mechanisms underpredicted the CO_2 concentration. However, in the case of hp50bt50 and bt100, the CRECK mechanism reported better agreements with the measurements, especially at higher equivalence ratios. In these conditions, the Wang, Sarathy, and Veloo mechanisms under-predicted the measurement results. Overall, it can be concluded that, the CRECK mechanism reports a fair agreement between the mechanisms in the case of small hydrocarbon C_1 and C_2 species. The next section elucidates the application of the CRECK mechanism for the investigation of the addition of butanol on *n*-heptane for C_1 and C_2 species

at various equivalence ratios within 2.0 - 5.0.

3-4-2 The effect of butanol addition to *n*-heptane on C_2H_2 and C_2H_4 as well as CO and CO_2.

This section discusses the effect of butanol addition to *n*-heptane on C_2H_2 and C_2H_4 and CO and CO_2 Previous studies investigated the effectiveness of addition of oxygenated fuels to base fuels in reducing soot [28]. Many researchers used a detailed chemical kinetic model to anticipate processes that takes place during the reaction of hydrocarbon with oxygenated fuels. They reported that, reaction path to CO and CO_2 species were the most produced product from the reactions of oxygenated fuels instead of going to form soot precursors. Since CO and CO_2 are strongly bonded and tend to remain intact, the concentrations of soot precursors are subsequently reduced. This agrees with Esarte et al. [141], where the authors analyzed the pyrolysis of acetylene as a baseline mixed with methanol, ethanol, iso-propanol, and *n*-butanol in a flow reactor. They concluded that alcohol is capable of reducing soot concentration. The mixed fuel mostly going to form into CO and CO_2, which removes the carbon from the alcohol from soot formation pathways, subsequently leading to soot reduction. The prevention of soot formation indirectly contributes to decreased soot precursors, such as C_2H_2 and C_2H_4. However, those studies did not outline the major reactions involved in the targeted species. This work intends to elucidate the effects of the addition of butanol on the concentrations of C_2H_2, C_2H_4, CO, and CO_2.

Figure 3.4.4 shows a comparison of the experimental and computational results of C_2H_2 and C_2H_4 mole fractions at $\phi = 2.0 - 5.0$ and $T_{w,max} = 1,100$ K. The computational results of C_2H_4 show gradually improving agreement with the measurement results in tandem with increasing equivalence ratios. Its trend mirrors that of the experimentally obtained results. It is apparent that the C_2H_4 mole fraction is inversely proportional to the mole percentage of butanol, which is also the trend observed in the case of C_2H_2. The computation of C_2H_2 concentration

confirmed the accuracy of the prediction relative to the measurement results in the case of all equivalence ratios. Decreasing concentrations of C_2H_4 and C_2H_2 confirm the capability of butanol towards decreasing soot formation.
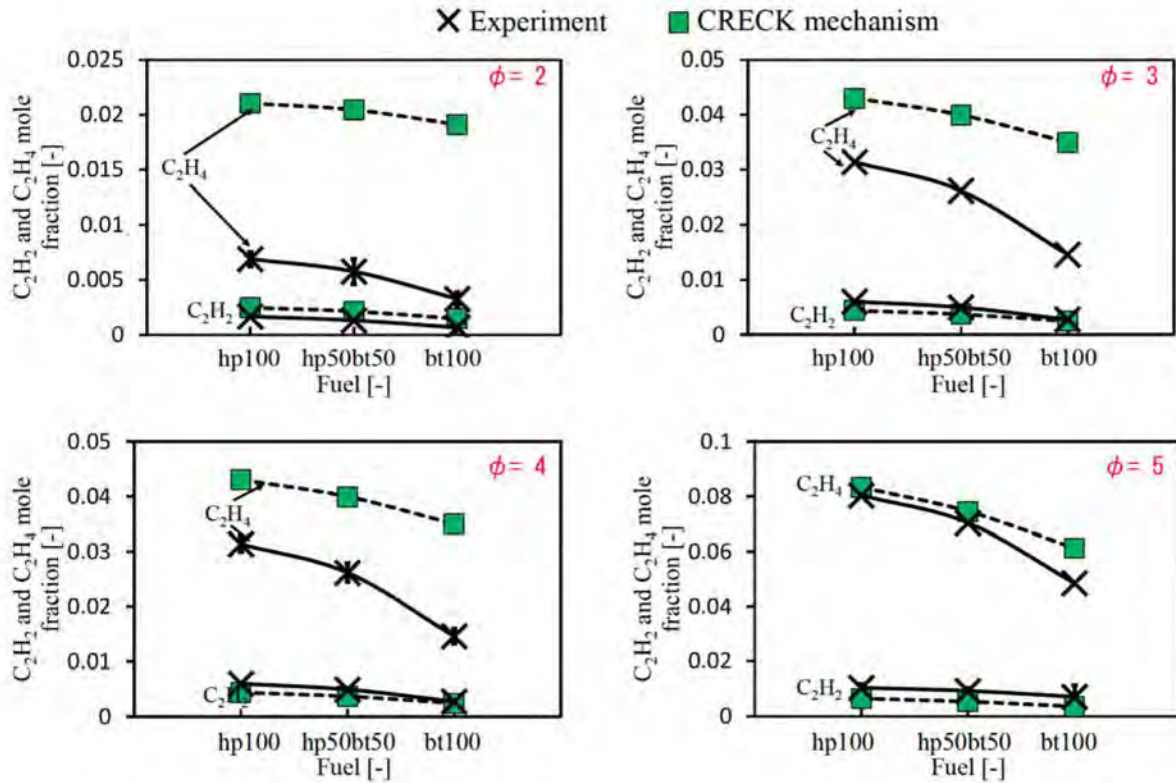
Fig. 3.4.4 Effects of butanol addition to *n*-heptane on C_2H_2 and C_2H_4 at $U_0 = 10$ cm/s and $T_{w,max}$ = 1100 K.

The effect of the addition of butanol to *n*-heptane on CO and CO_2 at $\phi = 2.0$ to 5.0 and $T_{w,max} = 1,100$ K are shown in Fig. 3.4.5. The increasing trend is evident and significant in the case of CO and CO_2 concentrations with the addition of butanol at higher equivalence ratios (3.0, 4.0, and 5.0) relative to that of the equivalence ratio of 2.0. Overall, the CRECK mechanism accurately predicted the CO_2's mole fraction. In the case of CO mole fraction, despite the trend being consistent with the measurements, the mechanism still require slight modifications.

The results shown in Figures 3.4.4 and 3.4.5 show that the mole percentage of butanol

is inversely proportional to the concentrations of C_2H_4 and C_2H_2 and directly proportional to the concentrations of CO and CO_2. This could be due to the fact that butanol as oxygenated fuels plays an important role in modifying reaction path of C_2H_2, C_2H_4, CO and CO_2 formation.

To further understand the effect of the addition of butanol to *n*-heptane on soot precursors, the behavior of larger hydrocarbons and PAHs were measured. The reaction path analysis between small and large hydrocarbons, as well as PAHs were also determined and the results are discussed in the next section.
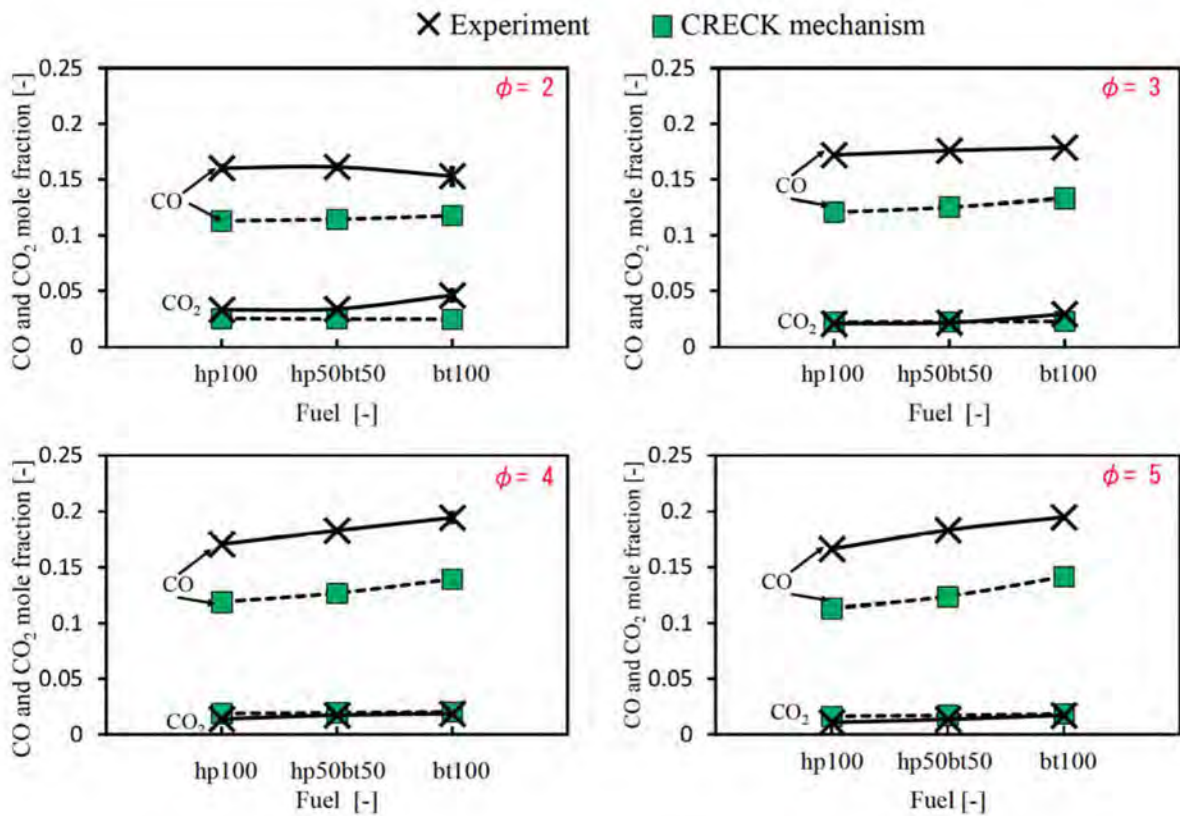

Fig. 3.4.5 Effects of butanol addition to *n*-heptane on CO and CO_2 at $U_0 = 10$ cm/s and $T_{w,max} = 1100$ K.

3-5 Measurement of Larger hydrocarbons and PAHs

Formation of C_2H_2 and C_2H_4 contribute towards the production of PAHs. From the soot formation process detailed in Section 1-4, it was pointed out that PAHs are able to combine and produce incipient soot particles. It continues to grow, aggregate, and form bigger structures, subsequently forming soot particles. Singh and Sung [142] analyzed PAHs measurement using planar laser-induced fluorescence (PLIF), and it was concluded that fuel structure influences the formation of PAHs, proving the importance of C_2H_2 in PAHs' growth process. Therefore, in the context of the second group, PAHs analysis is equally important.

3-5-1 Formation of large hydrocarbons and PAHs

The CRECK mechanism was used to investigate larger hydrocarbons and PAHs since it reported the best agreement relative to the other mechanisms. Figure 3.5.1 shows the equivalence ratio dependence on the measured and computed mole fractions by the CRECK mechanism for larger hydrocarbons and PAHs, such as C_6H_6, C_6H_5OH, C_7H_6O, C_7H_8, C_8H_{10}, C_8H_8, and $C_{10}H_8$ for all of the fuels. The measurements and computations were conducted at similar parameters as the measurements of small hydrocarbons species C_1 and C_2, as outlined in Section 3-4-1. The conditions were set at $U_0 = 10$ cm/s, $P = 1$ atm, and $T_{w,max} = 1,100$ K.

All computed species from the CRECK mechanism in the case of all of the fuels reported similar trends with that of the measurement species, where the mole fraction is directly proportional to the equivalence ratio. However, overall, most of the species mole fraction (C_6H_5OH, C_7H_6O, C_7H_8, C_8H_{10}, and C_8H_8) computed by the CRECK mechanism overestimates the measurement species, except in the case of C_6H_6 and $C_{10}H_8$.

C_6H_6 is the most important species in the case of PAHs and soot growth [137]. It reported the highest concentration relative to other species, as shown in Fig. 3.5.1, which implies C_6H_6 is a dominant species in the context of PAHs' and soot formation. This was also posited in Golea et al. [138], where C_6H_6 is the first aromatic ring that is closely related to the

soot formation process.
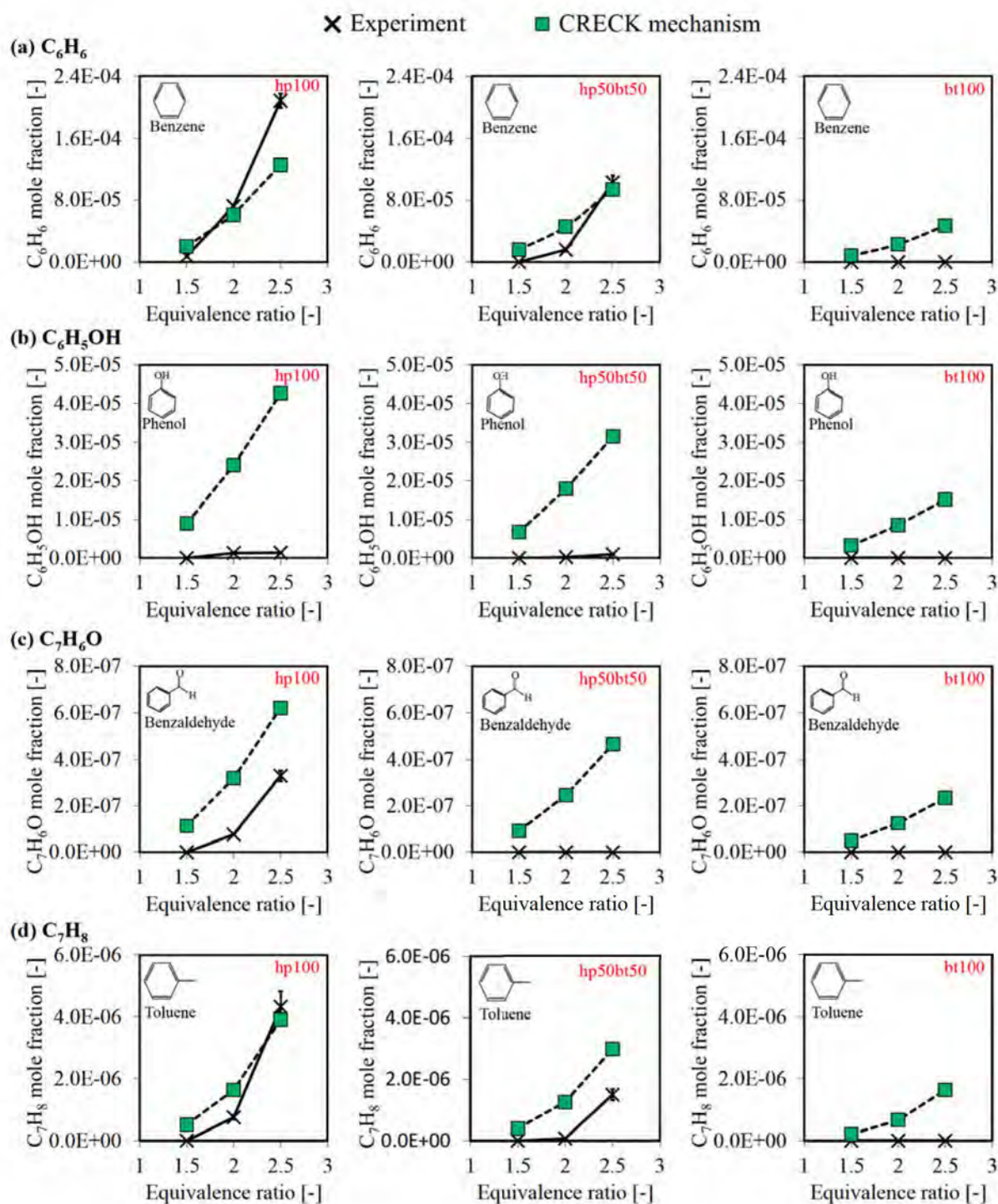
Fig. 3.5.1 Experimental and computational results of a) C_6H_6 b) C_6H_5OH c) C_7H_6O and d) C_7H_8 for hp100, hp50bt50 and bt100 at $U_0 = 10$ cm/s and $T_{w,max} = 1100$ K by the CRECK mechanism.
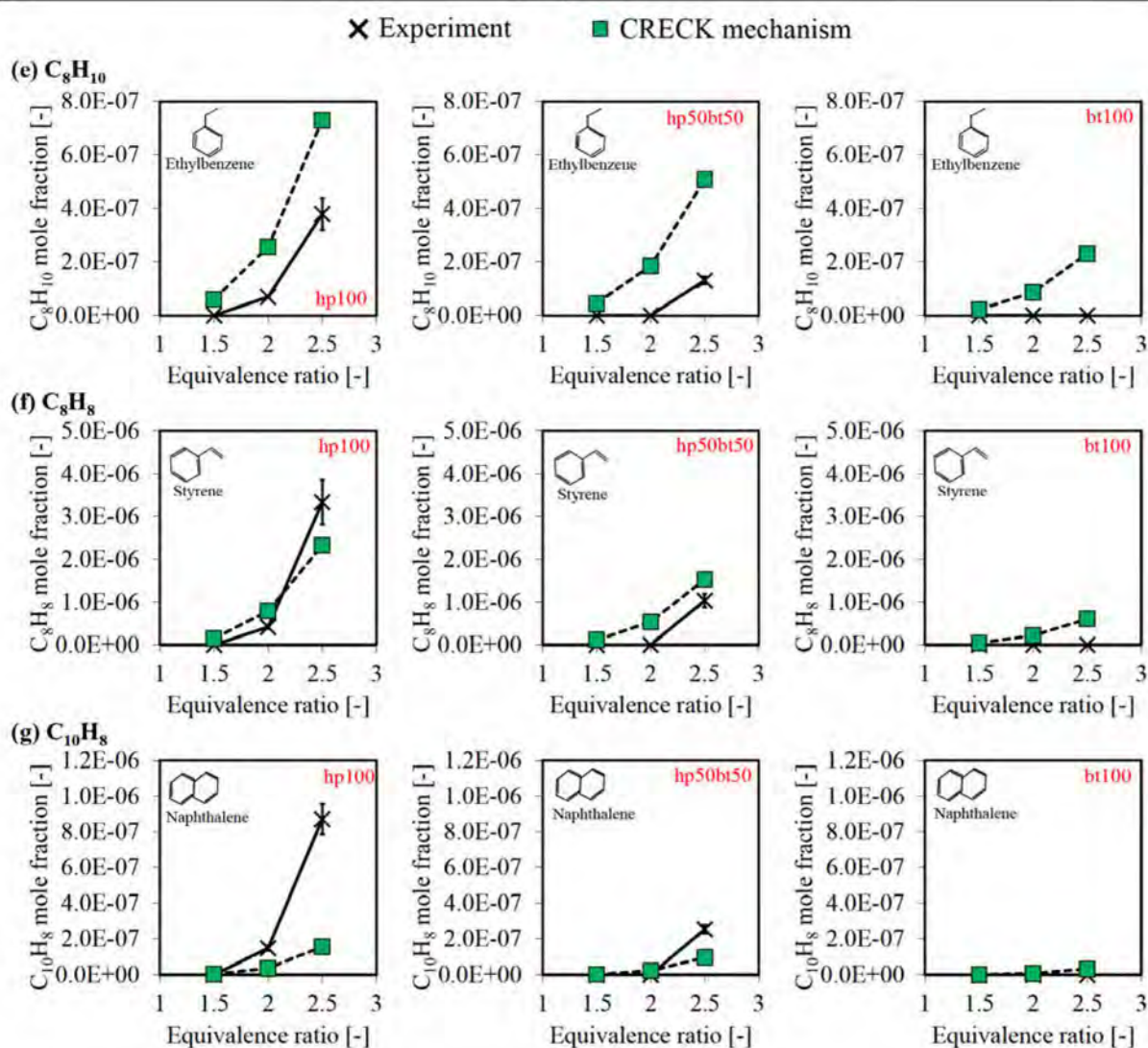
(Continued from Fig. 3.5.1) Experimental and computational results of e) C_8H_{10} f) C_8H_8 and g) $C_{10}H_8$ for hp100, hp50bt50 and bt100 at U_0 = 10 cm/s and $T_{w,max}$ = 1100 K by the CRECK mechanism.

The second aromatic ring after C_6H_6 is $C_{10}H_8$. In this study, the highest PAHs that can be measured by GC/MS is $C_{10}H_8$. Note that the mole fraction of all of the identified species for hp100 are evident, while in the case of hp50bt50, only benzene, phenol, and toluene are evident. However, in the case of bt100, none of the species are evident, since the signals were too weak. This indicates that the concentration of the measured species is inversely proportional to the butanol mole percentages, confirming the capability of butanol as oxygenated fuel towards inhibiting the formation of PAHs.

It can be surmised from Figure 3.5.1 that the CRECK mechanism remains in agreement with the measured species' C_6H_6, C_6H_5OH, C_7H_6O, C_8H_{10}, C_8H_8, and $C_{10}H_8$ mole fractions. Hence, the effect of the addition of butanol to *n*-heptane for large hydrocarbons and PAHs using the CRECK mechanism was analyzed, and the results discussed in the next subsection.

3-5-2 The effect of butanol addition to *n*-heptane on larger hydrocarbons and PAHs

This section details the investigation of the effect of the addition of butanol to *n*-heptane on larger hydrocarbons and PAHs (C_6H_6, C_7H_8, C_8H_{10}, C_8H_8, and $C_{10}H_8$) formations. $\phi = 2.0$ was selected for this purpose, due to the fact that it reports the lowest critical equivalence ratio for hp100, as per Section 2-4. Figure 3.5.2 shows effects of the addition of butanol to *n*-heptane on C_6H_6, C_7H_8, C_8H_{10}, C_8H_8, and $C_{10}H_8$ at $U_0 = 10$ cm/s and $T_{w,max} = 1,100$ K. All of the measured species mole fraction are inversely proportional to the mole fraction of butanol, which is consistent with the computation approaches reported by the CRECK mechanism.
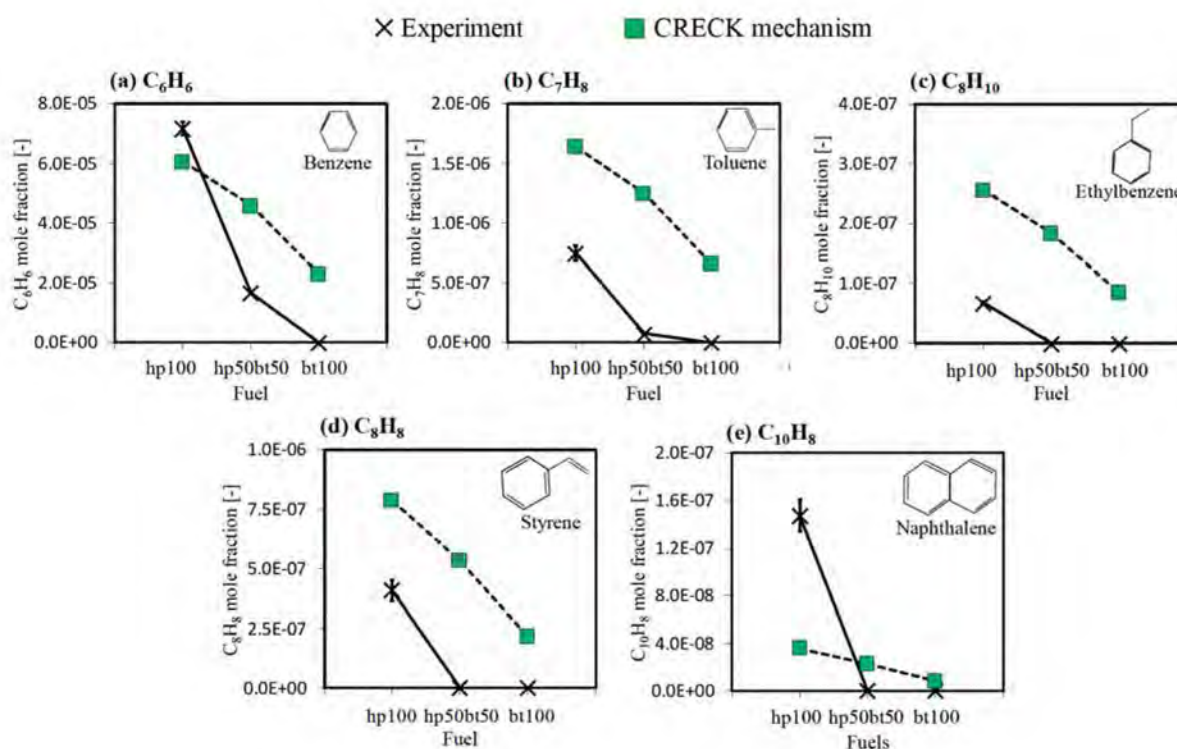

Fig. 3.5.2 Effects of butanol addition to *n*-heptane on C_6H_6, C_7H_8, C_8H_{10}, C_8H_8, and $C_{10}H_8$ at $U_0 = 10$ cm/s and $T_{w,max} = 1,100$ K.

3-6 Comparison of the effect of butanol addition to *n*-heptane for larger hydrocarbons and PAHs between measured species of hp50bt50 and hp50bt0

In order to determine PAHs reduction is due to the influence of the addition of butanol or mole fraction of *n*-heptane, the measured species of hp50bt50 and hp50bt0 were compared, and the results shown in Fig. 3.6.1. Note that, mole fraction of hp50bt0 is controlled by N_2 and it has the same mole fraction as the *n*-heptane in hp50bt50. Therefore, the effect of butanol addition to *n*-heptane for larger hydrocarbons and PAHs as well as the decrease in *n*-heptane can be distinguished.
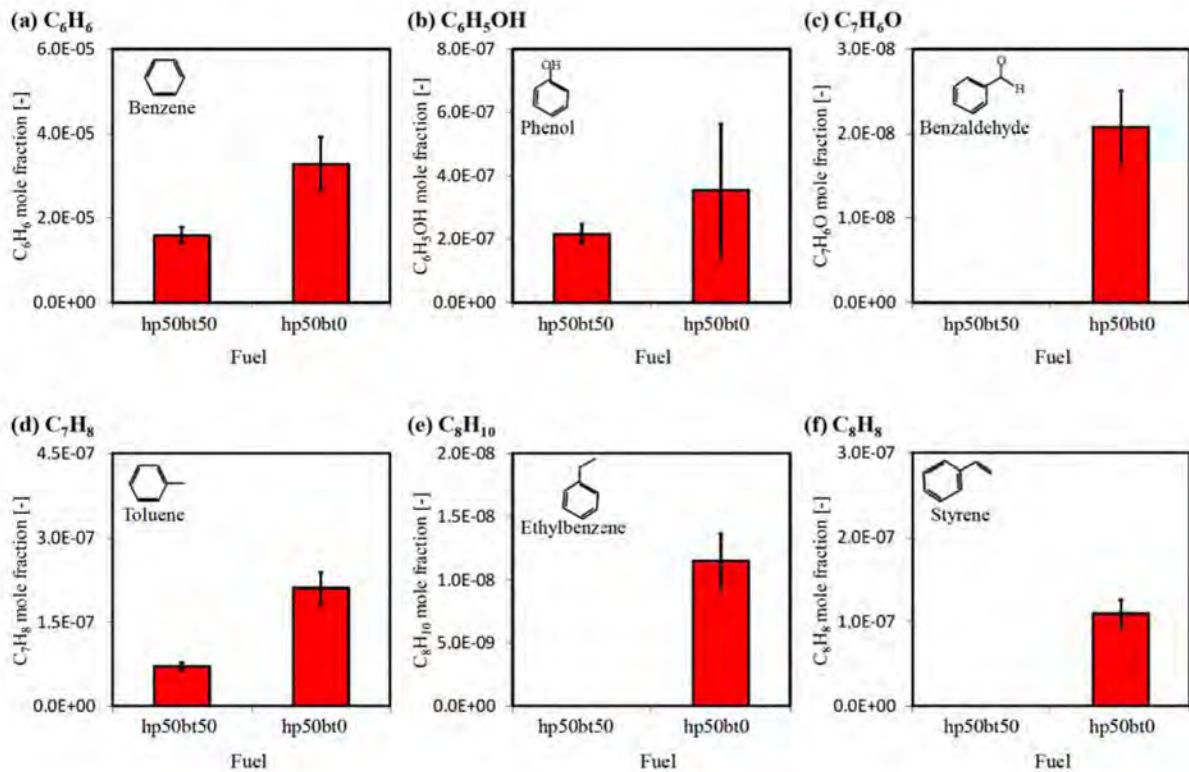
Fig. 3.6.1 Larger hydrocarbons and PAHs for all fuels between hp50bt50 and hp50bt0. a) C_6H_6 b) C_6H_5OH c) C_7H_6O d) C_7H_8 e) C_8H_{10} and f) C_8H_8. ($U_0 = 10$ cm/s, $\phi = 2.0$ and $T_{w,max} = 1,100$ K).

It can be seen that the mole fractions of PAHs higher in the case of hp50bt0 than hp50bt50. However, the concentration of naphthalene in the case of hp50bt50 and *n*-heptane diluted with

N_2 cannot be detected by GC/MS, due to its weak signal. Therefore, the figure corresponding to naphthalene is not shown in this section. However, it is evident that in the case of the other species, PAHs concentration decreased due to the addition of butanol instead of decreased *n*-heptane's mole fraction.

3-7 Summary

The species measurements of small hydrocarbons C_1 and C_2, consisting of C_2H_4, C_2H_2, C_2H_6, CH_4, CO, and CO_2 were carried out using GC-TCD. The behavior of the measurement species results was divided into three trends; the first consists of species concentration that are directly proportional to the equivalence ratios, which are C_2H_4, C_2H_2, C_2H_6, and CH_4 for all fuels. Second trend is shown by CO, CO concentration shows an increment at first and then slightly decrease with respect to equivalence ratios for hp100, while for hp50bt50 and bt100 shows an increment of CO concentration at first and then constant with respect to equivalence ratios. The third species that is concentration inversely proportional to the equivalence ratio, which is demonstrated by CO_2.

Several mechanisms were tested by comparing them with the measurement results of small hydrocarbon species C_1 and C_2. The tested mechanisms were the CRECK, Wang, KUCRS, Reduced Livermore, Detailed Livermore, Sarathy, and Veloo mechanisms. From the overall computational results, the CRECK mechanism reported satisfactory agreement with the measurement species, and due to this reason, the CRECK mechanism was used to compute the larger hydrocarbons and PAHs.

Next, species measurement for larger hydrocarbon and PAHs, such as C_6H_6, C_6H_5OH, C_7H_6O, C_8H_{10}, C_8H_8, and $C_{10}H_8$ were conducted using GC/MS. The computed species using the CRECK mechanism results with that of the measurement results were compared, and all of the species computed using the CRECK mechanism reported similar trends where the mole fraction of the species is directly proportional to the equivalence ratios. Overall, computed species concentration for C_6H_5OH, C_7H_6O, C_7H_8, C_8H_{10}, and C_8H_8 by the CRECK mechanism overestimates the measurement species, except in the case of C_6H_6 and $C_{10}H_8$.

All of the parameters in the experimental and computational methods reported in this chapter were performed under similar parametric conditions of the flame and soot response experiments outlined in Chapter 2, except in the case of the maximum wall temperature, which

was decreased from 1,300 K to 1,100 K to prevent soot formation and focus only on the region of gas phase of small and large hydrocarbons, as well as PAHs.

The PAHs' concentration of hp50bt50 was lower than that of PAHs of hp50bt0, which is due to the addition of butanol instead of the decrease in the mole fraction of *n*-heptane.

The effects of the addition of butanol to *n*-heptane onto soot precursors (C_2H_2 and C_2H_4), PAHs (C_6H_6, C_8H_{10}, C_8H_8 and $C_{10}H_8$), as well as CO and CO_2 were investigated by comparing the results obtained from the CRECK mechanism to that of the measurement results. It was confirmed that the mole fractions of C_2H_2, C_2H_4, C_6H_6, C_8H_{10}, C_8H_8, and $C_{10}H_8$ are inversely proportional to the mole percentage of butanol. CO and CO_2 are directly proportional to the mole percentage of butanol especially at higher equivalence ratios (3.0, 4.0 and 5.0). This implies that the addition of butanol to *n*-heptane enhances the role of carbon in increasing the rate of formation of CO and CO_2 instead of soot precursors and PAHs. The phenomenon process of soot precursors, PAHs, and CO and CO_2, its corresponding reaction path and rate of production analysis will all be elucidated in the next chapter.

Chapter 4

Reaction path and rate of production analyses

4-1 Introduction

The reaction path and rate of production analyses were conducted to elucidate the effect of the addition of butanol on small species (ethylene (C_2H_4), acetylene (C_2H_2), ethane (C_2H_6), methane (CH_4), carbon monoxide (CO), and carbon dioxide (CO_2)), as well as large hydrocarbons and PAHs such as benzene (C_6H_6), phenol (C_6H_5OH), benzaldehyde (C_7H_6O), toluene (C_7H_8), ethylbenzene (C_8H_{10}), styrene (C_8H_8), and naphthalene ($C_{10}H_8$).

From the results of the flame position (refer to Chapter 2, Section 2-6) and measuremet species (refer to Chapter 3, Section 3-4 and 3-5), the CRECK mechanism showed the best agreement relative to the other mechanisms. The CRECK mechanism was used to elucidate the reaction path and rate of production analyses.

The reaction path analyses were performed at $\phi = 2.0$, $U_0 = 10$ cm/s, and $T_{w,max} = 1,100$ K, since the effect of the addition of butanol on the measurement species was significant at these parameters (refer to Chapter 3, Section 3-5-1). The analyses were performed by selecting major rates of production reactions where the maximum heat release rate (HRR) occurs. These reactions represent the significant production and consumption reactions of the species.

4-2 Reaction path analyses

In order to elucidate the effect of effect of the addition of butanol on reaction pathways of the small and large hydrocarbons and PAHs, a comparison of reaction pathways between hp100, hp50bt50 and bt100 are shown in Fig. 4.2.1. Fuels: *n*-heptane (NC_7H_{16}) and *n*-butanol ($N1C_4H_9OH$)) are represented by the red ellipse. The production of the identified species such as small hydrocarbons (C_2H_4, C_2H_2, C_2H_6, CH_4, CO, and CO_2) are shown in the blue box, while large hydrocarbons and PAHs (C_6H_6, C_6H_5OH, C_7H_6O, C_8H_{10}, C_8H_8 and $C_{10}H_8$) are shown in the yellow box. To represent the number of reactions in the reaction path analyses, "R with number" was applied. For example, R4065 shows that the reaction of NC_7H_{16} forms NC_7H_{15}.

An explanation of reaction pathways for all fuels producing the identified species can be divided into two parts, where the first explains the reaction path of small hydrocarbons, while the second explain the large hydrocarbons and PAHs.

The reaction path for the first part is summarized in Fig. 4.2.1. Starting from the decomposition of the fuels by H abstraction via OH, which produces NC_7H_{15} from NC_7H_{16}, the products of the fuel decomposition react further to form C_2H_4. C_2H_4 is known to be one of soot's precursor [68]. Therefore, the formation of C_2H_5 is crucial towards the formation of higher PAHs. It can be seen from the figure that the formation of C_2H_4 comes via the formation of NC_4H_{9p} through C_2H_5. The reaction of C_2H_4 with OH forms C_2H_3, and continues on to form C_2H_2. The reaction between C_2H_4 and C_4H_5 also promotes the production of the first aromatic species, which is C_6H_6. From C_2H_3, further oxidation takes place to yield CH_2CHO, which then go on to form CH_2CO. The CH_2CO reacts with OH to yield CH_3 prior to producing CH_4. The same reaction also partially forms CO_2.

After the decomposition of the fuel, three main pathways for the measured species were evident. The first is the formation of C_7H_8, C_8H_{10}, and C_7H_6O via NC_4H_8. NC_4H_8 is formed from the decomposition of fuel and NC_7H_{15}. The formation of NC_4H_8 is important as it affect the subsequent concentrations of C_7H_8, C_8H_{10}, and C_7H_6O.
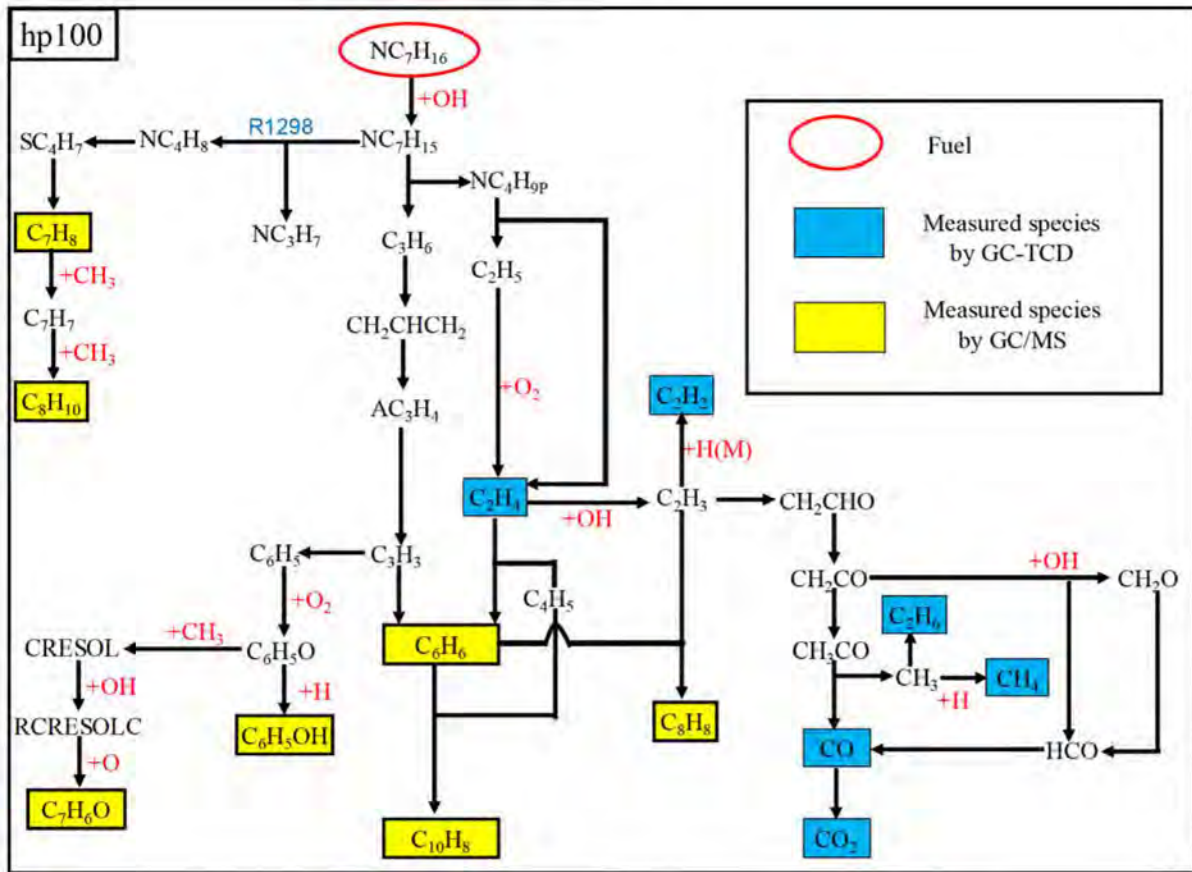
Fig. 4.2.1 Main reaction pathway analysis for hp100 at $U_0 = 10$ cm/s, $\phi = 2.0$, and $T_{w,max} = 1,100$ K.

The next phase is the formation of C_6H_6, $C_{10}H_8$, and C_8H_8 via C_2H_4 and C_3H_3. C_3H_3 undergoes self recombination to form C_6H_6. From Chapter 3, Section 3.4.2, the experimental and computational results for all of the fuels show that the mole fraction of C_6H_6 exceeds that of the other PAHs. The higher concentration of C_6H_6 could be due to the domination pathway of $2C_3H_3(+M) \Longleftrightarrow C_6H_6(+M)$ and $C_4H_5 + C_2H_4 \Longrightarrow C_6H_6 + H + H_2$. This supposition is also supported in Richter and Howard [110], where C_3H_3 is crucial towards the formation of benzene. The formation of C_6H_6 from C_2H_4 and C_3H_3 is regarded as the continuation product of NC_7H_{15}. Also, the decomposition of NC_7H_{15} contributes to the formation of C_3H_6 and NC_4H_{9p}. C_3H_6 is one of the small unsaturated hydrocarbon species that leads to the production of small aromatics and PAHs [28]. The third phase is the formation of C_6H_5OH via C_3H_3. C_3H_3 is further

divided into reactions forming larger hydrocarbons (C_6H_5OH) and PAHs (C_6H_6, $C_{10}H_8$ and C_8H_8).

The reaction pathway for the addition of butanol is shown in Fig. 4.2.2. The addition of butanol resulted in a significant difference in the reaction pathway relative to that of the base fuel (hp100) as shown in green arrow. However, since it possess components from *n*-heptane, most of the reactions are similar to the reaction path of hp100. It can be seen that the reaction from NC_7H_{16} identify species of small and large hydrocarbons, as well as PAHs, which is similar to the reaction path of hp100.
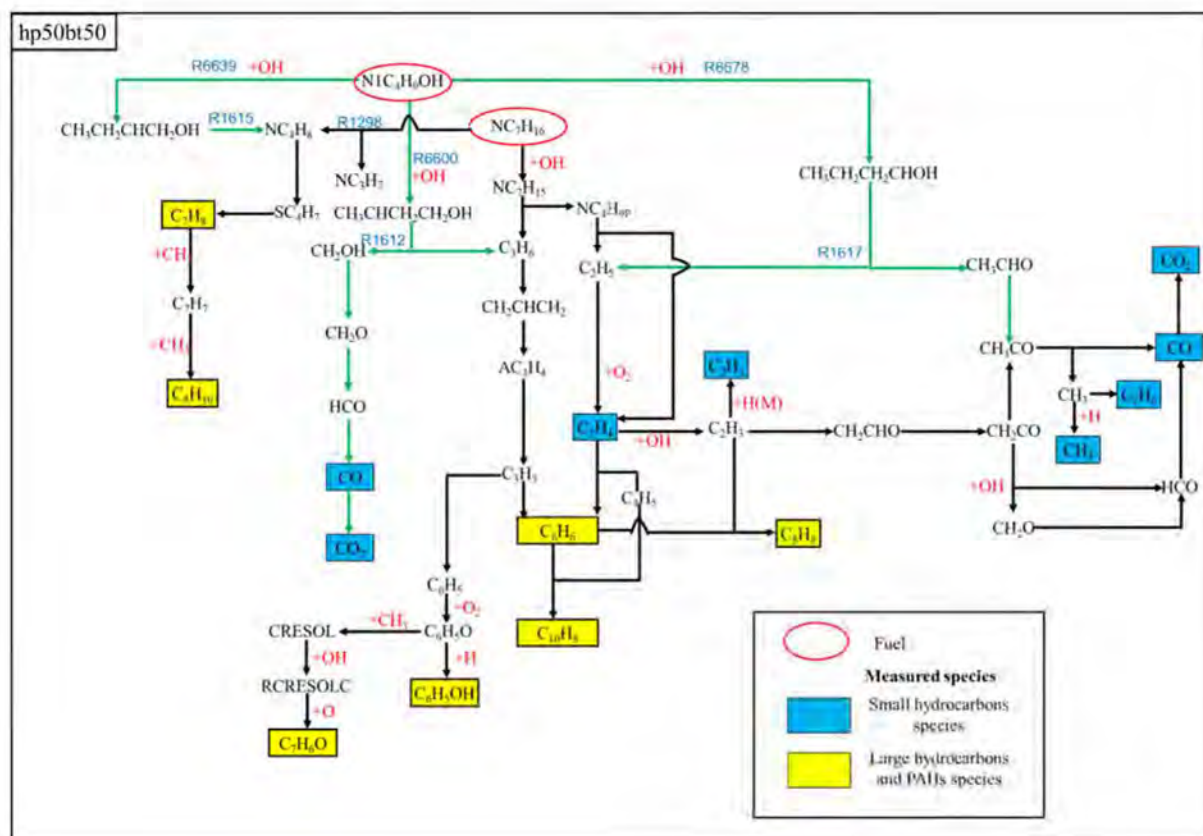

Fig 4.2.2 Main reaction pathway analysis for hp50bt50 at $U_0 = 10$ cm/s, $\phi = 2.0$, and $T_{w,max} = 1,100$ K.

The addition of $N1C_4H_9OH$ resulted in new reactions. $N1C_4H_9OH$ changes the reaction pathway(s), as per R6600, R6639, and R6678. These reactions represent the decomposition of

N1C$_4$H$_9$OH to form CH$_3$CHCH$_2$CH$_2$OH, CH$_3$CH$_2$CHCH$_2$OH, and CH$_3$CH$_2$CH$_2$CHOH, with H abstraction via OH. These hydroxybutyl radicals play an important role to the reduction of the measured species of small and large hydrocarbons, as well as PAHs. The production of these hydroxylbutyl radicals resulted in the production of different species for hp50bt50. For example, the formation of CH$_3$CHCH$_2$CH$_2$OH in R6600 was followed by R1612, which produced C$_3$H$_6$ and CH$_2$OH. As pointed out previously, the formation of C$_3$H$_6$ is also influenced by R1297 from NC$_7$H$_{15}$, while the formation of CH$_2$OH led to the formation of CO$_2$. Furthermore, the formation of C$_3$H$_6$ led to the formation of C$_3$H$_3$ formation, which controls the concentrations of C$_6$H$_6$, C$_{10}$H$_8$, C$_8$H$_8$, C$_7$H$_6$O, and C$_6$H$_5$OH.

The formation of CO$_2$ from butanol could result in the reduction of PAHs. According to Westbrook et al. [28], the addition of oxygenated fuel such as butanol result in the formation of CO and CO$_2$. Both are strongly bonded carbon atoms, which prevents the atoms from participating in the production of soot. Another formation of hydroxybutyl radicals, such as CH$_3$CH$_2$CHCH$_2$OH in R6639, promotes R1615 on the formation of NC$_4$H$_8$, which is also formed from NC$_7$H$_{15}$ in R1298. The formation of NC$_4$H$_8$ from both reactions resulted in the decrease of the concentrations of C$_7$H$_8$ and C$_8$H$_{10}$. The product of R6678, given by CH$_3$CH$_2$CH$_2$CHOH, was also among the most prominent reaction that reduced PAHs. It was evident that CH$_3$CHO and C$_2$H$_5$ were produced from CH$_3$CH$_2$CH$_2$CHOH in R1617. CH$_3$CHO also demonstrated similar final direction to that of CH$_2$OH, as pointed out previously. Also, C$_2$H$_5$ led to the production of C$_2$H$_4$ and subsequently to the reduction of C$_6$H$_6$, C$_{10}$H$_8$, and C$_8$H$_8$.

The reaction path of bt100 is not shown in this work, due to the fact that the reaction is almost similar to that of hp50bt50. Bearing this fact in mind, only a short brief of the reaction path of bt100 is shown here. N1C$_4$H$_9$OH produces hydroxybutyl radicals via R6639, R6600, and R6678. Since no sources of hp100 contributes to the soot precursor, the concentrations of C$_2$H$_4$ and C$_2$H$_2$ decreased. Subsequently, the concentrations of larger hydrocarbons and PAHs (C$_6$H$_6$, C$_6$H$_5$OH, C$_7$H$_6$O, C$_8$H$_{10}$, C$_8$H$_8$ and C$_{10}$H$_8$) decreased as well.

In summary, the results confirmed that hydroxybutyl radicals' reaction in R1612 ($CH_3CHCH_2CH_2OH \Leftrightarrow C_3H_6 + CH_2OH$), R1615 ($CH_3CH_2CHCH_2OH \Leftrightarrow NC_4H_8 + OH$) and R1617 ($CH_3CH_2CH_2CHOH \Leftrightarrow CH_3CHO + C_2H_5$) plays a major role during the addition of butanol on the formation of C_6H_6, C_6H_5OH, C_7H_6O, C_7H_8, C_8H_{10}, C_8H_8, and $C_{10}H_8$. Also, R1612 and R1617 dictate the ratio between PAHs or CO_2, which eventually influence the formation of soot. Low concentrations of PAHs results in the reduction of soot formation.

The upcoming sections detail the main species of soot precursors. Also, for comparison purposes with the CREEK mechanism, the reaction path analysis for the Wang mechanism is detailed in Appendix 4-A.

4-3 Major reaction analyses

As outlined in Chapter 3, Section 3-5-1, soot reduction is reliant upon the reduction of the concentration of soot precursors. This necessitates a detailed study on major reactions involved in the formation of soot precursors. The three main species that are imperative towards the formation of soot precursors, such as primary hydrocarbons (C_2H_4), intermediates (C_6H_6), and largest PAHs ($C_{10}H_8$) were selected, as per the main reaction pathway in Figs 4.2.1 and 4.2.2. These species represent the continuity formation from C_2H_4 to C_6H_6, leading to the formation of $C_{10}H_8$. In order to aid in the interpretation of the measurement species, the total rate of production/consumption for hp100, hp50bt50, and bt100 were set at $\phi = 2.0$ and $T_{w,max}$ = 1,100 K, and analyzed using the CRECK mechanism. The total rates of production/consumption plays a crucial role towards confirming the trend of the experimental results, where positive values represent production behaviors, while negative values represent consumption behaviors.

Figures 4.3.1(a), 4.3.2(a), and 4.3.3(a) show the total rate of production/consumption of C_2H_4, C_6H_6, and $C_{10}H_8$. The total rates of production/consumption are representative of the experimentally observed trend (as per Figures 3.4.1 and 3.5.1). The total production and consumption for C_2H_4, C_6H_6, and $C_{10}H_8$ are evidently well balanced. It shows that the net reaction of the production and consumption for these species decreases when the mole percentage of butanol increases (inverse relationship). These results are in agreement with the experimental results.

To determine the major reactions contributing to the net production/consumption, the top three production/consumption reactions are shown in Figures 4.3.1(b), 4.3.2(b) and 4.3.3(b).

4-3-1 Rate of C_2H_4 production/consumption

As evident in Figure 4.3.1(b), most of the production rate of C_2H_4 is related to the C_2H_5 reactions in hp100. The main reactions are R223: $O_2+C_2H_5 \Rightarrow HO_2+C_2H_4$, which continues to

R757: $NC_4H_{9P} \Longleftrightarrow C_2H_5 + C_2H_4$. However, when butanol was introduced (hp50bt50), the reaction of R757 decreased, and the position of the second dominant reaction was overtaken by R95. This implies that the addition of butanol enhances the formation of NC_3H_7 $NC_3H_7 \Longleftrightarrow CH_3 + C_2H_4$. In the case of bt100, R757 is not present, since NC_4H_{9P} in R757 is available only for hp100.
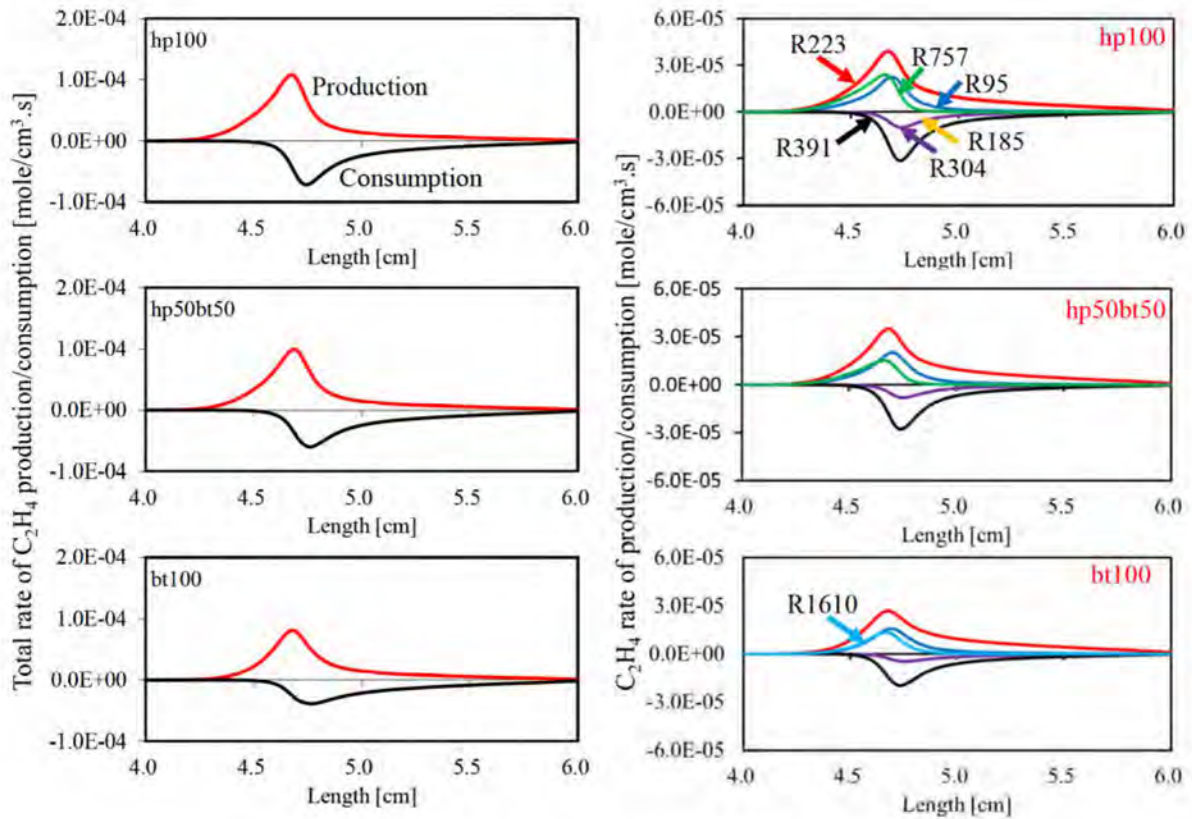
Reaction	C_2H_4
Production	
R223	$O_2 + C_2H_5 \Rightarrow HO_2 + C_2H_4$
R757	$NC_4H_9P \Longleftrightarrow C_2H_5 + C_2H_4$
R95	$NC_3H_7 \Longleftrightarrow CH_3 + C_2H_4$
R1610	$CH_2CH_2CH_2CH_2OH \Longleftrightarrow C_2H_4 + C_2H_4OH$
Consumption	
R391	$OH + C_2H_4 \Longleftrightarrow H_2O + C_2H_3$
R185	$O + C_2H_4 \Longleftrightarrow CH_3 + HCO$
R304	$O + C_2H_4 \Rightarrow CH_2CHO + H$

Fig. 4.3.1 (a) Total rate of C_2H_4 production/consumption (b) Major reactions of C_2H_4 production/consumption for all fuels at $U_0 = 10$ cm/s, $\phi = 2.0$ and $T_{w,max} = 1,100$ K.

On the other hand, R1610 $CH_2CH_2CH_2CH_2OH<=>C_2H_4+C_2H_4OH$ production has taken place in the top three of the C_2H_4 production rate in bt100. For consumption reactions, R391: $OH+C_2H_4<=>H_2O+C_2H_3$ is dominant in the case of all fuels. A large discrepancy between R391 and other consumption reactions (R304 and R185) is evident in hp100 and hp50bt50, which means that R391 plays an important role in the concentration of C_2H_4.
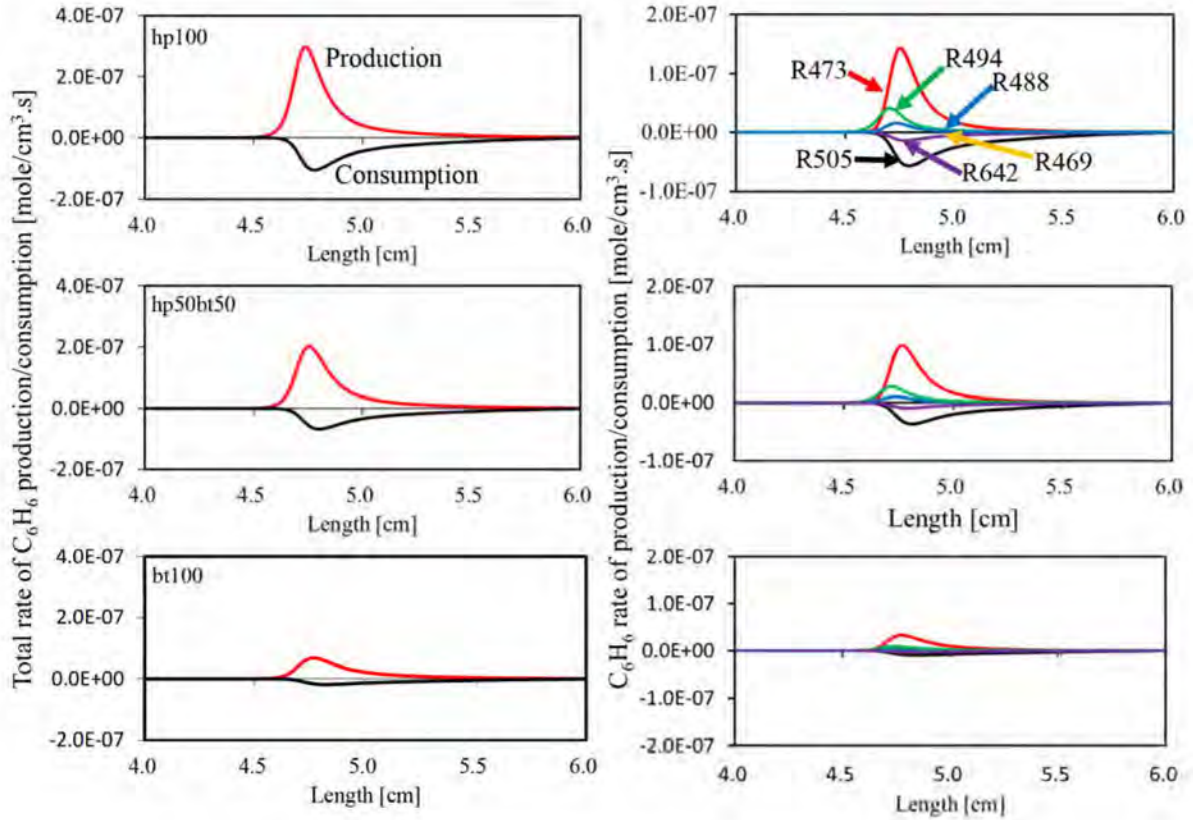
4-3-2 Rate of C_6H_6 production/consumption

Based on the reaction path analysis (refer Figure 4.2.1), C_6H_6 is formed after C_2H_4. Therefore, the production/consumption of C_6H_6 is discussed in this section. Figure 4.3.1 shows the total rate of C_6H_6 production and the main reactions involved in the production/consumption of C_6H_6.

C_2H_6 production/consumption also shows a decrease with increasing mole percentage of butanol, showing a similar trend with the rate of the production/consumption of C_2H_4. Figure 4.3.2 (b) show the main reactions of C_6H_6 production contributed by R473: $2C_3H_3(+M)<=>C_6H_6(+M)$, R494: $C_4H_5+C_2H_4=>C_6H_6+H+H_2$, and R488: $CH_2CHCH_2+PC_3H_4=>C_6H_6+H_2+H$. R473, confirming that the self reaction of C_3H_3 significantly contribute towards the formation of C_6H_6. This supposition is also supported in [107], where C_3H_3 plays an important role in the formation of benzene. The reaction by C_2H_4 plays an important role in the formation of C_6H_6, meaning that the higher concentration of C_2H_4 leads to a higher concentration of C_6H_6.

In previously reported results (refer to Fig. 3.5.1), the experimental and computational values for all of the fuels confirmed that the mole fraction of C_6H_6 exceeded that of the other PAHs. This higher concentration of C_6H_6 could be due to the domination pathway of R473 from to its large peak area relative to both R494 and R488. Based on the reaction path analysis seen in Figs. 4.2.1 and 4.2.2, the formation of C_6H_6 from C_2H_4 and C_3H_3 represents the continuation product of NC_7H_{15}. The decomposition of NC_7H_{15} contributed to the formation of C_3H_6 and

NC_4H_{9p}. Therefore, the formation of C_2H_4 from R494 and C_3H_3 from R473 are crucial towards the formation of C_6H_6.

Reaction	C_6H_6
	Production
R473	$2C_3H_3(+M)<=>C_6H_6(+M)$
R494	$C_4H_5+C_2H_4=>C_6H_6+H+H_2$
R488	$CH_2CHCH_2+PC_3H_4=>C_6H_6+H_2+H$
	Consumption
R505	$H+C_6H_6<=>H_2+C_6H_5$
R642	$O+C_6H_6<=>C_6H_5O+H$
R469	$OH+C_6H_6=>CYC_5H_6+CO+H$

Fig. 4.3.2 (a) Total rate of C_6H_6 production/consumption (b) Major reactions of C_6H_6 production/consumption for all fuels at $U_0 = 10$ cm/s, $\phi = 2.0$ and $T_{w,max} = 1,100$ K.

The effect of butanol is significant to the production (R473, R494, and R488) and consumption reactions (R505, R642 and R469), as it decreases with increasing mole percentage of butanol shown in hp50bt50 and bt100. This implies that the production of C_6H_6 can be

inhibited when butanol is introduced into the mixture.

4-3-3 Rate of $C_{10}H_8$ production/consumption

The largest measured PAHs in this study is that of $C_{10}H_8$. The main reactions of production and consumption are shown in Figure 4.3.3. The total rate of $C_{10}H_8$ for hp100 is evidently higher in terms of production/consumption relative to fuels containing butanol (hp50bt50 and bt100).

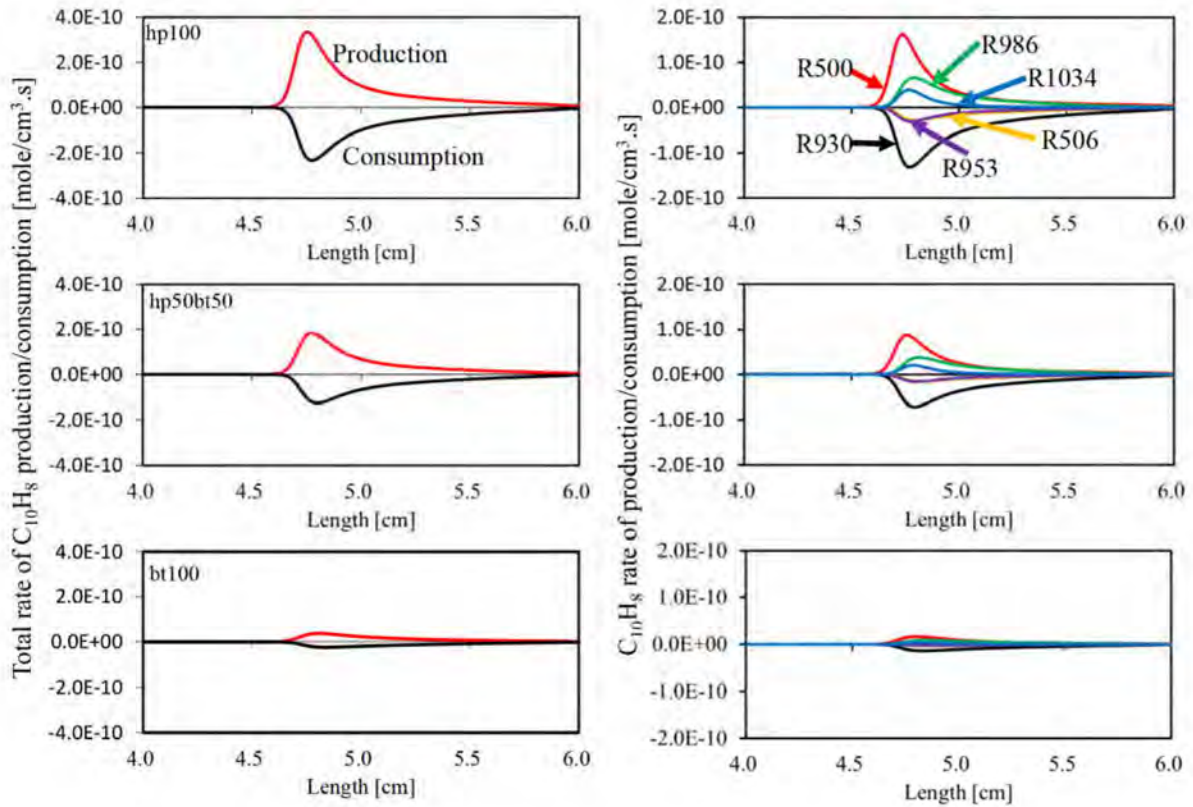| Reaction	$C_{10}H_8$
	Production
R500	$C_4H_5+C_6H_6 => C_{10}H_8+H_2+H$
R986	$H+C_{10}H_7OH => C_{10}H_8+OH$
R1034	$C_3H_3+C_7H_7 => C_{10}H_8+2H$
	Consumption
R930	$OH+C_{10}H_8 => H_2O+C_{10}H_7$
R953	$O+C_{10}H_8 <=> C_{10}H_7O+H$
R506	$H+C_{10}H_8 => C_6H_5+C_4H_4$

Fig. 4.3.3 (a) Total rate of $C_{10}H_8$ production/consumption (b) Major reactions of $C_{10}H_8$ production/consumption for all fuels at $U_0 = 10$ cm/s, $\phi = 2.0$ and $T_{w,max} = 1,100$ K.

The total rate of $C_{10}H_8$ production was mostly formed by the smallest PAHs, which in this case was C_6H_6. This is shown by R500: $C_4H_5+C_6H_6=>C_{10}H_8+H_2+H$, and continued by R986: $H+C_{10}H_7OH=>C_{10}H_8+OH$ and R1034: $C_3H_3+C_7H_7=>C_{10}H_8+2H$. The trend of these reactions are similar in the case of all of the fuels (hp100, hp50bt50, and bt100). However, it is inversely proportional to the butanol mole percentage.

4-4 Discrepancy of *n*-heptane/*n*-butanol mixture flame mechanisms: revisited

As pointed out previously (Chapter 2, Section 2-3), chemical reactions involving *n*-butanol and *n*-heptane was only evident in the CRECK and Wang mechanisms. However, from the previous results of flame position of the measurement species of small and large hydrocarbons and PAHs, the CRECK measurement are in better agreement relative to the Wang mechanism. This discrepancy can be explained by the fact that C_2H_2 was selected as a representative species, and was investigated in the context of mole fraction profile along the axial length. All of the fuels reported similar trends, and hp100 was selected as a reprensative of the behavior of mole fraction.

Figure 4.4.1 shows the computational profiles of the C_2H_2 mole fraction from the hp100 fuel using the CRECK and Wang mechanisms. In the case of the former, the C_2H_2 mole fraction used a peak as an intermediate at the flame position prior to maintaining a constant value up till the end of the tube, while in the case of the latter, the peak behaves differently, where the C_2H_2 mole fraction demonstrating a continuously decreasing trend. In order to elucidate these trends in the context of the computed C_2H_2, the rate of C_2H_2 production was analyzed at parameters of $\phi = 2.0$ and $T_{w,max} = 1,100$ K in the case of the CRECK and Wang mechanism. Figure 4.4.2 shows the rate of production of C_2H_2 computed using the CRECK and Wang mechanisms for hp100 fuel. The major reactions in the case of C_2H_2 consumption as a function of temperature distributions are also shown in the figure. The CRECK mechanism reported a zero rate of C_2H_2

production in the low-temperature region (under ~800 K) towards the end of the reactor, confirming the lack of reactions in this region.

The Wang mechanism reported a negative rate of C_2H_2 production in the low temperature region (under ~800 K). The C_2H_2 production behaviors were obtained from R130: $C_2H_2+H<=>C_2H_3$ and R268: $C_2H_2+C_2H_3<=>C_4H_5$. These reactions reduced the C_2H_2 mole fraction within the lower temperature region (downstream side of the quartz tube), and subsequently induced a different trend in the C_2H_2 mole fraction profile between the CRECK and Wang mechanisms.
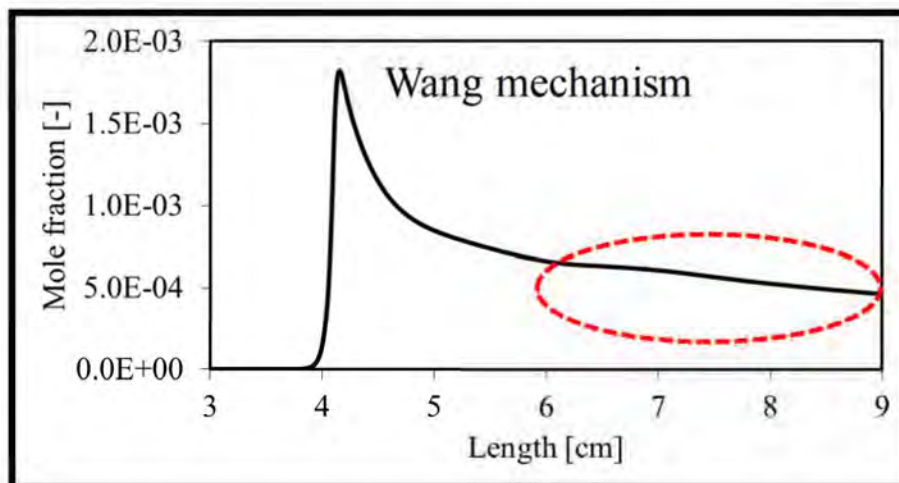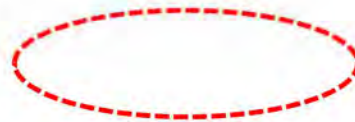
Figure 4.4.1 Computation of C_2H_2 from hp100 mole fraction profile by the CRECK and Wang mechanisms at $U_0 = 10$ cm/s, $\phi = 2.0$, and $T_{w,max} = 1,100$ K.

Wall temperature [K]

973   782   589   468   416   393   393

CRECK mechanism

R350: $C_2H_2+O<=>HCCO+H$

R349: $C_2H_2+O<=>CH_2+CO$

R305: $OH+C_2H_2=>CH_2CHO$

R205: $HO_2+C_2H_2=>CH_2O+HCO$

Wall temperature [K]

973   782   589   468   416   393   393

Wang mechanism

R211: $C_2H_2+H(+M)<=>C_2H_3(+M)$

R263: $C_2H_3+C_2H_2<=>H+C_4H_4$

R268: $C_2H_3+C_2H_2<=>C_4H_5$

R130: $C_2H_2+H<=>C_2H_3$
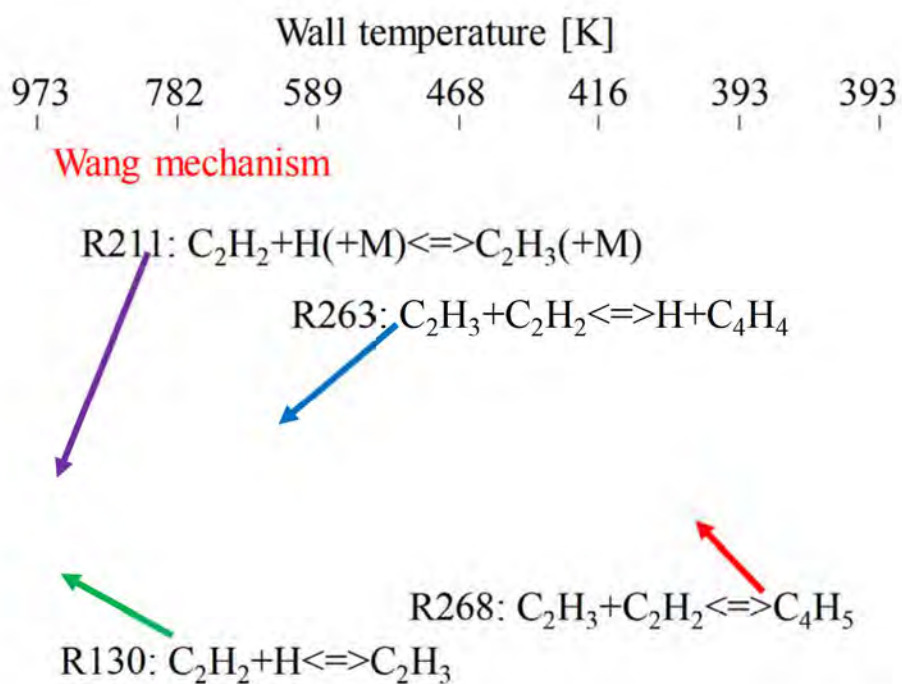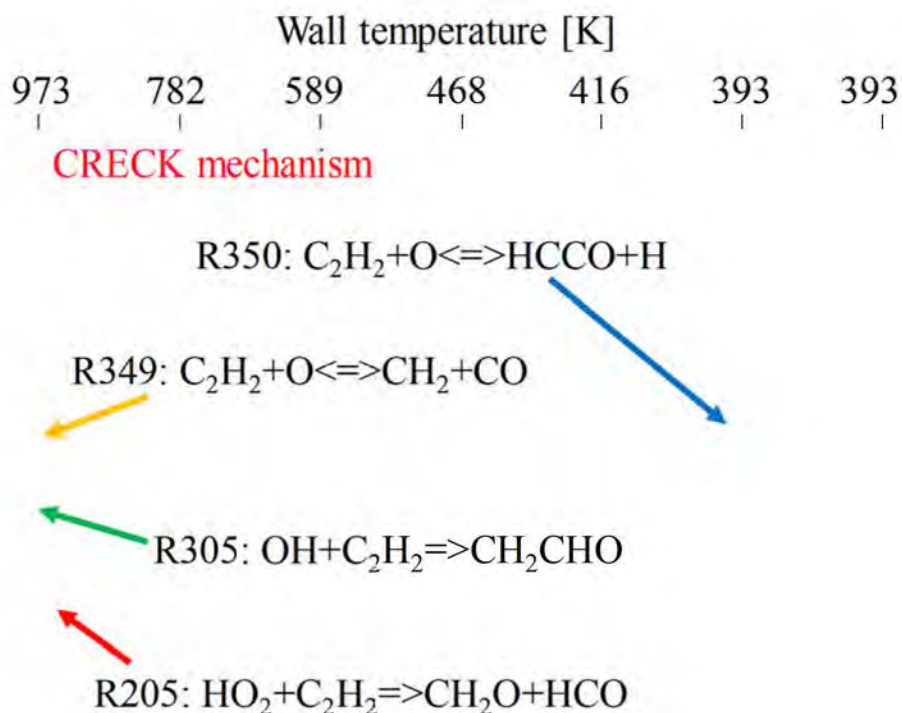
Figure 4.4.2 • • • • • ◦•• ••• ••••••••••••••••••••••• • • • • • • • $U_0 = 10$ cm/s, • • • • •

$\phi = 2.0$, and $T_{w,max} = 1,100$ K.

Both reactions (corresponding to R130 and R268 in the Wang mechanism) were included in the CRECK mechanism to represent R83 and R43. However, these reactions are not the top three reactions in the CRECK mechanism, and the kinetic parameters in the CRECK mechanism differed from those of the Wang mechanism, as per Table 4.4.1.

Table 4.4.1 Kinetic parameter for Wang and CRECK mechanisms

Wang mechanism				
Reaction Number	Reaction	A	B	E
R130	$C_2H_3 = C_2H_2 + H$	4.60E+40	-8.80	46200.
R268	$C_4H_5 <=> C_2H_3 + C_2H_2$	0.10E+15	0	43610
CRECK mechanism				
R83	$C_2H_2 + H(+M) = C_2H_3(+M)$	0.10E+14	0	2770
R43	$C_4H_5 = C_2H_3 + C_2H_2$	0.75E+13	0	40000

The rates of C_2H_2 production computed using the CRECK mechanism using reactions R83 and R43 are shown in Fig. 4.4.3. The reactions (corresponding to R84 and R43 in the CRECK mechanism) shows zero rate of C_2H_2 production within the low temperature region, which is expected. The finite consumption of C_2H_2 shown by the Wang mechanism within the low temperature region shown in Fig. 4.4.2 led to the underestimation of C_2H_2.

4-5 Summary

The effect of the addition of butanol on the reaction path and rate of production/consumption using the CRECK mechanism was elucidated in this chapter. The production of the measured species by GC-TCD, such as small hydrocarbons (C_2H_4, C_2H_2, C_2H_6, CH_4, CO, and CO_2), large hydrocarbons, as well as PAHs (C_6H_6, C_6H_5OH, C_7H_6O, C_8H_{10}, C_8H_8, and $C_{10}H_8$) measured by GC/MS are shown in the reaction path.

The addition of butanol on the *n*-heptane resulted in three main reactions involving hydroxybutyl radicals, which were $CH_3CHCH_2CH_2OH$, $CH_3CH_2CHCH_2OH$, and $CH_3CH_2CH_2CHOH$. These radicals decompose and react with C_3H_6, CH_2OH, NC_4H_8, CH_3CHO, and C_2H_5, which result in the reduction of small and large hydrocarbons, as well as PAHs. These reactions are: R1612 ($CH_3CHCH_2CH_2OH<=>C_3H_6+CH_2OH$), R1615 ($CH_3CH_2CHCH_2OH<=>NC_4H_8+OH$) and R1617 ($CH_3CH_2CH_2CHOH<=>CH_3CHO+C_2H_5$).

The effect of the addition of butanol on the three main species of soot precursors, which are primary hydrocarbon (C_2H_4), intermediate and largest PAHs (C_6H_6, and $C_{10}H_8$), were determined by analyzing the total rates of production/consumption and the top three major production/consumption reactions for hp100, hp50bt50, and bt100 at $\phi = 2.0$, and $T_{w,max} = 1,100$ K using the CRECK mechanism. The reduction of C_2H_4 is caused by the production reaction of R95: $NC_3H_7<=>CH_3+C_2H_4$ and consumption reaction of R391: $OH+C_2H_4<=>H_2O+C_2H_3$. In the case of the smallest PAHs, which is C_6H_6, the self-reaction by R473: $2C_3H_3(+M)<=>C_6H_6(+M)$ was identified as the dominant reaction. The formation of C_6H_6 also influenced the formation of $C_{10}H_8$ via R500: $C_4H_5+C_6H_6=>C_{10}H_8+H_2+H$.

The overall trend of the total rate of production/consumption and the contribution of reactions to the trend of soot precursors were determined. The total rate of production/consumption of soot precursors is inversely related to the mole percentage of butanol.

Mechanisms covering fuel *n*-heptane and *n*-butanol were the CRECK and Wang

mechanisms. The rate of production analysis for C_2H_2 by the CRECK and Wang mechanism were also determined, and we managed to identify the possible cause of the large discrepancy between the experimental and computation results, which is the negative rates of the C_2H_2 production in the low-temperature region by R130: $C_2H_2+H<=>C_2H_3$ and R268: $C_2H_2+C_2H_3<=>C_4H_5$ in the Wang mechanism.

Appendix 4-A Reaction path analysis of Wang mechanism

Figure 4.A.1 shows the reaction path analysis for all of the fuels at $\phi = 2.0$ and $T_{w,max}$ = 1,100 K using the Wang mechanism. It shows a similar reaction path with that of the CRECK mechanism, despite the fact that theWang mechanism not being able to reproduce experiments quantitatively. Therefore, the only reaction path involving small hydrocarbons is shown here, which are C_2H_4, C_2H_2, CH_4, CO, and CO_2 (illustrated in small box).
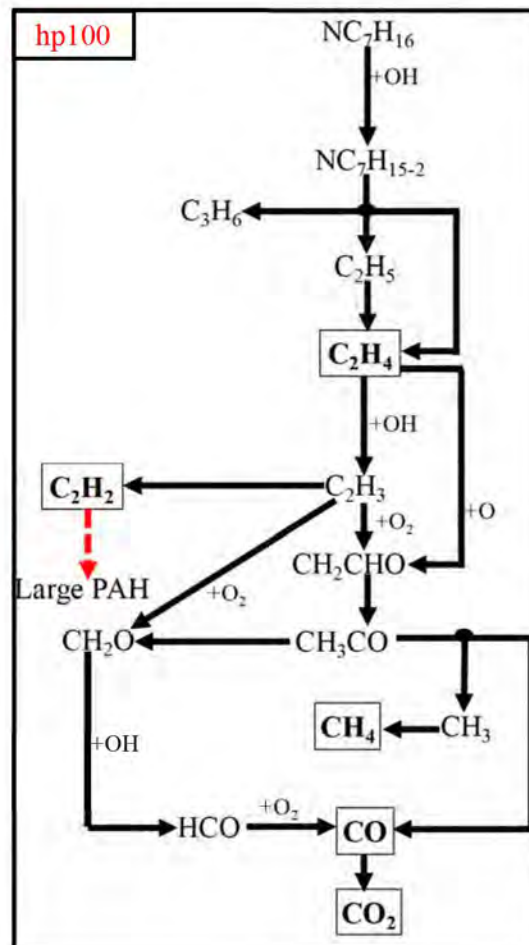
Figure 4.A.1 Reaction path analyses for Wang mechanism

Starting with the decomposition of fuel (NC_7H_{16}) to C_2H_4 via NC_7H_{15-2} and C_2H_5. The C_2H_4 mole fraction of the Wang mechanism shows excellent trend with the measurement results, as shown in Fig. 3.4.1 in Chapter 3.

C_2H_2, known as the former PAH, is formed after the reaction C_2H_4 via C_2H_3. Due to this fact, the mole fractions of C_2H_4 and C_2H_2 are proportional to one another. C_2H_2 continues to form larger PAHs.

C_2H_3 will produce CH_2CHO, then CH_3CO. CH_3CO will then go on to produce CH_4 via CH_3. The same CH_3CO reaction partially forms CH_2O and HCO prior to forming CO and CO_2.
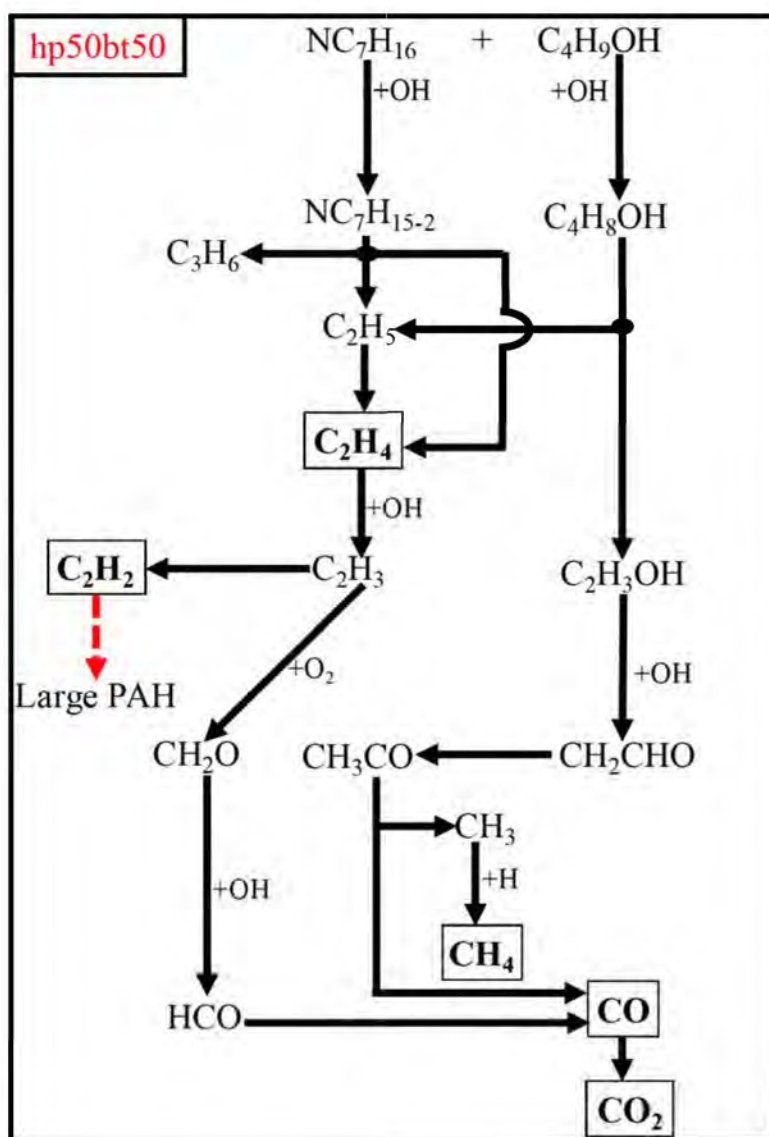
Figure 4.A.2 Reaction path analyses for hp50bt50 by Wang mechanism

The reaction path analyses for hp50bt50 by the Wang mechanism is shown in Fig. 4.A.2. The reaction path for hp50bt50 shows a similar reaction path with that of the hp100, since *n*-heptane is included in the mixture. However, the addition of butanol changed the C_2H_5 species. C_4H_9OH was oxidized with OH to produce C_4H_8OH. C_4H_8OH then go on to form C_2H_5 and C_2H_3OH.

It can be seen that C_2H_5 from C_4H_9OH is related to C_2H_4 and C_2H_2. It can be surmised that C_2H_5 species is an important key species when butanol is added to *n*-heptane. The produced C_2H_3OH will then go on to produce CH_4, CO, and CO_2.

Chapter 5

Summary and Conclusions

The impact of the addition of butanol to sooting tendency and PAHs formation behaviors have been investigated using a micro-flow reactor with a controlled temperature profile (MFR). The following conclusions were made:

Species measurement, which were produced from the *n*-heptane/*n*-butanol mixtures flames, were investigated. The measurement species was divided into two parts: (1) Small hydrocarbons of C_1 and C_2 species by GC-TCD, and (2) larger hydrocarbons and PAHs by GC/MS. Both parts were tested under similar parameters: inlet mean velocity, $U_0 = 10$ cm/s, pressure, $P = 1$ atm, and maximum wall temperature, $T_{w,max} = 1,100$ K. It can be concluded that:

(1) Small hydrocarbons of C_1 and C_2 species by the GC-TCD measurement.

in hp50bt50 were smaller relative to the same species in hp50bt0.

The discrepancy of the *n*-heptane/*n*-butanol mixture involved in the CRECK and Wang mechanisms were elucidated.

References

[1]   J. Warnatz, U. Maas, R.W. Dibble, Combustion: physical and chemical fundamentals, modeling and simulation, experiments, pollutant formation., Springer. (2006) Springer.

[2]   BP energy outlook 2035, (2014).

        URL: https://www.bp.com/en/global/corporate/energy-economics/energy-outlook.html.

[3]   The world bank, Reducing black carbon emissions from diesel vehicles: impacts, control strategies, and cost-benefit analysis, (2014).

        URL:http://documents.worldbank.org/curated/en/329901468151500078/pdf/864850W P00PUBL0l0report002April2014.pdf.

[4]   J.M. Cristiano Façanha, Kate Blumberg, Global transportation energy and climate roadmap, International Council on Clean Transportation, (2012).

        URL:https://www.theicct.org/publications/global-transportation-energy-and-climate-roadmap.

[5]   T.R. Barfknecht, Toxicology of soot, Progress in Energy and Combustion Science, 9 (1983) 199–237.

[6]   T. Nielsen, H.E. Jsrgensen, J.C. Larsenb, M. Poulsenb, City air pollution of polycyclic aromatic hydrocarbons and other mutagens: occurrence, sources and health effects, The Science of the Total Environment, 189/190 (1996) 41–49.

[7]   M.O. Andreae, The dark side of aerosols, Nature, 409 (2001) 671–672.

[8]   D.A. Green, R. Lewis, Effect of soot on oil properties and wear of engine components, Journal of Physics D: Applied Physics, 40 (2007) 5488.

[9]   E. Hu, X. Hu, T. Liu, L. Fang, K.D. Dearn, H. Xu, The role of soot particles in the tribological behavior of engine lubricating oils, Wear, 304 (2013) 152–161.

[10]   United States Environmental Protection Agency (USEPA), Office of air and radiation, office of air quality planning and standards, 1997.

[11]   C.I. Falcon-Rodriguez, A.R. Osornio-Vargas, I. Sada-ovalle, P. Segura-medina, Aeroparticles, composition, and lung diseases, Frontiers in Immunology, 7 (2016).

[12]   T.C. Bond, S.J. Doherty, D.W. Fahey, P.M. Forster, T. Berntsen, B.J. Deangelo, M.G. Flanner, S. Ghan, B. Kärcher, D. Koch, S. Kinne, Y. Kondo, P.K. Quinn, M.C. Sarofim, M.G. Schultz, M. Schulz, C. Venkataraman, H. Zhang, S. Zhang, N. Bellouin, S.K. Guttikunda, P.K. Hopke, M.Z. Jacobson, J.W. Kaiser, Z. Klimont, U. Lohmann, J.P. Schwarz, D. Shindell, T. Storelvmo, S.G. Warren, C.S. Zender, Bounding the role of black carbon in the climate system: A scientific assessment, Journal of Geophysical Research Atmospheres, 118 (2013) 5380–5552.

[13]   URL: http://www.adsystems-sa.com.

[14]   W.M.F.W. Mahmood, Computational studies of soot paths to cylinder wall layers of a direct injection diesel engine, PhD thesis, University of Nottingham, (2011).

[15]   R. Mainwaring, Soot and wear in heavy duty diesel engines, SAE Paper, (1997) 971631.

[16]   O. Orhan, E. Haffner-staton, A. La Rocca, M. Fay, Tribology international

characterisation of flame-generated soot and soot-in-oil using electron tomography volume reconstructions and comparison with traditional 2D-TEM measurements, Tribiology International, 104 (2016) 272–284.

[17] D.A. Green, R. Lewis, The effects of soot-contaminated engine oil on wear and friction: a review, Journal of Automobile Engineering, 222 (2008) 1669–1689.

[18] A. Jess, What might be the energy demand and energy mix to reconcile the world's pursuit of welfare and happiness with the necessity to preserve the integrity of the biosphere?, Energy Policy, 38 (2010) 4663–4678.

[19] I.E.A. (IEA), Technology roadmap: biofuels for transport, OECD Publishing, 2011.

URL: https://www.iea.org/topics/renewables/technologyroadmaps/.

[20] Carbon disclosure project Transport report: analysis based on CDP 2009 data, 2009.

URL: https://trid.trb.org/view.aspx?id=1150985.

[21] S. Yamamoto, S. Watanabe, K. Komada, D. Sakaguchi, H. Ueki, M. Ishida, Study on combustion and soot emission of ethanol or butanol blended with gas oil in a direct injection diesel engine, SAE International Journal Fuels Lubricant, 6 (2013) 1021–1031.

[22] D.C. Rakopoulos, C.D. Rakopoulos, E.G. Giakoumis, A.M. Dimaratos, D.C. Kyritsis, Effects of butanol–diesel fuel blends on the performance and emissions of a high-speed DI diesel engine, Energy Conversion and Management, 51 (2010) 1989–1997.

[23] N. Miyamoto, H. Ogawa, N.M. Nurun, K. Obata, T. Arima, Smokeless, low NOx high thermal efficiency and low noise diesel combustion with oxygenated agents as main fuel, SAE paper, (1998) Series 980506.

[24] P.J.M. Frijters, R.S.G. Baert, Oxygenated fuels for clean heavy-duty diesel engines, International Journal of Vehicle Design, 41 (2006) 242.

[25] K. Alexandrino, P. Salvo, Á. Millera, R. Bilbao, M.U. Alzueta, Influence of the Temperature and 2 , 5- Dimethylfuran Concentration on Its Sooting Tendency, Combustion Science and Technology, 188 (2016) 651–666.

[26] G. Chen, W. Yu, J. Fu, J. Mo, Z. Huang, J. Yang, Z. Wang, H. Jin, F. Qi, Experimental and modeling study of the effects of adding oxygenated fuels to premixed n-heptane flames, Combustion and Flame, 159 (2012) 2324–2335.

[27] K.H. Song, P. Nag, T.A. Litzinger, D.C. Haworth, Effects of oxygenated additives on aromatic species in fuel-rich , premixed ethane combustion: a modeling study, Combustion and Flame, 135 (2003) 341–349.

[28] C.K. Westbrook, W.J. Pitz, H.J. Curran, Chemical kinetic modeling study of the effects of oxygenated hydrocarbons on soot emissions from diesel engines, Journal of Physical Chemistry A, 110 (2006) 6912–6922.

[29] N. Savage, Fuel options: the ideal biofuel, Nature, 474 (2011) 9–11.

[30] J.T. Moss, A.M. Berkowitz, M. a Oehlschlaeger, J. Biet, V. Warth, P.-A. Glaude, F. Battin-Leclerc, An experimental and kinetic modeling study of the oxidation of the four isomers of butanol., Journal of Physical Chemistry A, 112 (2008) 10843–10855.

[31] S.Y. Lee, J.H. Park, S.H. Jang, L.K. Nielsen, J. Kim, K.S. Jung, Fermentative butanol production by clostridia, Biotechnol and Bioengineering, 101 (2008) 209–228.

[32] S. Atsumi, T. Hanai, J.C. Liao, Non-fermentative pathways for synthesis of branched-chain higher alcohols as biofuels, Nature, 451 (2008) 1–5.

[33] H. Ghiassi, P. Toth, J.S. Lighty, Sooting behaviors of n-butanol and n-dodecane blends, Combustion and Flame, 161 (2014) 671–679.

[34] P. Singh, X. Hui, C.-J. Sung, Soot formation in non-premixed counterflow flames of butane and butanol isomers, Combustion and Flame, 164 (2016) 167–182.

[35] J. Camacho, S. Lieb, H. Wang, Evolution of size distribution of nascent soot in n- and i-butanol flames, Proceedings of the Combustion Institute, 34 (2013) 1853–1860.

[36] P. Dagaut, C. Togbe, Experimental and modeling study of the kinetics of oxidation of butanol-*n*-heptane mixtures in a jet-stirred reactor, Energy and Fuels, 23 (2009) 3527–3535.

[37] S.M. Sarathy, M.J. Thomson, C. Togbé, P. Dagaut, F. Halter, C. Mounaim-Rousselle, An experimental and kinetic modeling study of *n*-butanol combustion, Combustion and Flame, 156 (2009) 852–864.

[38] P. Dagaut, C. Togbé, Oxidation kinetics of butanol–gasoline surrogate mixtures in a jet-stirred reactor: Experimental and modeling study, Fuel. 87 (2008) 3313–3321.

[39] K.A. Heufer, R.X. Fernandes, H. Olivier, J. Beeckmann, O. Ro, N. Peters, Shock tube investigations of ignition delays of *n*-butanol at elevated pressures between 770 and 1250 K, Proceedings of the Combustion Institute, 33 (2011) 359–366.

[40] A.S. AlRamadan, J. Badra, T. Javed, M. Al-Abbad, N. Bokhumseen, P. Gaillard, H. Babiker, A. Farooq, S.M. Sarathy, Mixed butanols addition to gasoline surrogates: Shock tube ignition delay time measurements and chemical kinetic modeling, Combustion and Flame, 162 (2015) 3971–3979.

[41] Z. Yang, Y. Qian, X. Yang, Y. Wang, Y. Wang, Z. Huang, X. Lu, Autoignition of n-

butanol/*n*-heptane blend fuels in a rapid compression machine under low-to-medium temperature ranges, Energy and Fuels, 27 (2013) 7800–7808.

[42] Z. Yang, Y. Wang, X. Yang, Y. Qian, X. Lu, Z. Huang, Autoignition of butanol isomers/*n*-heptane blend fuels on a rapid compression machine in N2/O2/Ar mixtures, Science China Technological Sciences, 57 (2014) 461–470.

[43] D.M.A. Karwat, S.W. Wagnon, P.D. Teini, M.S. Wooldridge, On the chemical kinetics of n-butanol: ignition and speciation studies, The journal of physical chemistry. A, (2011) 4909–4921.

[44] G. Black, H.J. Curran, S. Pichon, J.M. Simmie, V. Zhukov, Bio-butanol: Combustion properties and detailed chemical kinetic model, Combustion and Flame, 157 (2010) 363–373.

[45] P. Saisirirat, F. Foucher, S. Chanchaona, C. Mounaïm-Rousselle, Effects of ethanol, *n*-butanol - *n*-heptane blended on low temperature heat release and HRR phasing in diesel-HCCI, SAE International, (2009).

[46] M.E. Baumgardner, S.M. Sarathy, A.J. Marchese, Autoignition characterization of primary reference fuels and *n*-heptane/n-butanol mixtures in a constant volume combustion device and homogeneous charge compression ignition engine, Energy and Fuels, 27 (2013) 7778–7789.

[47] K. Fushimi, E. Kinoshita, Effect of butanol isomer on diesel combustion characteristics of butanol/gas oil blend, SAE International Journal Engines, 2013-3 (2013).

[48] O. Doğan, The influence of n-butanol/diesel fuel blends utilization on a small diesel engine performance and emissions, Fuel, 90 (2011) 2467–2472.

[49]   Y. Zhang, A.L. Boehman, Oxidation of 1-butanol and a mixture of *n*-heptane/1-butanol in a motored engine, Combustion and Flame, 157 (2010) 1816–1824.

[50]   B.-Q. He, M.-B. Liu, J. Yuan, H. Zhao, Combustion and emission characteristics of a HCCI engine fuelled with n-butanol–gasoline blends, Fuel, 108 (2013) 668–674.

[51]   N. Mittal, P. Patanwal, M. Sithananthan, M. Subramanian, A.K. Sehgal, R. Suresh, B.P. Das, Experimental investigation of n-butanol diesel fuel blends on a passenger car, SAE International Journal Engines, 2015-01-09 (2015).

[52]   M. Reardon, DuPont and BP disclose advanced biofuels partnership targeting multiple butanol molecules, 2008.

URL:https://news.thomasnet.com/companystory/dupont-and-bp-disclose-advanced-biofuels-partnership-targeting-multiple-butanol-molecules-813361.

[53]   X. Feng, Investigation of combustion and emmision characteristics of a diesel engine fueled with butanol-diesel blends, Thesis University Illinois. (2011).

[54]   A. Gomez, G. Sidebotham, I. Glassman, Sooting behavior in temperature-controlled laminar diffusion flames, Combustion and Flame, 58 (1984) 45–57.

[55]   L. Rubino, The effect of oxygenated additives on soot precursor formation, Thesis University of Toronto, 1999.

[56]   H.Bockhorn. (Ed.), Soot Formation in Combustion, in: Springer-Verlag, Berlin., 1994.

[57]   A.C.Y. Yuen, G.H. Yeoh, V. Timchenko, T.B.Y. Chen, Q.N. Chan, C. Wang, D.D. Li, Comparison of detailed soot formation models for sooty and non-sooty flames in an under-ventilated ISO room, International Journal of Heat and Mass Transfer, 115 (2017)

717–729.

[58] M. Frenklach, D.W. Clary, W.C.G. Jr, S.E. Stein, Detailed kinetic modeling of soot formation in shock-tube pyrolysis of acetylene, Symposium (International) on Combustion, 20 (1984) 887–901.

[59] S. Kewley, J.; Jackson, The burning of mineral oil in wick fed lamps, Journal of the Institute of Petroleum, 13 (1927) 364–397.

[60] S.T. Minchin, Luminous stationary flames: the quantitative relationship between flame dimensions at the sooting point and chemical composition, with special reference to petroleum hydrocarbons, Journal of the Institute of Petroleum Technology, 17 (1931) 102–120.

[61] F.H. Clarke, A. E.; Hunter, T. G.; Garner, The tendency to smoke of organic substances on burning. Part I, Journal of the Institute of Petroleum, 32 (1946) 627– 642.

[62] D.B. Olson, J.C. Pickens, The effects of molecular structure on soot formation , I. Soot thresholds in premixed flames, Combustion and Flame, 57 (1984) 199–208.

[63] E.J. Barrientos, Impact of oxygenated fuels on sooting tendency and soot oxidative reactivity with application to biofuels, Thesis University Pennsylvania. (2014).

[64] R.A. Hunt, Relation of smoke point molecular structure, Industrial and Engineering Chemistry, 45 (1953) 602–606.

[65] R.L. Schalla, G.E. Mcdonald, Variation in smoking tendency, Industrial and Engineering Chemistry, 45 (1953) 1497–1500.

[66] H.F. Calcote, D.M. Manos, Effect of molecular structure on incipient soot formation,

Combustion and Flame, 49 (1983) 289–304.

[67]   A. Street, J. C., and Thomas, Carbon formation in premixed flames, Fuel. 34 (1955).

[68]   M.P. Ruiz, A. Callejas, A. Millera, M.U. Alzueta, R. Bilbao, Soot formation from C2H2 and C2H4 pyrolysis at different temperatures, Journal of Analytical and Applied Pyrolysis, 79 (2007) 244–251.

[69]   M. Bolla, D. Farrace, Y.M. Wright, K. Boulouchos, E. Mastorakos, Influence of turbulence-chemistry interaction for *n*-heptane spray combustion under diesel engine conditions with emphasis on soot formation and oxidation, Combustion Theory and Modelling, 18 (2014) 330–360.

[70]   A. Hamins, Soot – Environmental implications of combustion processes, chapter 3, in: CRC Press Boca Rato, 1993: pp. 71–95.

[71]   M.M. Harris, E.T. Al, Influence of temperature and hydroxyl concentration on incipient soot formation in premixed flames, Combustion and Flame, 64 (1986) 99–112.

[72]   A. Ergut, Y.. Levendis, H. Richter, J.B. Howard, J. Carlson, The effect of equivalence ratio on the soot onset chemistry in one-dimensional, atmospheric-pressure, premixed ethylbenzene flames, Combustion and Flame, 151 (2007) 173–195.

[73]   H. Nakamura, R. Tanimoto, T. Tezuka, S. Hasegawa, K. Maruta, Soot formation characteristics and PAH formation process in a micro flow reactor with a controlled temperature profile, Combustion and Flame, 161 (2014) 582–591.

[74]   H. Nakamura, S. Suzuki, T. Tezuka, S. Hasegawa, K. Maruta, Sooting limits and PAH formation of n-hexadecane and 2,2,4,4,6,8,8-heptamethylnonane in a micro flow reactor with a controlled temperature profile, Proceedings of the Combustion Institute, 35 (2014)

3397–3404.

[75] A.K. Dubey, T. Tezuka, S. Hasegawa, H. Nakamura, K. Maruta, Study on sooting behavior of premixed C1–C4 n-alkanes/air flames using a micro flow reactor with a controlled temperature profile, Combustion and Flame, 174 (2016) 100–110.

[76] T. Ingemarsson, R. Pedersen, J.O. Olsson, Oxidation of n-heptane in a premixed laminar flame, The Journal of Physical Chemistry A, 103 (1999) 8222–8230.

[77] D.F. Davidson, Z. Hong, G.L. Pilla, A. Farooq, R.D. Cook, R.K. Hanson, Multi-species time-history measurements during n-heptane oxidation behind reflected shock waves, Combustion and Flame, 157 (2010) 1899–1905.

[78] D.F. Davidson, M.A. Oehlschlaeger, R.K. Hanson, Methyl concentration time-histories during iso-octane and n-heptane oxidation and pyrolysis, Proceedings of the Combustion Institute, 31 (2007) 321–328.

[79] A.J. Smallbone, W. Liu, C.K. Law, X.Q. You, H. Wang, Experimental and modeling study of laminar flame speed and non-premixed counterflow ignition of n-heptane, Proceedings of the Combustion Institute, 32 (2009) 1245–1252.

[80] C. Yao, C. Cheng, S. Liu, Z. Tian, J. Wang, Identification of intermediates in an n-heptane/oxygen/argon low-pressure premixed laminar flame using synchrotron radiation, Fuel, 88 (2009) 1752–1757.

[81] B. Akih-kumgeh and J.M. Bergthorson, Comparative study of methyl butanoate and n-heptane high temperature autoignition, Energy and Fuels, 24 (2010) 2439–2448.

[82] A. Yamamoto, H. Oshibe, H. Nakamura, T. Tezuka, S. Hasegawa, K. Maruta, Stabilized three-stage oxidation of gaseous n-heptane/air mixture in a micro flow reactor with a

controlled temperature profile, Proceedings of the Combustion Institute, 33 (2011) 3259–3266.

[83] O. Herbinet, B. Husson, Z. Serinyel, M. Cord, V. Warth, R. Fournet, P. Glaude, B. Sirjean, F. Battin-leclerc, Experimental and modeling investigation of the low-temperature oxidation of n-heptane, Combustion and Flame, 159 (2012) 3455–3471.

[84] L. Sileghem, V.A. Alekseev, J. Vancoillie, K.M.V. Geem, E.J.K. Nilsson, S. Verhelst, A.A. Konnov, Laminar burning velocity of gasoline and the gasoline surrogate components iso-octane, n-heptane and toluene, Fuel, 112 (2013) 355–365.

[85] H.M. Hakka, R.F. Cracknell, A. Pekalski, P. Glaude, F. Battin-leclerc, Experimental and modeling study of ultra-rich oxidation of n-heptane, Fuel, 144 (2015) 358–368.

[86] L. Seidel, K. Moshammer, X. Wang, T. Zeuch, K. Kohse-höinghaus, F. Mauss, Comprehensive kinetic modeling and experimental study of a fuel-rich, premixed n-heptane flame, Combustion and Flame, 162 (2015) 2045–2058.

[87] A. Tekawade, G. Kosiba, M.A. Oehlschlaeger, Time-resolved carbon monoxide measurements during the low- to intermediate-temperature oxidation of n-heptane, n-decane, and n-dodecane, Combustion and Flame, 173 (2016) 402–410.

[88] Z.E. Loparo, J.G. Lopez, S. Neupane, W.P. Partridge, K. Vodopyanov, S.S. Vasu, Fuel-rich n-heptane oxidation: A shock tube and laser absorption study, Combustion and Flame, 185 (2017) 220–233.

[89] B. Savard, H. Wang, A. Teodorczyk, E.R. Hawkes, Low-temperature chemistry in n-heptane/air premixed turbulent flames, Combustion and Flame, 196 (2018) 71–84.

[90] P. Dagaut, S.M. Sarathy, M.J. Thomson, A chemical kinetic study of n-butanol oxidation

at elevated pressure in a jet stirred reactor, Proceedings of the Combustion Institute, 32 (2009) 229–237.

[91]　C. Togbé, A.M. Ahmed, P. Dagaut, Kinetics of oxidation of 2-butanol and isobutanol in a jet-stirred reactor: Experimental study and modeling investigation, Energy and Fuels, 24 (2010) 5244–5256.

[92]　P. Oßwald, H. Güldenberg, K. Kohse-höinghaus, B. Yang, T. Yuan, F. Qi, Combustion of butanol isomers–A detailed molecular beam mass spectrometry investigation of their flame chemistry, Combustion and Flame, 158 (2011) 2–15.

[93]　J. Cai, L. Zhang, F. Zhang, Z. Wang, Z. Cheng, W. Yuan, F. Qi, Experimental and kinetic modeling study of n-butanol pyrolysis and combustion, Energy and Fuels, 26 (2012) 5550–5568.

[94]　J. Zhang, L. Wei, X. Man, X. Jiang, Y. Zhang, E. Hu, Z. Huang, Experimental and modeling study of n-butanol oxidation at high temperature, Energy and Fuels, 26 (2012) 3368–3380.

[95]　N. Hansen, S.S. Merchant, M.R. Harper, W.H. Green, The predictive capability of an automatically generated combustion chemistry mechanism: Chemical structures of premixed iso-butanol flames, Combustion and Flame, 160 (2013) 2343–2351.

[96]　M. Braun-unkhoff, N. Hansen, T. Methling, K. Moshammer, B. Yang, The influence of i -butanol addition to the chemistry of premixed 1, 3-butadiene flames, Proceedings of the Combustion Institute, 36 (2017) 1311–1319.

[97]　L. Tran, J. Pieper, M. Zeng, Y. Li, X. Zhang, W. Li, I. Graf, F. Qi, K. Kohse-höinghaus, Influence of the biofuel isomers diethyl ether and n-butanol on flame structure and pollutant formation in premixed n-butane flames, Combustion and Flame, 175 (2017)

47–59.

[98]   K. Maruta, T. Kataoka, N. Il Kim, S. Minaev, R. Fursenko, Characteristics of combustion in a narrow channel with a temperature gradient, Proceedings of the Combustion Institute, 30 (2005) 2429–2436.

[99]   A. Fan, S. Minaev, E. Sereshchenko, R. Fursenko, S. Kumar, W. Liu, K. Maruta, Experimental and numerical investigations of flame pattern formations in a radial microchannel, Proceedings of the Combustion Institute, 32 (2009) 3059–3066.

[100]   Y. Tsuboi, T. Yokomori, K. Maruta, Lower limit of weak flame in a heated channel, Proceedings of the Combustion Institute, 32 (2009) 3075–3081.

[101]   Y. Ju, C. Cadou, K. Maruta, Microscale combustion and power generation, Momentum Press LLC New York. (2015).

[102]   Y. Ju, K. Maruta, Microscale combustion: Technology development and fundamental research, Progress in Energy and Combustion Science, 37 (2011) 669–715.

[103]   K. Maruta, Micro and mesoscale combustion, Proceedings of the Combustion Institute, 33 (2011) 125–150.

[104]   A.C Fernandez-Pello, Micropower generation using combustion: issues and approaches, Proceedings of the Combustion Institute, 29 (2002) 883–899.

[105]   P.D. Ronney, Analysis of non-adiabatic heat-recirculating combustors, Combustion and Flame, 135 (2003) 421–439.

[106]   N.I. Kim, T. Kataoka, S. Maruyama, K. Maruta, Flamability limits of stationary flames in tubes at low pressure, Combustion and Flame, 141 (2005) 78–88.

[107] N.I. Kim, S. Aizumi, T. Yokomori, S. Kato, T. Fujimori, K. Maruta, Development and scale effects of small Swiss-roll combustors, Proceedings of the Combustion Institute, 31 (2007) 3243–3250.

[108] H. Oshibe, H. Nakamura, T. Tezuka, S. Hasegawa, K. Maruta, Stabilized three-stage oxidation of DME/air mixture in a micro flow reactor with a controlled temperature profile, Combustion and Flame, 157 (2010) 1572–1580.

[109] M. Hori, A. Yamamoto, H. Nakamura, T. Tezuka, S. Hasegawa, K. Maruta, Study on octane number dependence of PRF/air weak flames at 1-5 atm in a micro flow reactor with a controlled temperature profile, Combustion and Flame, 159 (2012) 959–967.

[110] M. Hori, H. Nakamura, T. Tezuka, S. Hasegawa, K. Maruta, Characteristics of *n*-heptane and toluene weak flames in a micro flow reactor with a controlled temperature profile, Proceedings of the Combustion Institute, 34 (2013) 3419–3426.

[111] S. Suzuki, M. Hori, H. Nakamura, T. Tezuka, S. Hasegawa, K. Maruta, Study on cetane number dependence of diesel surrogates/air weak flames in a micro flow reactor with a controlled temperature profile, Proceedings of the Combustion Institute, 34 (2013) 3411–3417.

[112] T. Kamada, H. Nakamura, T. Tezuka, S. Hasegawa, K. Maruta, Study on combustion and ignition characteristics of natural gas components in a micro flow reactor with a controlled temperature profile, Combustion and Flame, 161 (2014) 37–48.

[113] H. Nakamura, H. Takahashi, T. Tezuka, S. Hasegawa, K. Maruta, K. Abe, Effects of CO-to-H2 ratio and diluents on ignition properties of syngas examined by weak flames in a micro flow reactor with a controlled temperature profile, Combustion and Flame, 172 (2016) 94–104.

[114] Y. Saiki, Y. Suzuki, Effect of wall surface reaction on a methane-air premixed flame in narrow channels with different wall materials, Proceedings of the Combustion Institute, 34 (2013) 3395–3402.

[115] Y. Kizaki, H. Nakamura, T. Tezuka, S. Hasegawa, K. Maruta, Effect of radical quenching on CH4/air flames in a micro flow reactor with a controlled temperature profile, Proceedings of the Combustion Institute, 35 (2015) 3389–3396.

[116] S. Minaev, K. Maruta, R. Fursenko, Nonlinear dynamics of flame in a narrow channel with a temperature gradient, Combustion Theory Model, 11 (2007) 187–203.

[117] M. Hafidzal, H. Nakamura, S. Hasegawa, T. Tezuka, K. Maruta, Effects of n-butanol addition on sooting tendency and formation of C1-C2 primary intermediates of *n*-heptane/air mixture in a micro flow reactor with a controlled temperature profile, Combustion Science and Technology, (2018) 1–16.

[118] H. Wang, R. Deneys Reitz, M. Yao, B. Yang, Q. Jiao, L. Qiu, Development of an *n*-heptane-n-butanol-PAH mechanism and its application for combustion and soot prediction, Combustion and Flame, 160 (2013) 504–519.

[119] L.M. Pickett, D.L. Siebers, Soot formation in diesel fuel jets near the lift-off length, Int International Journal of Engine Research, 7 (2006) 103–130.

[120] S. Kikui, T. Kamada, H. Nakamura, T. Tezuka, S. Hasegawa, K. Maruta, Characteristics of n-butane weak flames at elevated pressures in a micro flow reactor with a controlled temperature profile, Proceedings of the Combustion Institute, 35 (2015) 3405–3412.

[121] Y. Ra, R.D. Reitz, A reduced chemical kinetic model for IC engine combustion simulations with primary reference fuels, Combustion and Flame, 155 (2008) 713–738.

[122] N.A. Slavinskaya, U. Riedel, S.B. Dworkin, M.J. Thomson, Detailed numerical modeling of PAH formation and growth in non-premixed ethylene and ethane flames, Combustion and Flame, 159 (2012) 979–995.

[123] S.M. Sarathy, S. Vranckx, K. Yasunaga, M. Mehl, P. Oßwald, W.K. Metcalfe, C.K. Westbrook, W.J. Pitz, K. Kohse-Höinghaus, R.X. Fernandes, H.J. Curran, A comprehensive chemical kinetic combustion model for the four butanol isomers, Combustion and Flame, 159 (2012) 2028–2055.

[124] A. Frassoldati, A. Cuoci, T. Faravelli, E. Ranzi, Kinetic modeling of the oxidation of ethanol and gasoline surrogate mixtures, Combustion Science and Technology, 182 (2010) 653–667.

[125] A. Frassoldati, A. Cuoci, T. Faravelli, U. Niemann, E. Ranzi, R. Seiser, K. Seshadri, An experimental and kinetic modeling study of n-propanol and iso-propanol combustion, Combustion and Flame, 157 (2010) 2–16.

[126] A. Frassoldati, R. Grana, T. Faravelli, E. Ranzi, P. Oßwald, K. Kohse-Höinghaus, Detailed kinetic modeling of the combustion of the four butanol isomers in premixed low-pressure flames, Combustion and Flame, 159 (2012) 2295–2311.

[127] A. Goldaniga, T. Faravelli, E. Ranzi, P. Dagaut, Oxidation of oxygenated octane improves: MTBE , ETBE , DIPE , and TAME, Symposium (International) on Combustion, 27 (1998) 353–360.

[128] P.S. Veloo, Y.L. Wang, F.N. Egolfopoulos, C.K. Westbrook, A comparative experimental and computational study of methanol, ethanol, and n-butanol flames, Combustion and Flame, 157 (2010) 1989–2004.

[129] M. Frenklach, H. Wang, Detailed modeling of soot particle nucleation and growth,

Symposium (International) on Combustion, 23 (1990) 1559–1566.

[130] T.G. Benish, A.L. Lafeur, K. Taghizadeh, J.B. Howard, C2H2 and PAH as soot growth reactants in premixed C2H4-air flames, Symposium (International) on Combustion, (1996) 2319–2326.

[131] H. Richter, J.B. Howard, Formation of polycyclic aromatic hydrocarbons and their growth to soot—a review of chemical reaction pathways, Progress in Energy and Combustion Science, 26 (2000) 565–608.

[132] W.L. Fitch, A.D. Sauter, Calculation of Relative Electron Impact Total Ionization Cross Sections for Organic Molecules, Analytical Chemistry, 55 (1983) 832–835.

[133] R. Seiser, H. Pitsch, K. Seshadri, W.J. Pitz, H.J. Curran, Extinction and Autoignition of *n*-Heptane in Counterflow Configuration, Proceedings of the Combustion Institute, 28 (2000) 2029–2037.

[134] H.J. Curran, P. Gaffuri, W.J. Pitz, C.K. Westbrook, A comprehensive modeling study of *n*-heptane oxidation, Combustion and Flame, 114 (1998) 147–177.

[135] M. Mehl, W.J. Pitz, C.K. Westbrook, H.J. Curran, Kinetic modeling of gasoline surrogate components and mixtures under engine conditions, Proceedings of the Combustion Institute, 33 (2011) 193–200.

[136] A. Miyoshi, Systematic computational study on the unimolecular reactions of alkylperoxy (RO2), hydroperoxyalkyl (QOOH), and hydroperoxyalkylperoxy (O2 QOOH) radicals, The Journal of Physical Chemistry A, 115 (2011) 3301–3325.

[137] I. Glassman, Soot formation in combustion processes, Symposium (International) on Combustion, 22 (1988) 295–311.

[138] D. Golea, Y. Rezgui, M. Guemini, S. Hamdane, Reduction of PAH and soot precursors in benzene flames by addition of ethanol, The Journal of Physical Chemistry A, 116 (2012) 3625–3642.

[139] A. Violi, G.A. Voth, A.F. Sarofim, The relative roles of acetylene and aromatic precursors during soot particle inception, Proceedings of the Combustion Institute, 30 (2005) 1343–1351.

[140] B. Öktem, M.P. Tolocka, B. Zhao, H. Wang, M. V. Johnston, Chemical species associated with the early stage of soot growth in a laminar premixed ethylene-oxygen-argon flame, Combustion and Flame, 142 (2005) 364–373.

[141] C. Esarte, M. Abián, Á. Millera, R. Bilbao, M.U. Alzueta, Gas and soot products formed in the pyrolysis of acetylene mixed with methanol, ethanol, isopropanol or n-butanol, Energy, 43 (2012) 37–46.

[142] P. Singh, C.-J. Sung, PAH formation in counterflow non-premixed flames of butane and butanol isomers, Combustion and Flame, 170 (2016) 91–110.

Acknowledgments

List of publications

Original papers

(Underline indicates the author of this thesis)

(1) <u>M. Hafidzal</u>, H. Nakamura, T. Tezuka, K. Maruta, Effect of n-butanol addition on soot formation of n-heptane in a micro flow reactor with a controlled temperature profile, ARPN Journal of Engineering and Applied Sciences, 12 (2017) 4813-4817.

(2) <u>M. Hafidzal</u>, H. Nakamura, S. Hasegawa, T. Tezuka, K. Maruta, Effects of n-butanol addition on sooting tendency and formation of C_1-C_2 primary intermediates of n-heptane/air mixture in a micro flow reactor with a controlled temperature profile, Combustion Science and Technology, (2018) 1–16.

(3) <u>M. Hafidzal</u>, H. Nakamura, S. Hasegawa, T. Tezuka, K. Maruta, Effects of n-butanol blends on the formation of hydrocarbons and PAHs from fuel-rich heptane combustion in a micro flow reactor with a controlled temperature profile, Combustion Science and Technology, (Revision with minor correction).

International Conferences

(O indicates the presented person and underline indicates the author of this thesis)

(4) O <u>M. Hafidzal,</u> H. Nakamura, T. Tezuka, K. Maruta, Effect of n-butanol addition on soot formation of n-heptane in a micro flow reactor with a controlled temperature profile, The 4th International Conference on Engineering & ICT 2016 (ICEI 2016), Oral, Apr. 2016.

(5) O <u>M. Hafidzal,</u> H. Nakamura, T. Tezuka, K. Maruta, Study on sooting limits of n-heptane / n-butanol mixtures in a micro flow reactor with a controlled temperature temperature

profile, The Thirty-Sixth International Symposium on Combustion, Poster, Aug. 2016.

(6) O M. Hafidzal, H. Nakamura, T. Tezuka, K. Maruta, Sooting limits of n-heptane / n-butanol mixtures C_2H_2 and C_2H_4 formation in a micro flow reactor with a controlled temperature temperature profile, 13th International Conference on Flow Dynamics 2016 (ICFD), Poster, Oct 2016.

(7) OM. Hafidzal, H. Nakamura, S. Hasegawa, T. Tezuka, K. Maruta, Effect of n-Butanol addition to the sooting limits and PAH formation of n-heptane in a micro flow reactor with a controlled temperature temperature profile, 14th International Conference on Flow Dynamics 2017 (ICFD), Oral, Nov 2017.

National Conferences

(O indicates the presented person and underline indicates the author of this thesis)

(8) OM. Hafidzal, H. Nakamura, T. Tezuka, K. Maruta, Sooting limit of n-heptane/n-butanol mixture in a micro flow reactor with a controlled temperature profile, 53rd National Heat Transfer Symposium of Japan, Oral, May 2016.

(9) OM. Hafidzal, H. Nakamura, T. Tezuka, S. Hasegawa, K. Maruta, Study on impacts of n-butanol addition to sooting limits of n-heptane and PAH formation in a micro flow reactor with a controlled temperature profile with GC measurement, 54th National Heat Transfer Symposium of Japan, Oral, May 2017.